

**Dynamics of Rod-Like Macromolecules
in Heterogeneous Materials**

Dynamics of Rod-Like Macromolecules in Heterogeneous Materials

Felix Höfling



MV WISSENSCHAFT

Felix Höfling, Dynamics of rod-like macromolecules in heterogeneous materials.
Dissertation, Ludwig-Maximilians-Universität München.

© 2006 der vorliegenden Ausgabe:
Verlagshaus Monsenstein und Vannerdat OHG Münster
www.mv-wissenschaft.com

© 2006 Felix Höfling
Alle Rechte vorbehalten

Umschlag & Satz: Felix Höfling
Druck und Bindung: MV-Verlag

ISBN: 978-3-86582-426-4

Erstgutachter: Prof. Dr. Erwin Frey
Zweitgutachter: Prof. Dr. Matthias Fuchs
Tag der mündlichen Prüfung: 26. Oktober 2006

Dissertation

der Fakultät für Physik
der Ludwig-Maximilians-Universität
München

angefertigt am
Hahn-Meitner-Institut Berlin

vorgelegt von
Herrn Felix Höfling
aus Chemnitz

München, den 14. August 2006

Contents

1	Introduction	1
1.1	Biopolymer Networks	1
1.2	Heterogeneous Materials	7
1.3	Percolation Theory	11
1.4	The Lorentz Model	17
1.5	Outline	21
I	Localization in the Lorentz Model	23
2	The Localization Transition and Continuum Percolation	25
3	Diffusion on Percolation Clusters	35
3.1	Self-Similarity and Scaling	36
3.2	Cluster-Resolved Dynamic Scaling Theory	37
3.3	Universal Corrections to the Scaling Behavior	43
4	Dynamics Close to the Transition	47
4.1	Continuum Percolation	47
4.2	The Mean-Square Displacement	52
4.3	Finite-Size Scaling	57
4.4	Space-Resolved Dynamics	59
II	Rod-Like Macromolecules	65
5	Dynamics of a Rod in the Dilute Limit	67
5.1	Introduction	67
5.2	Definition of the Model	69

5.3	Linearized Boltzmann Theory	71
6	Entanglement and Enhanced Diffusion	79
6.1	Molecular Dynamics Simulations	79
6.2	Diffusion Coefficients	83
6.3	A Twofold Persistence	86
7	Synopsis	99
	Appendix	103
A	Matrix Elements of the Collision Operator	105
B	The Interval Newton Method	111
B.1	A Short Introduction to Interval Analysis	111
B.2	The Interval Newton Method	114

List of Figures

1.1	Stereo image of an F-actin layer in a <i>Dictyostelium</i> cell	2
1.2	Examples of heterogeneous materials.	8
1.3	Generation of the Sierpinski gasket	10
1.4	Random fractal derived from a square lattice	11
1.5	Schematic representation of the percolating cluster	12
2.1	Particle trajectories in a Lorentz model	27
2.2	Mean-square displacement $\delta r^2(t)$	29
2.3	Scaling plot of the mean-square displacement	29
2.4	Diffusion coefficient D and localization length ℓ	30
2.5	Mean-quartic displacement and non-Gaussian parameter	33
4.1	Mapping to a random resistor network	49
4.2	Cartoon of the nodes-links-blobs model	49
4.3	Molecular Dynamics algorithm	53
4.4	Power laws of D , ℓ and ξ close to the transition	55
4.5	Comparison of different conjectures for μ	56
4.6	Finite-size scaling for diffusion coefficients	58
4.7	Rectification plots of the diffusion coefficient	58
4.8	Time evolution of the van Hove function $G(r, t)$	60
4.9	Incoherent intermediate scattering function $\Phi_q(t)$	60
4.10	Density-dependence of the non-ergodicity parameter f_q	62
5.1	Geometry of a collision	70
6.1	Geometry for the collision detection	80
6.2	Diffusion coefficients D_{cm} and D_{rot}	85
6.3	The legend of the Ulm sparrow	85
6.4	Mean-square angular displacement $\delta\varphi^2(t)$	87

6.5	Orientation correlation function $\Psi_1(t)$	89
6.6	Initial decay of the orientation correlations	89
6.7	Extended ballistic regime in the mean-square displacement . .	91
6.8	Velocity auto-correlation function $\psi_{cm}(t)$	91
6.9	Snapshots of the needle	92
6.10	Time series of fast and slow degrees of freedom	94
6.11	Correlation functions $\psi_{\perp}(t)$, $\psi_{\parallel}(t)$ and $\Psi_1(t)$	95
6.12	Separation of time scales	95
B.1	Illustrations of the interval Newton method	115

The fear of the LORD is the beginning of wisdom: and the knowledge of the holy is understanding.

(Proverbs 9:10)

1 Introduction

1.1 Biopolymer Networks

Eukaryotic cells exhibit an impressive versatility of biological functioning which is attributed to their amazingly well-balanced design. They actively crawl and squeeze through the membranes of arteria, duplicate themselves following a precise blueprint, and form tissues uniquely combining softness and mechanical strength (*Alberts et al.*, 2002). These processes are intimately connected with a vast number of accessory proteins controlling a set of biological polymers.

DNA, a prominent exponent of a flexible and large polymer, coils up inside the nucleus. Filamentous actin (F-actin), on the other hand, is elongated and forms stiff bundles, viscous gels, or dense networks. Along with other types of fibers, microtubule and intermediate filaments, it develops a sophisticated composite network inside each cell, the cytoskeleton. This network gives mechanical stability to the cell and supplies a scaffold for the cell membrane. Such a biological network in living tissue should not be considered static; rather, it is a highly dynamic structure, being actively driven by chemical reactions with various proteins, e. g., polymerizing enzymes or motor molecules. These active features are indispensable for important cell functions such as cell locomotion and cell division. Further, the cytoskeleton exhibits remarkable viscoelastic properties: it elastically resists instantaneous, mechanical deformation, but lets the cell adapt to permanent changes in its environment.

The overwhelming complexity of a living cell renders a quantitative understanding of cells a mission impossible. To unravel the interwoven physical, chemical and biological processes, research started with the isolation of biological macromolecular assemblies. One of these subunits is the cytoskeleton with its actin networks. F-actin plays a key role as model for stiff polymers: Actin filaments are involved in virtually any mechanical action of cells; they are experimentally comparatively well under control; and they can be tailored

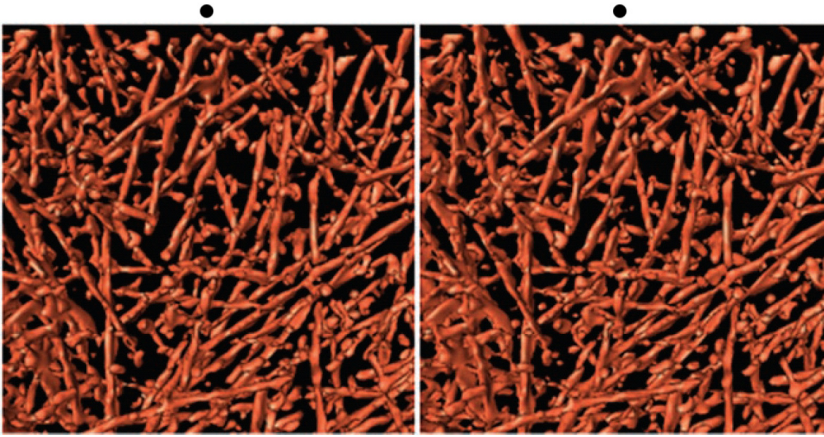


Figure 1.1 Stereo visualization of an F-actin layer in a *Dictyostelium* cell using cryo-electron tomography (Medalia *et al.*, 2002). The width of the figure is about 350 nm, its depth 100 nm. Focus on the black dots at the top, bring them in congruence, and the three-dimensional structure of the network becomes visible.

and manipulated *in vitro* almost at will by means of a large variety of actin binding proteins (Alberts *et al.*, 2002). In particular, actin networks provide a versatile model system to study fundamental properties of polymeric fluids and gels (Bausch and Kroy, 2006; Kroy, 2006).

Theoretical approaches to polymer physics reduce the polymer to its backbone and attribute some diameter a to this line (Doi and Edwards, 1986; de Gennes, 1979). The filaments are characterized by two length scales, the persistence length ℓ_p , being the typical length scale for the decay of tangent-tangent correlations, and the contour length L . A filament is considered flexible when $\ell_p \ll L$, and rigid when the opposite holds. A biologically relevant third category contains semi-flexible or stiff polymers, which have ℓ_p and L comparable in magnitude. These filaments do not form loops and knots (unless certain enzymes are present), yet they are sufficiently flexible to have significant thermal bending fluctuations. *In vitro* polymerized F-actin belongs to this category: it has a persistence length of $17 \mu\text{m}$ (Gittes *et al.*, 1993; Le Goff *et al.*, 2002; Ott *et al.*, 1993), and filaments are between 4 and $70 \mu\text{m}$ long, at average $22 \mu\text{m}$ (Käs *et al.*, 1996). The filaments, however, are quite rigid, e. g., in the cell cortex, where thermal undulations play a subordinate role, see Fig. 1.1.

Tube model for stiff polymers

Highly entangled, semi-dilute solutions of stiff polymers form viscoelastic gels. In contrast to chemically cross-linked networks, the interaction between the polymers is reversible and merely due to steric hindrance. A semi-dilute polymer solution is given when the polymers have substantial overlap, but their volume fraction is still small. Stiff polymers start to “overlap” when their free rotation is hindered, i. e., the polymer concentration n is of the order of L^{-3} due to the rod-like conformations. Excluded volume effects are negligible as long as the backbone diameter a is small against the average mesh size of the network, $\zeta_m = \sqrt{3/nL}$; the latter simply rephrasing the concentration. In this regime ($a \ll \zeta_m$), the static properties should not be effected by the steric interaction between polymers. Experimentally studied F-actin networks have mesh sizes in the sub-micron range, while the filament backbone is about 5 nm thick.

The picture, however, is clouded by thermally induced fluctuations of the contour, blowing up thin polymers to thick tubes of diameter $d \gg a$ (Isambert and Maggs, 1996; Semenov, 1986). A stiff polymer with transverse undulations of wavelength longer than the so-called entanglement length L_e obtains a tube diameter (Hinner *et al.*, 1998; Odijk, 1983)

$$d \approx \left(\frac{L_e^3}{\ell_p} \right)^{1/2}. \quad (1.1)$$

A polymer is effectively confined in its tube, which itself is in a cage formed by the tubes of the surrounding polymers. The mutual steric hindrance of the tubes limits the fluctuations, and the tubes grow until $d \approx \zeta_m^2/L_e$, as can be seen from the following scaling argument (Kroy, 2006):

In a similar spirit as for flexible polymers, the essence of the highly correlated state is expressed in terms of a monomer concentration c_* characteristic to the cross-over between the dilute and the entangled state. Defining the monomer concentration $c = nL/a$, the insertion free energy density can be expressed by a scaling Ansatz,

$$f = n k_B T F(c/c_*). \quad (1.2)$$

The dilute limit is recovered for small arguments requiring $F(x \rightarrow 0) = 1$. At high concentrations, it is expected that collective properties of the strongly entangled solution are independent of the polymer length, and $F(x \rightarrow \infty)$ has to become a power law in order to annihilate the dependence on L and n .

The exponent of the power law follows from the cross-over concentration c_* at which the enveloping tubes, with diameter $d_* = (L^3/\ell_p)^{1/2}$, start to have multiple contacts. (Note that at such a low concentration the entanglement or deflection length, L_e , equals the polymer length.) Since the interaction of two hard, rigid cylinders of diameter d_* and length L results in an excluded volume of about d_*L^2 , the cross-over happens when there is about one polymer per such volume, $nd_*L^2 \approx 1$, yielding

$$c_* \approx \frac{L/a}{d_*L^2} \sim \frac{\ell_p^{1/2}}{L^{5/2}}. \quad (1.3)$$

Consequently, the scaling function behaves as $F(x \rightarrow \infty) \sim x^{2/5}$, and the asymptotic form of the free energy density for tightly entangled polymers follows,

$$f/k_B T \sim c^{7/5} \ell_p^{-1/5} \quad \text{for } c \gg c_*. \quad (1.4)$$

Finally, it is argued that each of the space filling ‘‘blobs’’ or correlation volumes of size $\xi_m^2 L_e/3$ contributes $k_B T$ to the free energy density,

$$f/k_B T \approx 3/\xi_m^2 L_e \sim (nL)^{7/5} \ell_p^{-1/5}, \quad (1.5)$$

yielding the scaling forms of the entanglement length and, via Eq. (1.1), the tube diameter,

$$L_e \sim \xi_m^{4/5} \ell_p^{1/5} \quad \text{and} \quad d \sim \xi_m^{6/5} \ell_p^{-1/5}. \quad (1.6)$$

Using purified F-actin solutions, the confinement of stiff polymers in tubes was observed *in vitro* by video microscopy of fluorescently labelled single filaments (Käs *et al.*, 1994), and the concentration dependence $d \sim c^{-3/5}$ was experimentally confirmed (Käs *et al.*, 1996). This example demonstrates the importance of scaling concepts for the description of highly non-trivial systems. It was sufficient to determine the cross-over point and to assume the cancellation of the length dependence in the free energy of the highly entangled state.

Elasticity and reptation

The mechanical properties of cytoskeletal networks are essential for their physiological function. Due to the heterogeneity of these networks, active microrheological methods were developed which allow local measurements of, e. g., viscoelastic properties (Amblard *et al.*, 1996; Ziemann *et al.*, 1994).

A magnetic bead is placed inside the network and rattled by an external force, the resulting displacement of the particle is tracked by video microscopy and is used to determine the frequency-dependent, complex shear modulus of the network. In an intermediate frequency regime, the real part of this modulus, the storage modulus $G'(\omega)$, exhibits a plateau G_0 , indicating rubber-elasticity in this regime—the highly entangled polymers reacts like a cross-linked network. The plateau modulus depends on the monomer concentration in a subtle way, $G_0 \sim c^{7/5}$ (Hinner *et al.*, 1998; Morse, 2001); although the theoretical prediction, based on the tube model, is supported by experiments with F-actin (Gardel *et al.*, 2003; Hinner *et al.*, 1998; Palmer *et al.*, 1999), the literature knows of different theoretical justifications making different assumptions about the local strain field (Kroy, 2006). Since present experiments cannot distinguish these subtleties and since the interpretation of the microrheological experiments seems to depend on a complete understanding of the network mechanics, extensive computer simulations of simplified models would be of great value.

In the short frequency regime, i. e., on long time scales, the shear modulus falls below its plateau value; the entangled network becomes viscous and starts to flow. Thus, stress due to an imposed strain slowly relaxes—a typical out-of-equilibrium situation, which needs an extension of the above tube model. In a first step, the dynamics of a single polymer is investigated, keeping all other polymers fixed.

For flexible polymers, it was argued by *de Gennes* (1979) that the polymer motion is restricted to the tube which can only be left by sliding back and forth in the tube, a process being termed “reptation” following the Latin *repere*, to creep. Thus, the ends of the tube are continuously released and remodeled, and with each remodeling, they are free to change their orientation since the polymers are flexible. After a characteristic time scale, the disengagement time τ_d , the tube is completely renewed and uncorrelated from the old one. On this time scale, the polymer is free to diffuse, and a translational diffusion coefficient for flexible polymers is inferred, $D_{cm} \sim L^{-2}$.

For stiff polymers, however, the situation is different: the remodeled ends of the tube are correlated and describe some kind of persistent random walk. After the disengagement time, the new tube is not at all uncorrelated with the old one. This requires a different theory for reptation of semiflexible polymers which has still to be formulated. Meanwhile, the stiff polymer might be simplified as a rigid rod, the “reptation” dynamics of which is covered by a theory due to *Doi* and *Edwards* (1978, 1986). The motion of the rod along its tube axis is scarcely hindered by the other polymers, and the trans-

lational diffusion coefficient is approximately the same as in dilute solution: $D_{\text{cm}}^{(0)} \sim L^{-1} \log(L/a)$, due to hydrodynamic interactions. The confinement of F-actin to tubes, the process of reptation as well as the quoted suppression of diffusivity with length was directly observed experimentally (Käs *et al.*, 1994).

A non-trivial prediction is given for the rotational diffusion coefficient of entangled rigid rods; it is strongly suppressed compared to its value in dilute solution, $D_{\text{rot}} \approx D_{\text{rot}}^{(0)} (nL^3)^{-2}$. The time scale at which correlations of the orientation decay is given by the inverse of D_{rot} and really huge: the microscopic time scale of the diffusion process, the disentanglement time grows already with the cube of the rod length, $\tau_{\text{d}} \approx L^2/D_{\text{cm}}$ (Doi and Edwards, 1986). From the data in Ref. (Käs *et al.*, 1994) for F-actin, one estimates $\tau_{\text{rot}} \approx 1-9$ hours for filament lengths between 20 and 50 μm ! Clearly, this regime will be difficult to access experimentally, presently ruling out a verification of the predicted behavior. A way out of this are computer simulations which will nevertheless be very demanding on resources and time. In the present thesis, this issue is targeted using a simplified, two-dimensional model.

Molecular crowding

With microrheological methods, the structure and dynamics of polymer networks can be studied at a specific length scale given by the diameter of the colloidal tracers. Since the relevant scale for the mechanical properties is the mesh size of the network, the motion of appropriately sized colloidal particles was studied in F-actin networks (Wong *et al.*, 2004). It was found that the tracer motion is anomalously slow, i. e., subdiffusive, indicating a heterogeneous structure of the network. The particles are temporarily trapped within “cages” of actin filaments, until they can move on to the next cage. Similar findings were obtained *in vivo* for macromolecules inside the cytoplasm.

The cytoplasm of eukaryotic cells is far from being a homogeneous solution of proteins, sugar and molecules. Rather, it is structured on many length scales: on the μm -scale, there are organelles like the mitochondria, endosomes, and the Golgi apparatus. On smaller scales of about 100 nm, the endoplasmic reticulum imposes together with the cytoskeleton a random reticular network (Alberts *et al.*, 2002). Differently sized proteins, lipids, and sugars constitute more than 40% of the volume of the cytoplasm (Weiss *et al.*, 2004). Consequently, the motion of macromolecules is obstructed; the mobility de-

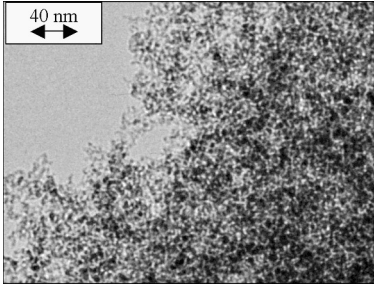
creases as the radius of gyration increases, finally leading to total immobilization of particles with radii larger than 10–30 nm. (Arrio-Dupont *et al.*, 2000; Luby-Phelps *et al.*, 1987, 1986). On short time scales, however, measurements indicate that the mobility is independent of the particle size (Seksek *et al.*, 1997)—supporting the picture of particles being trapped in cages.

The reduction of mobility is related to another effect very well known from disordered and glassy media: critical slowing down. An increase of the radius of the tracer particle effectively increases the volume fraction of the surrounding obstacles. As this effective volume fraction approaches a critical value, the tracer does not diffuse freely, but in a maze leading to a qualitatively different type of motion: anomalous transport or subdiffusion. The mean-square displacement no longer grows linearly, but as a power law, $\delta r^2(t) \sim t^\alpha$, with $\alpha < 1$. Such a behavior was directly measured in the cytoplasm of eukaryotes (Caspi *et al.*, 2002; Tolić-Nørrelykke *et al.*, 2004; Weiss *et al.*, 2004) as well as in bacterial cells (Golding and Cox, 2006). The anomalous, fractal form of the mean-square displacement is attributed to the heterogeneities of the cytoplasm and to the fractal geometry of the cytoskeleton (Aon *et al.*, 2004). The presence of such heterogeneities in the dynamics may directly be observed using the technique of single particle tracking (Saxton and Jacobson, 1997) which currently makes substantial progress (Hellriegel *et al.*, 2005; Levi *et al.*, 2005). Similar phenomena are found not only in molecularly crowded environments, but also in many other materials; they are grouped together in the class of heterogeneous materials to be discussed next.

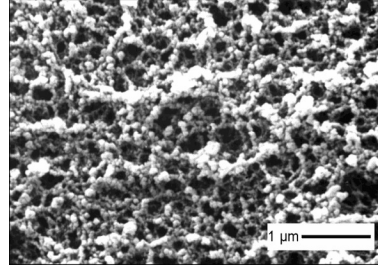
1.2 Heterogeneous Materials

A heterogeneous material is one that is composed of domains of different materials or phases, such as a composite, or the same material in different states, such as a polycrystal. The typical length scale of the material, e. g., the average domain size, shall be much larger than the atomic dimensions, but much smaller than the length of a macroscopic sample. In such circumstances, the heterogeneous material can be subjected to classical analysis, the sample looks homogeneous and macroscopic properties can be ascribed to it (Torquato, 2002).

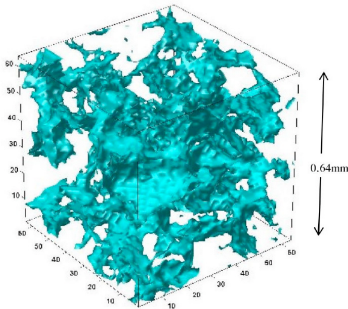
Such heterogeneous media abound in synthetic products and in nature; some examples are gels, foams, and concrete, but also various rocks (sandstone, pumice, or scoria), wood, bone, and biological tissue, a few of them being illustrated in Fig. 1.2. Heterogeneous materials can be investigated by means



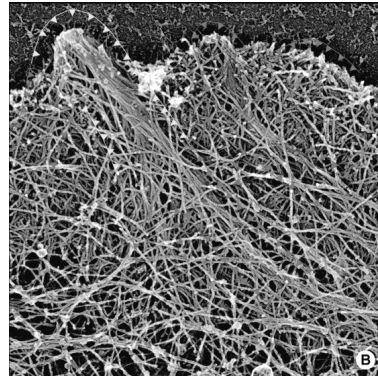
(a) A silica aerogel as seen by transmission electron microscopy (*Knoblich and Gerber, 2001*)



(b) Scanning electron micrograph of the same aerogel as in (a), but at a larger length scale



(c) Pore space of Berea sandstone from micro-computerized tomography, box size: 0.64 mm (*Okabe and Blunt, 2004*)



(d) Electron micrograph of F-actin network (filopodia) in a melanoma cell, image width: 2.2 μm (*Svitkina et al., 2003*)

Figure 1.2 Examples of heterogeneous materials.

of various imaging techniques, e. g., electron microscopy or confocal light microscopy, and, maybe more importantly, scattering techniques such as small-angle neutron or X-ray scattering, nuclear magnetic resonance spectroscopy, and dielectric measurements. A physical understanding of their macroscopic properties, such as mechanical elasticity, electrical conductivity, particle transport or fluid permeability has far reaching consequences for applications in material science, nano-chemistry and oil recovery.

The heterogeneities manifest themselves in the apparent randomness in the morphology of materials, the latter having two major aspects: first, the interconnectedness of its individual elements and, second, the shape and size of these individual elements. However, a heterogeneous morphology is only half of the story; typical examples are diffusion and Brownian motion where apparent random processes are observed over certain length scales. Hence, nature is disordered both in its structure and the dynamic processes that take place therein. Indeed, the two types of disorder are often coupled. An example is fluid flow through a porous rock where the interplay between the disordered morphology of the pore space and the dynamics of fluid motion gives rise to a rich variety of phenomena (Sahimi, 2003).

A physical description of disordered media should provide methods for deriving macroscopic properties of such materials from the laws that govern the microscopic world. Whereas the microscopic details are only relevant for a quantitative description of the physical properties, a general understanding can be gained by focusing on the topology of the medium and the emerging random structures. These structures were successfully modeled in terms of fractals. A more rigorous analysis can be given on the basis of the well established percolation theory.

Fractals

Fractals are geometric objects that look similar when observed at various magnifications; they are *self-similar* (ben Avraham and Havlin, 2000). One type of fractals is generated by a deterministic prescription: in general, one starts from an initial shape, and recursively, adds or removes rescaled copies of this shape to or from the developing structure *ad infinitum*. A two-dimensional example is the Sierpinski gasket, Fig. 1.3. Here, an equilateral triangle of length a is divided into four equal subunits, and the central subunit is discarded. This step is repeated with the remaining three subunits and then iterated further. Proper magnifications of the resulting object are indistinguishable from the original. However, the length a sets an upper cutoff, since a scaled down copy



Figure 1.3 The first steps of the recursive generation of the Sierpinski gasket.

can't be matched with the whole. A lower cutoff were present if the fractal were build up by adding elementary units. Apart from these cutoff lengths, a fractal exhibits no other length scale.

Since the Sierpinski gasket has zero “mass” density, it is sparser than a two-dimensional object, but it is certainly “denser” than a line. Thus, its dimension is expected to be something between 1 and 2; in particular, it is *fractal*. This fractal dimension d_f is defined by the scaling of the mass of the fractal with its linear size, i. e.,

$$M(L) \sim L^{d_f}. \quad (1.7)$$

(The constant of proportionality includes a factor a^{-d_f} in order to get the dimensions right.) In our example, magnifying a sub-triangle by a factor 2 increases its mass by a factor 3, hence $M(2L) = 3M(L)$, and the fractal dimension of the Sierpinski gasket is $d_f = \log(3)/\log(2) \approx 1.585$.

Another kind of fractals is generated by random processes. For example, one could take a huge fishing net and roll a die for each side of every mesh, cutting the thread if the die is odd. The net will fall apart in pieces of all sizes. The largest piece—on average still spanning the original net from edge to edge—is a fractal object termed *incipient infinite cluster* in percolation theory. It will, however, look different if another fishing net is cut. Also, many regions of this cluster won't be similar to some other region. Exact self-similarity is lost, instead we can argue that the fractal is self-similar in a statistical sense: the distribution of holes looks similar at all length scales (Fig. 1.4)—provided the individual meshes are still invisible ($L \gg a$). In particular, no characteristic length scale is present also in a random fractal. The absence of such a length scale forces all physical quantities to obey power laws similar to Eq. (1.7).

The fractal dimension can also be measured for a random fractal if averages over many realizations are considered. In contrast to deterministic fractals, its value is universal for, e. g., different lattices and depends only on the dimension of the embedding space. In two dimensions, it is given by a rational

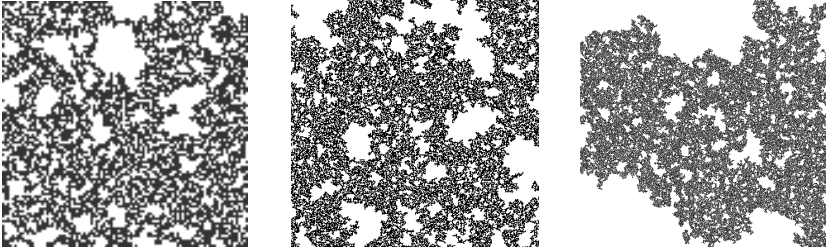


Figure 1.4 A random fractal derived from a square lattice at three different magnifications. The lattice sites were colored with probability $p = 0.5927$; then, only the largest cluster is retained. From left to right, the image widths equal 100, 300 and 1000 lattice spacings. All three images look similar in the sense that they show holes of all sizes.

number, $d_f = 91/48$. In three dimensions, no exact result is available; computer simulations yield $d_f \approx 2.53$ (Stauffer and Aharony, 1994).

1.3 Percolation Theory

Basic concepts

Consider a square lattice on which each bond is present with probability p , or absent with probability $1 - p$. When p is small, there is a dilute population of bonds, and clusters of small numbers of connected bonds predominate. As p increases, the size of the clusters also increases. Eventually, for p large enough there emerges a cluster that spans the lattice from edge to edge. If the lattice is infinite, the inception of the spanning cluster occurs sharply upon crossing a critical threshold of the bond concentration, $p = p_c$.

The probability P_∞ that a given bond belongs to this incipient infinite cluster undergoes a phase transition: it is zero for $p < p_c$, and increases continuously as p is made larger than the critical threshold p_c . Above and close to the transition point, P_∞ follows a power law:

$$P_\infty \sim (p - p_c)^\beta \quad (1.8)$$

This phenomenon is known as percolation transition. The bonds may be interpreted as open channels in a porous medium, and at the transition point, a fluid can percolate through the medium for the first time. The percolation

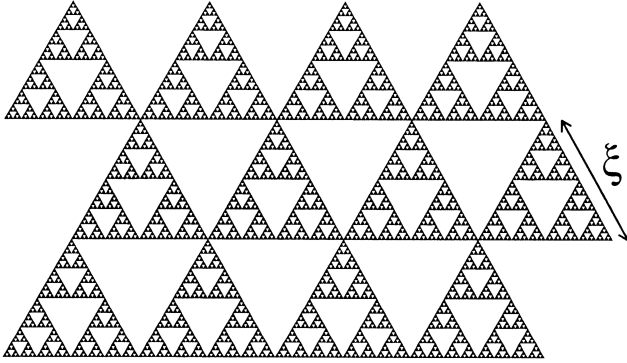


Figure 1.5 Schematic representation of the percolating cluster by repeating the Sierpinski gasket on a triangular lattice: self-similarity is found only on distances shorter than the correlation length ξ , whereas on larger length scales, the cluster is homogeneous. Figure taken from the book by *ben Avraham* and *Havlin* (2000).

transition is analogous to continuous thermodynamic phase transitions with respect to their phenomenology and theoretical concepts; but the mechanisms driving both types of transitions are actually quite different. In the percolation transition, P_∞ plays the role of an order parameter, and β is its critical exponent.

The continuous character of the transition suggests that the percolating cluster grows continuously upon approaching p_c , where it starts to span the whole lattice. In addition to this largest cluster, there is a complete hierarchy of smaller clusters. The typical size of the largest non-percolating or finite cluster defines an important length scale characterizing the medium: the correlation length ξ . It diverges close to the transition as

$$\xi \sim |p - p_c|^{-\nu}, \quad (1.9)$$

constituting another critical exponent ν . Above p_c , the correlation length is also of significance for the structure of the percolating cluster: since the largest holes are typically of size ξ , it can be self-similar only up to length scales smaller than ξ . At length scales large compared to ξ , self-similarity is lost, and the infinite cluster looks homogeneous (Fig. 1.5). Finite clusters are self-similar at small scales where their boundaries are not yet seen. Exactly at the percolation threshold, the limitations by the correlation length are lifted, no characteristic length scale can be found anymore, and the system is scale

invariant. Thus, the concepts of fractals can be successfully applied to the percolation problem; in particular, a fractal dimension, d_f , can be defined.

The peculiar structure of the infinite cluster implies that its mass within a sphere of radius L scales differently for radii shorter and larger than ξ :

$$M(L) \sim \begin{cases} L^{d_f} & \text{if } L \ll \xi, \\ L^d & \text{if } L \gg \xi. \end{cases} \quad (1.10)$$

The probability that an arbitrary bond within a given region of volume L^d belongs to the infinite cluster is given by $M(L)/L^d$. For large distances, $L \gg \xi$, it approaches a constant, namely P_∞ . Matching the behavior for small and large L at the cross-over length ξ , we infer

$$P_\infty \sim \frac{\xi^{d_f}}{\xi^d} \quad (1.11)$$

close to the transition. Comparing the singular behavior of P_∞ and ξ , Eqs. (1.8) and (1.9), an exponent relation follows,

$$d - d_f = \frac{\beta}{\nu}. \quad (1.12)$$

Thus, the fractal dimension is not a new, independent exponent, but depends on the critical exponents β and ν . Other physical quantities introduce more critical exponents, which however, have to fulfill similar scaling relations. In general, an equilibrium phase transition is characterized by only two independent critical exponents, and it is difficult to say which set is the most fundamental one.

Here, an important concept in the context of critical phenomena comes into play: universality. For many thermodynamic phase transitions, the critical exponents, e. g., β and ν , are identical provided that fundamental symmetries are shared. Phase transitions with the same critical exponents are grouped into universality classes. One such class contains many liquid-gas transitions near the critical point and, surprisingly, also the vanishing of ferromagnetism in uniaxial magnets.

Percolation constitutes another universality class. The microscopic details of the system under consideration merely determine the percolation threshold and the prefactors of the divergences, the critical amplitudes. But the qualitative behavior close to the percolation transition, i. e., the divergence of physical quantities, is not influenced by these details. It does not matter whether

the underlying geometry is a square lattice, a honeycomb structure, or even irregular—they all share the same critical exponents. These exponents only depend on the dimensionality of the system. But above the upper critical dimension d_c , even the dimension is irrelevant; the percolation transition has $d_c = 6$.

Random walks and anomalous diffusion

A random walk is a stochastic process defined on the points of a lattice. We will choose its simplest variant, where the time variable is considered discrete as well; but continuous time steps are also chosen frequently, in particular if one likes to describe the real dynamics of the system or use analytical tools (Metzler and Klafter, 2000). At each time step, the “walker” hops to a neighboring site according to a prescribed random rule. This rule is independent of the history of the walk, and so the process is Markovian.

Assume that the walk is performed on a hypercubic lattice in d dimensions and that the rule says that the walker hops to one of its nearest neighbors with equal probability, $1/2d$. Let the lattice spacing be a , and let the time step be τ . Denoting the displacement of the i th step by \mathbf{e}_i and using $|\mathbf{e}_i| = a$, the mean-square displacement of the walker is given by

$$\delta r^2(n\tau) = \left\langle \left(\sum_{i=1}^n \mathbf{e}_i \right)^2 \right\rangle = na^2 + 2 \sum_{i>j}^n \langle \mathbf{e}_i \cdot \mathbf{e}_j \rangle, \quad (1.13)$$

where the average $\langle \dots \rangle$ is over different realizations of the walk. Since the steps are independent, it holds $\langle \mathbf{e}_i \cdot \mathbf{e}_j \rangle = a^2 \delta_{ij}$, and the second term vanishes. Therefore, $\delta r^2(t) \sim t$, and the walker—or more vividly, a set of independent walkers—*diffuses* over the lattice. In particular, a diffusion coefficient, $D = a^2/(2d)\tau$, can be defined such that

$$\delta r^2(t) = (2d)Dt. \quad (1.14)$$

More generally, one can consider the probability distribution $G(\mathbf{r}, t)$ to find the walker at position \mathbf{r} after time t if it started at the origin $\mathbf{r} = 0$ at time $t = 0$. In one dimension, the occupation probability of a site x depends on the occupation of its neighboring sites at the previous time step,

$$G(x, t + \tau) = \frac{1}{2}G(x - a, t) + \frac{1}{2}G(x + a, t), \quad (1.15)$$

the generalization to arbitrary dimensions is straightforward. In the limit of small a and τ , but for fixed a^2/τ , this equation is transformed into a diffusion equation,

$$\partial_t G(\mathbf{r}, t) = D \nabla^2 G(\mathbf{r}, t) \quad (1.16)$$

with the above definition of D , proving that the random walk is indeed a discrete version of the diffusion problem.

What happens if the space available for the walker is not uniform but ramified as in a fractal? Then, the various lattice sites are no longer equal, many of them can't be left in all directions, some can only be left to that site where the walker came from. The Markovian assumption is no longer true, and the hopping process is highly correlated. If the walker enters a large cul-de-sac, it will take some time until it comes back to the exit, and the time inside the cul-de-sac is "lost" for the mean-square displacement. Hence, one expects that the diffusion coefficient is much smaller than in a homogeneous space. Actually, the diffusion coefficient is zero! A new, anomalous transport mechanism arises being *qualitatively* slower than diffusion. It is called anomalous diffusion or subdiffusion; its signature is a mean-square displacement growing slower than linearly with a power law

$$\delta r^2(t) \sim t^{2/d_w}; \quad (1.17)$$

and it is described by the walk dimension d_w . Since $d_w > 2$, the diffusion coefficient, defined as the long-time limit of $\delta r^2(t)/(2dt)$, vanishes.

Such a behavior is observed for a random walk on the percolating cluster exactly at the percolation threshold. The exponent d_w is in general not inferable from the other critical exponents; rather, it is independent and complements the static exponents. Slightly above the threshold, the infinite cluster is fractal only on length scales smaller than the correlation length. Hence, the transport is anomalous only as long as $\delta r^2(t) \ll \xi^2$, defining a cross-over time scale $t_{\text{cross}} \sim \xi^{d_w}$. For much longer times, $t \gg t_{\text{cross}}$, normal diffusion takes place again. Since the cross-over time scale—and thus, the window of anomalous transport—diverges upon approaching the threshold, the diffusion coefficient vanishes. We match the two regimes at the cross-over and estimate,

$$D_\infty \sim \frac{\xi^2}{t_{\text{cross}}} \sim \xi^{-(d_w-2)}. \quad (1.18)$$

The subscript on D_∞ indicates that the walker is restricted to the infinite cluster.

Dynamic scaling

The central idea of critical scaling is that in the vicinity of a continuous phase transition, all static properties are described in terms of a single divergent length scale, the correlation length ξ . The dynamic scaling assumption states further, that this length scale is the same for static and dynamic properties (Ferrell *et al.*, 1967, 1968; Halperin and Hohenberg, 1967; Hohenberg and Halperin, 1977). This implies that close to the transition, all physical properties are independent of the distance to the transition if all lengths are renormalized by ξ , and if time is rescaled by an appropriate power of ξ (and a constant prefactor taking care of the dimensions). In particular, all singular behavior is traced back to the divergence of the correlation length, $\xi \sim |p - p_c|^{-\nu}$. In the previous section, we have expressed the cross-over time, t_{cross} , and the diffusion coefficient, D_∞ , in terms of ξ . But the scaling property also applies to functional contexts, e. g., to the mean-square displacement,

$$\delta r^2(t; p) = \xi^2 \tilde{\delta r}^2 \left(t \xi^{-d_w} \right). \quad (1.19)$$

It is conventional to pull out a factor x^{2/d_w} of $\tilde{\delta r}^2(x)$ and to isolate the anomalous behavior, writing

$$\delta r^2(t; p) = t^{2/d_w} \delta r^2 \left(t \xi^{-d_w} \right). \quad (1.20)$$

Although the mean-square displacement depends on two variables, it can be described by a one-parametric scaling function $\delta r^2(x)$. This function not only combines both the anomalous transport at short time scales and normal diffusion at long times, but also describes the cross-over in detail. It is required to behave asymptotically as

$$\delta r^2(x) \sim \begin{cases} \text{const} & \text{if } x \ll 1, \\ x^{1-2/d_w} & \text{if } x \gg 1. \end{cases} \quad (1.21)$$

A very sensitive test of dynamic scaling is achieved by plotting the rescaled mean-square displacements, $t^{-2/d_w} \delta r^2(t)$, against rescaled time, $t \xi^{-d_w}$, at various bond densities p . Then, the data points will collapse into the scaling function $\delta r^2(x)$. It is an interesting observation that also the scaling functions are often the same within the same universality class (Lübeck, 2005). Thus, data collapse is not only achieved amongst data from different parameters, p , but also amongst data from different systems belonging to the same universality class!

Continuum percolation

One class of percolating systems attracting special interest is that of continuum percolation (Kertész, 1981), which was later also termed “Swiss cheese” model (Halperin *et al.*, 1985). Isolating discs or spheres are distributed at random within a conducting material, they may overlap, and the void space between them forms the percolation clusters. In the simplest variant, the spheres are monodisperse, i. e., have equal radii, but binary distributions were considered as well (van der Marck, 1996; Rintoul, 2000). The percolation threshold was first determined by discretizing the void space and using lattice methods (Kertész, 1981). Much more efficiently, the void space is well represented by a random network constructed from a Voronoi tessellation (Kerstein, 1983); then, the percolation thresholds are calculated for that network. As expected from the universality hypothesis, the critical exponents for static properties, e. g., β and ν , agree with the findings for various lattices of the same dimension (Elam *et al.*, 1984).

The more surprising were theoretical predictions, based on the “nodes-links-blobs” picture, that the exponents of transport properties, e. g., conductivity and elasticity, are considerably larger than their values on lattices; in particular, they are not universal (Halperin *et al.*, 1985; Machta and Moore, 1985) (with exception of the conductivity exponent in $d = 2$). These results were obtained by assigning microscopic properties to the bonds of the network, e. g., in order to investigate the conductivity, the bonds were considered as resistors. Since the macroscopic conductivity only depends on the probability distribution of the bond conductances, the latter are distributed randomly obeying a given distribution. A renormalization group analysis of such random resistor networks (Harris *et al.*, 1984; Lubensky and Tremblay, 1986; Stenull and Janssen, 2001; Straley, 1982) attributes the non-universal character of the critical exponents to a singularity in the distribution of conductances.

Note that the mapping from the geometric Voronoi network to a random resistor network is indeed intuitive, but not at all rigorous. A direct confirmation by measuring transport properties of the Swiss cheese model would be desirable, the present work takes a first step towards this task.

1.4 The Lorentz Model

The Lorentz model has attracted the attention of researchers in statistical physics over more than a century now. Despite its simple formulation, it shares a

wealth of fundamental phenomena having always been a challenge for theory. Originally, *Lorentz* (1905) introduced its model in order to describe the electric resistance in metals: a gas of non-interacting electrons, i. e., point particles, is scattered from the ions which are assumed to be randomly placed in the metal. Due to the vacuum between the ions, the motion is ballistic. Two decades before the invention of quantum mechanics, the model, however, missed the duality of electrons being also waves and hence the consequences of the Bloch theorem—so, it had to fail its purpose.

The revival of the Lorentz model is closely related with the progress of kinetic theory in the 1960s. It started with the discovery that transport coefficients of simple liquids, e. g., the viscosity, cannot be expanded in a power series of the density (*Dorfman and Cohen*, 1965; *Haines et al.*, 1966; *Sengers*, 1965). Similar non-analyticities were found in the Lorentz model (*van Leeuwen and Weijland*, 1967), which can also be considered as a binary fluid mixture of heavy and light particles: the heavy particles are immobile and act merely as scatterers, whereas the light particles move ballistically with constant speed and do not interact with each other; they only change their direction of motion upon collisions with a scatterer. The Lorentz model is more tractable than a fluid, and there, *Weijland* and *van Leeuwen* (1968) obtained the non-analytic expansion of the inverse of a transport coefficient, namely the diffusion coefficient D of a light particle with speed v between heavy particles of radius σ and density n . This asymptotic expansion is valid for dilute systems, $n^* = n\sigma^d \rightarrow 0$; in $d = 2$ dimensions, the first terms are given by

$$\frac{v\sigma}{D} = \frac{16}{3}n^* - \frac{64}{9}(n^*)^2 \log(n^*) + O\left[(n^*)^2\right], \quad (1.22)$$

and in $d = 3$ dimensions,

$$\frac{v\sigma}{D} = 3\pi n^* + b_2(n^*)^2 + b'_3(n^*)^3 \log(n^*) + O\left[(n^*)^3\right]. \quad (1.23)$$

The lowest order represents the result of the linearized Boltzmann equation which treats subsequent collisions as uncorrelated. The calculation of the logarithmic terms involves the resummation of collision sequences of higher order; in three dimensions, only numerical values for the prefactors are known, $b_2 \approx 19.05$ and $b'_3 \approx 0.645$. With the appearance of computers, and therewith, the technique of Molecular Dynamics simulations (*Alder and Wainwright*, 1959), a direct “experimental” verification of this expansion—and of the logarithmic terms—became feasible. (*Bruin*, 1972, 1974)

Long-time tails

One of the most striking early results from the new technique of computer simulations was the discovery of power-law tails for long times in the velocity auto-correlation function, $\psi(t) := v^{-2} \langle \mathbf{v}(t) \cdot \mathbf{v}(0) \rangle$, in simple liquids by *Alder* and *Wainwright* (1967, 1970). They found that a tagged fluid particle remembers its initial velocity unusually long what the slow decay of the correlations reflects, $\psi(t) \sim t^{-d/2}$ for sufficiently long times. These memory effects were explained by the formation of a vortex pattern in the velocity field around the tagged particle: on average, it pushes the particles ahead as it moves, and the particles behind follow in its wake. Theoretical derivations of the phenomenon use hydrodynamic equations (*Ernst et al.*, 1970, 1971; *Kawasaki*, 1971) and kinetic theory techniques (*Dorfman and Cohen*, 1970; *Dorfman and Cohen*, 1972, 1975; *de Schepper and Ernst*, 1977). Since the long-time tail has a positive sign, the tail yields an increase of the diffusion coefficient; the latter being obtained by integrating the velocity auto-correlation function,

$$D = \frac{v^2}{d} \int_0^\infty dt \psi(t). \quad (1.24)$$

A remarkable consequence follows for two-dimensional liquid films: a tagged particle does not show truly diffusive behavior; the diffusion coefficient diverges.

For the Lorentz model, similar tails were predicted from the low-density expansion (*Ernst and Weijland*, 1971; *Weijland and van Leeuwen*, 1968) and measured by means of computer simulations (*Alder and Alley*, 1978; *Bruin*, 1972, 1974). The amplitudes of these tails, however, are negative, and their exponents are different from the liquid,

$$\psi(t) \simeq At^{-d/2-1} \quad \text{for } t \rightarrow \infty. \quad (1.25)$$

The tail in the Lorentz model is of a different nature than the hydrodynamic tails in liquids. It is not due to collective motion; rather, it results from a series of backscattering events preferring the return of the particle to its origin. The regime of higher obstacle densities poses considerable challenges for theory; ring collision sequences play an important role and were accounted for by self-consistent approaches. A mode-coupling approach by *Götze et al.* (1981a,b, 1982) provides a feedback mechanism for the current relaxations down to the particle density. It was found that the exponent of the tail, $d/2+1$, applies at all densities, but with increasing density, a preasymptotic tail, $\psi(t) \sim t^{-\alpha}$, devel-

ops. The time of the cross-over between both tails grows rapidly with increasing density. A self-consistent kinetic theory (Masters and Keyes, 1982) and a completely different approach mapping the Lorentz model to a hopping process on a random network (Machta and Moore, 1985) give similar predictions. Early computer experiments doubt the universality of the tail exponent (Alder and Alley, 1978, 1983); rather, support is claimed for a density-dependent exponent. It was argued (Götze *et al.*, 1981b, 1982) that the simulations cover only a finite and relatively small time window, and that the cross-over pretends effective exponents varying continuously from $d/2 + 1$ to α . More light should be shed on this controversy by simulations of two-dimensional lattice variants of the Lorentz model (Binder and Frenkel, 1990; Frenkel, 1987; Frenkel *et al.*, 1992), clearly observing the t^{-2} decay of the velocity auto-correlation function, independent of density. Further, a direct measurement on the Lorentz model in $d = 2$ corroborates the universality of the exponent (Lowe and Masters, 1993). An unresolved issue is the value of the amplitude, A . Theoretical predictions (Ernst *et al.*, 1984; Götze *et al.*, 1981b) disagree with each other, and greatly underestimate A as simulations in $d = 2$ indicate (Lowe and Masters, 1993).

The localization transition

The emergence of a preasymptotic, negative tail in the velocity auto-correlation function yields an additional suppression of the diffusion coefficient. At a critical obstacle density, n_c^* , the preasymptotic tail persists for all times, yielding zero diffusivity. At higher densities, diffusion is absent as well; moreover, the mean-square displacement saturates—and the moving particle is trapped. This transition from diffusion to localization has the signatures of a continuous phase transition; it exhibits power-law divergences of physical quantities with critical exponents expected to be universal. In particular, the diffusion coefficient vanishes with a power law upon approaching the critical density, $D \sim |n^* - n_c^*|^\mu$.

The transition was predicted by a mode-coupling approach (Götze *et al.*, 1981b) and by a mapping to continuum percolation (Kertész and Metzger, 1983; Machta and Moore, 1985). The mode-coupling approach provides a microscopic picture of the transition and predicts the critical slowing down of the dynamics, i. e., the anomalous transport being a consequence of the preasymptotic tail. But it has severe problems resulting from the divergent length scales at the transition; the mode-coupling functional contains a divergence for small wave numbers which must forcibly be removed. It can provide only poor pre-

dictions of the critical exponents, but nevertheless, it gives a qualitative and detailed description of the Lorentz model. On the other hand, the mapping to continuum percolation and, further, to hopping on random networks, describes the transition phenomenologically and—already anticipating the percolation scenario—accounts for the correct critical exponents. The direct link between the Lorentz model and continuum percolation, however, was not established until the present work.

1.5 Outline

This thesis is laid out in two parts. The first one focuses on the critical dynamics of the Lorentz model close to the localization transition. Chapter 2 gives an overview of the central findings. In particular, the intimate connection between the localization transition and continuum percolation is established, a dynamic scaling Ansatz is introduced which incorporates two divergent length scales, and the importance of corrections to dynamic scaling is demonstrated. Chapter 3 provides the theoretical background for this scaling Ansatz; a relation between the universal dynamic and static correction exponents is derived. Chapter 4 presents a detailed analysis of the data supplemented by a finite-size analysis of the diffusion coefficient and discusses the van Hove function and non-ergodicity parameters.

The second part of the thesis is dedicated to the dynamics of rod-like macromolecules. In Chapter 5, I will introduce a simplified model closely related to the Lorentz model: it describes the dynamics of a needle in a disordered environment of point obstacles. A theoretical description of the dynamics is given, being valid in the dilute regime. It is complemented by Molecular Dynamics simulations in Chapter 6; a novel algorithm allows for the exploration of the full density range and the observation of interesting collective effects. These effects will be discussed phenomenologically considering different non-trivial time scales in the system.

Chapter 7 closes the thesis with a synopsis of the main results.

Part I

**Localization in the
Lorentz Model**

2 The Localization Transition and Continuum Percolation

This chapter has been published as: F. Höfling, T. Franosch, and E. Frey: *Localization transition of the three-dimensional Lorentz model and continuum percolation*, Phys. Rev. Lett. **96**, 165901 (2006). Fig. 2.1 was chosen as cover illustration of this issue.

Abstract

The localization transition and the critical properties of the Lorentz model in three dimensions are investigated by computer simulations. We give a coherent and quantitative explanation of the dynamics in terms of continuum percolation theory and obtain an excellent matching of the critical density and exponents. Within a dynamic scaling Ansatz incorporating two divergent length scales we achieve data collapse for the mean-square displacements and identify the leading corrections to scaling. We provide evidence for a divergent non-Gaussian parameter close to the transition.

Transport in heterogeneous and disordered media has important applications in many fields of science including composite materials, rheology, polymer and colloidal science, and biophysics. Recently, dynamic heterogeneities and growing cooperative length scales in structural glasses have attracted considerable interest (*Berthier et al.*, 2005; *Bertin et al.*, 2005). The physics of gelation, in particular of colloidal particles with short range attraction (*Campbell et al.*, 2005; *Manley et al.*, 2005; *Ruzicka et al.*, 2004; *Zaccarelli et al.*, 2005), is often accompanied by the presence of a fractal cluster generating sub-diffusive dynamics. It is of fundamental interest to demonstrate the relevance of such heterogeneous environments on slow anomalous transport.

The minimal model for transport of particles through a random medium of fixed obstacles, is known as Lorentz model, and already incorporates the generic ingredients for slow anomalous transport. Earlier, the Lorentz model has played a significant role as a testing ground for elaborate kinetic theories,

shortly after the discovery of long-time tails in auto-correlation functions for simple liquids in the late 1960s (*Alder and Wainwright, 1970*), since the non-analytic dependence of transport coefficients on frequency, wavenumber, and density predicted for simple liquids (*Bedaux and Mazur, 1973; Dorfman and Cohen, 1970; Ernst et al., 1971; Kawasaki, 1971; Tokuyama and Oppenheim, 1978*) has a close analog in the Lorentz model (*Ernst and Weijland, 1971; Weijland and van Leeuwen, 1968*).

The simplest variant of the Lorentz model consists of a structureless test particle moving according to Newton's laws in a d -dimensional array of identical obstacles. The latter are distributed randomly and independently in space and interact with the test particle via a hard-sphere repulsion. Consequently, the test particle explores a disordered environment of possibly overlapping regions of excluded volume; see Fig. 2.1. Due to the hard-core repulsion, the magnitude of the particle velocity, $v = |\mathbf{v}|$, is conserved. Then, the only control parameter is the dimensionless obstacle density, $n^* := n\sigma^d$, where σ denotes the radius of the hard-core potential. At high densities, the model exhibits a localization transition, i. e., above a critical density, the particle is always trapped by the obstacles.

Significant insight into the dynamic properties of the Lorentz model has been achieved by a low-density expansion for the diffusion coefficient by *Weijland and van Leeuwen (1968)* rigorously demonstrating the non-analytic dependence on n^* . As expected, for low densities the theoretical results compare well with Molecular Dynamics simulations (*Bruin, 1974*). Elaborate self-consistent kinetic theories (*Götze et al., 1981a,b; Masters and Keyes, 1982*) have allowed going much beyond such perturbative approaches. They give a mathematically consistent description of the localization transition, which allows to calculate the critical density within a 20% accuracy and extend the regime of quantitative agreement to intermediate densities. In addition, they have provided a microscopic approach towards anomalous transport and mean-field-like scaling behavior (*Götze et al., 1981b*).

A different line of approach focusing on the localization transition starts from the fractal nature of the void space between the overlapping spheres in the Lorentz model and considers it as a continuum percolation problem (*Elam et al., 1984; Halperin et al., 1985; Kertész, 1981; Machta and Moore, 1985; Stenull and Janssen, 2001*), which in this context has also been termed “Swiss cheese” model (*Halperin et al., 1985*). These authors conjectured that the transport properties close to the percolation threshold can be obtained by analyzing an equivalent random resistor network. The equivalence, however, has been shown only for geometric properties close to the percolation point (*Ker-*

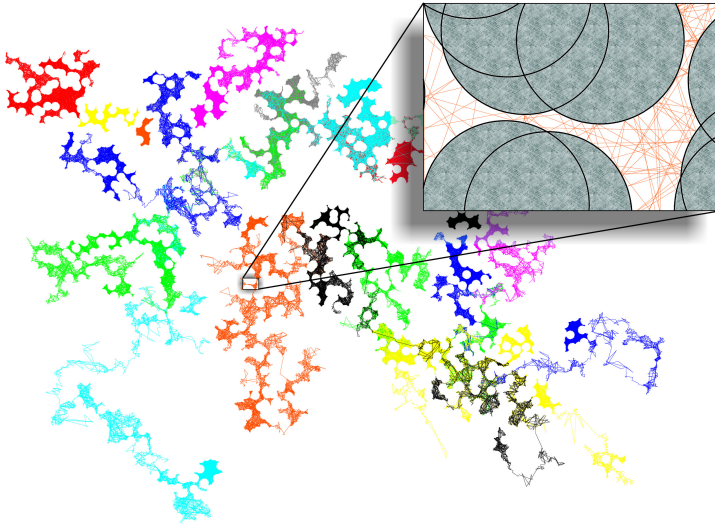


Figure 2.1 Typical particle trajectories in a two-dimensional Lorentz model slightly below n_c^* over a few thousand collisions each. Colors encode different initial conditions; obstacles have been omitted for clarity. Most trajectories being in the percolating void space have some overlap; a few trajectories are confined to finite clusters. Blow-up: a particle squeezes through narrow gaps formed by the obstacles.

stein, 1983). As a peculiarity of continuum percolation, differences to lattice percolation may arise due to power law tails in the probability distribution of the conductances (“narrow gaps”). Such random resistor networks have been investigated extensively by means of Monte-Carlo simulations (*Derrida et al.*, 1984; *Gingold and Lobb*, 1990) and renormalization group techniques (*Harris et al.*, 1984; *Lubensky and Tremblay*, 1986), providing reliable numeric and analytic results for the critical behavior (*Havlin and Ben-Avraham*, 2002).

In this Letter, we present a direct numerical analysis of the dynamic properties of the Lorentz model without resorting to random resistor networks. By means of extensive Molecular Dynamics simulations, we obtain a quantitative description of the dynamic properties over the full density range, in particular, focusing on both sides of the critical region. This allows for a quantitative test of the conjectured mappings to continuum percolation theory. Furthermore, we explore the range of validity of the dynamic scaling hypothesis for the Lorentz model (*Kertész and Metzger*, 1983). The probability distribu-

tion of particle displacements, i. e., the van Hove self-correlation function, $G(\mathbf{r}, t) := \langle \delta(\mathbf{r} - \Delta \mathbf{R}(t)) \rangle$, and its second moment, the mean-square displacement, $\delta r^2(t) := \langle |\Delta \mathbf{R}(t)|^2 \rangle$, are the appropriate quantities for this purpose; $\Delta \mathbf{R}(t) = \mathbf{R}(t) - \mathbf{R}(0)$ denotes the displacement of the test particle at time t .

Over a wide range of obstacle densities, we have simulated several hundred trajectories in three dimensions, employing an event-oriented Molecular Dynamics algorithm. For each of N_r different realizations of the obstacle disorder, a set of N_t trajectories with different initial conditions is simulated. Below the critical density, we have chosen $N_r \geq 25$ and $N_t \geq 4$. At very high densities, where the phase space is highly decomposed, these values have been increased up to $N_r \times N_t = 600$. In order to minimize finite-size effects, the size of the simulation box, L_{box} , has been chosen significantly larger than the correlation length ξ , $L_{\text{box}} = 200\sigma \gg \xi$.¹

The results for the mean-square displacement cover a non-trivial time window of more than seven decades for densities close to the transition, see Fig. 2.2. At low densities, one observes only a trivial cross-over from ballistic motion, $\delta r^2(t) = v^2 t^2$, to diffusion, $\delta r^2(t) \sim t$, near the mean collision time $\tau = 1/\pi n v \sigma^2$ as expected from Boltzmann theory. With increasing density, an intermediate time window opens where motion becomes sub-diffusive, $\delta r^2(t) \sim t^{2/z}$ with $z > 2$. This time window extends to larger and larger times upon approaching a certain critical density n_c^* . For the density $n^* = 0.84$, the sub-diffusive behavior is obeyed over more than five decades and is compatible with a value of $z \approx 6.25$. The power law, $\delta r^2(t) \sim t^{2/z}$, indicated in Fig. 2.2, discriminates nicely trajectories above and below n_c^* . One also observes a density-dependent length scale ℓ characterizing the end of the sub-diffusive regime by $\delta r^2(t) \simeq \ell^2$; upon approaching n_c^* this cross-over length scale ℓ is found to diverge. For long times, the dynamics eventually becomes either diffusive or localized for densities below or above n_c^* , respectively.

The diffusion coefficient D has been extracted from the long-time limit of $\delta r^2(t)/6t$; in Fig. 2.4, D is shown in units of the Boltzmann result, $D_0 = \tau v^2/3$. With increasing density, D is more and more suppressed until it vanishes at n_c^* as a power law, $D \sim |\varepsilon|^\mu$, where $\varepsilon := (n^* - n_c^*)/n_c^*$ defines the separation parameter. Anticipating the exponent μ from percolation theory, a fit to our data yields the critical density,² $n_c^* = 0.839(4)$, and the power law

¹This relation may be violated for $|\varepsilon| < 0.01$. We checked that our findings are not affected by finite-size effects. A detailed analysis is presented in Section 4.3.

²This value for n_c^* corresponds to a critical volume fraction for the obstacles, $\varphi_c = 1 - \exp(-\frac{4\pi}{3} n_c^*) = 0.9702(5)$.

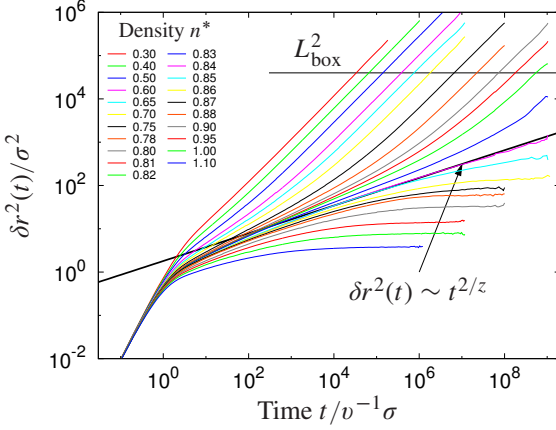


Figure 2.2 Mean-square displacement $\delta r^2(t)$ for various obstacle densities n^* varying from 0.30 (top) to 1.10 (bottom). The thick black line represents a power law, $\delta r^2(t) \sim t^{2/z}$ with $z = 6.25$.

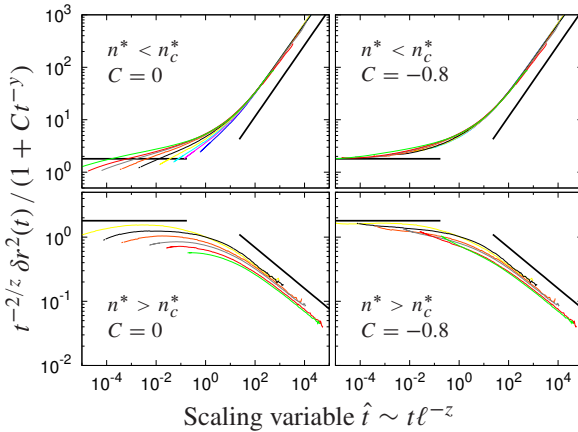


Figure 2.3 Scaling functions $\delta r_{\pm}^2(\hat{t})$ for the mean-square displacement. Right panels include corrections to scaling at leading order. Units are chosen such that $v = \sigma = 1$.

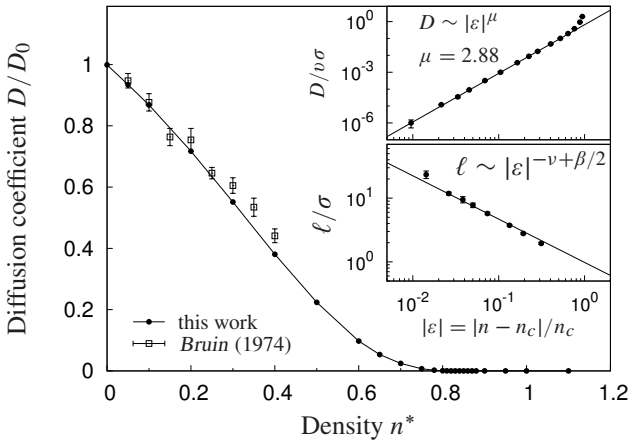


Figure 2.4 Suppression of the diffusion coefficient D/D_0 with increasing density n^* . Top inset: Power-law behavior of D close to n_c^* . Bottom inset: Divergence of the localization length ℓ upon approaching n_c^* with exponent $\nu - \beta/2 = 0.68$.

behavior is confirmed over five decades in D . Above the critical density, the long-time limit of the mean-square displacement is compatible with a power law over more than one decade, $\ell \sim \varepsilon^{-\nu+\beta/2}$, where $\nu - \beta/2 \approx 0.68$ (bottom inset in Fig. 2.4). Our finding of n_c^* coincides with the percolation point of the void space (Elam *et al.*, 1984; Kertész, 1981; Rintoul, 2000). This provides clear evidence for the intimate connection between continuum percolation and the Lorentz model, i. e., diffusion is not blocked as long as there is an infinite path through the medium—a purely geometric reason.

Considering the underlying continuum percolation problem, a geometric transition occurs at n_c^* , above which the void space falls completely apart into finite clusters. Just below this density, the volume fraction P of the percolating void space (infinite cluster) vanishes as a power law, $P \sim |\varepsilon|^\beta$. There are two divergent length scales characterizing the structure of the percolation network: the linear dimension of the largest finite clusters, $\xi \sim |\varepsilon|^{-\nu}$, and the mean cluster radius (radius of gyration), $\ell \sim |\varepsilon|^{-\nu+\beta/2}$ (Stauffer and Aharony, 1994). The geometric exponents β and ν are believed to be the same for lattice and continuum percolation (Elam *et al.*, 1984). Our results in Fig. 2.4 clearly identify the geometric mean cluster radius ℓ with the localization length of the mean-square displacement as anticipated by our choice of notation.

In continuum percolation, transport of a particle is limited by narrow gaps in the void space. It was argued that this feature of the dynamics is captured by an associated random resistor network with a distribution $\rho(W)$ of weak conductances W exhibiting a power-law tail, $\rho(W) \sim W^{-\alpha}$, $\alpha < 1$ for small W (Halperin *et al.*, 1985; Machta and Moore, 1985). Depending on the value of α , the suppression of diffusion, $D \sim |\varepsilon|^\mu$, may be dominated by this tail, and dynamic exponents become different from lattice percolation, $\mu > \mu^{\text{lat}}$. In this case, the hyperscaling relation, $\mu = (d - 2)v + 1/(1 - \alpha)$, holds (Stenull and Janssen, 2001; Straley, 1982). There is a discrepancy in the literature about the value of α in the Lorentz model (Halperin *et al.*, 1985; Havlin and Ben-Avraham, 2002; Machta and Moore, 1985). Only the result of Machta and Moore (1985), $\alpha = (d - 2)/(d - 1)$, is consistent with our data. In $d = 3$, it implies $\mu = v + 2 \approx 2.88$, and therefore, $\mu > \mu^{\text{lat}} \approx 2.0$.³ By means of a scaling relation (Stauffer and Aharony, 1994), $z = (2v - \beta + \mu)/(v - \beta/2)$, one finds the dynamic exponent, $z \approx 6.25$, describing anomalous transport at critical density, $\delta r^2(t) \sim t^{2/z}$. Note that this dynamic exponent is not independent but entirely determined by the geometric properties of the random environment.

In conclusion, the values obtained from the simulated mean-square displacement for the critical density n_c^* , the dynamic exponent z as well as the exponents for the diffusion coefficient μ and the localization length $v - \beta/2$ agree with the predicted values for continuum percolation. Within the statistical accuracy, no deviations can be inferred.

The quality of our data allows to go beyond determining critical exponents and to give a full analysis of the dynamic scaling properties. It has been argued by Kertész and Metzger (1983) that the van Hove correlation function obeys scaling. Rewriting their Ansatz in a more transparent way yields,

$$G(\mathbf{r}, t; \varepsilon) = \zeta^{-\beta/v-d} \mathbf{G}^\pm(\mathbf{r}/\zeta, t\ell^{-z}), \quad (2.1)$$

where \mathbf{G}^\pm are master functions above (+) and below (−) the critical density. This Ansatz clearly reflects the role of the two length scales: the correlation length ζ rescales geometry whereas the cross-over length scale ℓ rescales time. The scaling form of the mean-square displacement is easily inferred from $\delta r^2(t; \varepsilon) = \int d^d \mathbf{r} r^2 G(\mathbf{r}, t; \varepsilon)$ as, $\delta r^2(t; \varepsilon) = t^{2/z} \delta r_\pm^2(\hat{t})$, where $\hat{t} \sim t\ell^{-z}$. Plotting $t^{-2/z} \delta r^2(t; \varepsilon)$ versus \hat{t} for various densities (left panels of Fig. 2.3), the data collapse nicely in the diffusive and localized regimes ($\hat{t} \gg 1$) and

³All exponents are calculated consistently based on the values $\beta = 0.41$, $v = 0.88$, and $\mu^{\text{lat}} = 2.0$ (Stauffer and Aharony, 1994).

converge rapidly to the corresponding large- \hat{t} asymptotes, $\delta r_-^2(\hat{t}) \sim \hat{t}^{1-2/z}$ and $\delta r_+^2(\hat{t}) \sim \hat{t}^{-2/z}$. Convergence to the critical asymptote, $\delta r_{\pm}^2(\hat{t}) \sim \text{const}$, for $\hat{t} \ll 1$ becomes increasingly better as the critical point is approached.

Deviations from scaling can be rationalized by considering the again universal corrections to scaling. Extending the Ansatz, Eq. (2.1), by an irrelevant parameter u leads to $\delta r^2(t; \varepsilon, u) = t^{2/z} \mathcal{R}_{\pm}(t\ell^{-z}, ut^{-y})$, where y is a universal exponent. Since \mathcal{R}_{\pm} is assumed to be analytic for small arguments, one obtains the leading order correction upon expanding \mathcal{R}_{\pm} to first order in u ,

$$\delta r^2(t; \varepsilon) = t^{2/z} \delta r_{\pm}^2(\hat{t}) [1 + t^{-y} \Delta_{\pm}(\hat{t})], \quad (2.2)$$

introducing some analytic functions $\Delta_{\pm}(\hat{t})$. Specializing Eq. (2.2) to the critical density, i. e., $\hat{t} = 0$, yields $\delta r^2(t; \varepsilon = 0) \propto t^{2/z} (1 + Ct^{-y})$, with a single amplitude $C = \Delta_{\pm}(\hat{t} = 0)$; it also identifies y as the leading non-analytic correction exponent at criticality. Our data for $n_c^* = 0.84$ are compatible with values for y between 0.15 and 0.4. For the following, we found the choice $y = 0.34$ and $C = -0.8$ reasonable, the value for y is supported by theoretical arguments presented in Section 3.3.

Inspection of Fig. 2.3 reveals that corrections to scaling are less relevant for long times, $\hat{t} \gg 1$, whereas significant deviations are visible in the critical regime, $\hat{t} \ll 1$. This observation is consistent with the scaling behavior of the diffusion coefficient and the localization length, see Fig. 2.4. These findings also suggest approximating the corrections by its value at $\hat{t} = 0$, i. e., substituting $\Delta_{\pm}(\hat{t}) = C$ in Eq. (2.2) for all times, $\delta r^2(t; \varepsilon) = t^{2/z} \delta r_{\pm}^2(\hat{t}) (1 + Ct^{-y})$. With y and C already inferred from the data close to criticality, the correction terms should apply for all densities. Indeed, including this leading-order correction improves the data collapse substantially (Fig. 2.3, right panels).

The presence of two different length scales, ℓ and ζ , in the scaling hypothesis, Eq. (2.1), is not manifested in the mean-square displacement; it will, however, affect the higher moments of the probability distribution, e. g., the mean-quartic displacement, $\delta r^4(t; \varepsilon) = \int d^d \mathbf{r} r^4 \mathbf{G}(\mathbf{r}, t; \varepsilon)$. Above n_c^* , it is easily inferred that the long-time limit of the mean-quartic displacement scales as, $\delta r^4(t \rightarrow \infty) \sim \zeta^2 \ell^2$. At the critical density, we obtain the long-time asymptote, $\delta r^4(t) \sim t^{4/\tilde{z}}$, with the exponent $\tilde{z} := (2\nu - \beta + \mu)/(\nu - \beta/4) \approx 5.45$ different from z . We have evaluated the mean-quartic displacement by our simulation and find agreement with the prediction of continuum percolation at a similar level of significance as for the mean-square displacement, see Fig. 2.5. In particular, for the density $n^* = 0.84$ the mean-quartic displacement follows a power-law with the predicted exponent \tilde{z} for a time window of more than four decades.

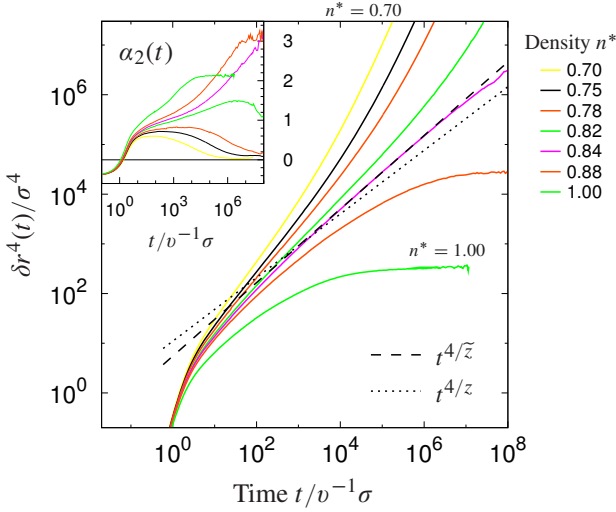


Figure 2.5 Mean-quartic displacement $\delta r^4(t)$ for densities above and below n_c^* . The dashed and dotted lines compare the two exponents \tilde{z} and z . Inset: non-Gaussian parameter $\alpha_2(t)$ for the same densities, its long-time limit increases as n_c^* is approached.

A more sensitive quantity is the (first) non-Gaussian parameter, $\alpha_2(t) := \frac{3}{5}\delta r^4(t)[\delta r^2(t)]^{-2} - 1$, quantifying deviations from a Gaussian distribution (Boon and Yip, 1991). At criticality, it diverges as $\alpha_2(t) \sim t^{4/\tilde{z}-4/z} \approx t^{0.097}$; direct observation of this very small exponent is expected to be a considerably difficult task. The long-time limits of $\alpha_2(t)$ diverge upon approaching n_c^* from either above or below as $\alpha_2(t \rightarrow \infty) \sim |\varepsilon|^{-\beta}$. In particular, the non-Gaussian parameter does not vanish in the diffusive regime close to the transition due to the presence of localized particles even below n_c^* . Although there are significant statistical errors in the data for the non-Gaussian parameter, Fig. 2.5 (inset) provides evidence for a significant increase of $\alpha_2(t)$ as density approaches n_c^* from either side. The properties of the non-Gaussian parameter demonstrate that the presence of two divergent length scales is crucial for the understanding of the dynamics close to the localization transition.

3 Diffusion on Percolation Clusters

Abstract

Based on scaling concepts and the fundamental assumption for percolation theory that a porous medium is self-similar up to length scales shorter than the correlation length, we formulate a cluster-resolved theory for diffusion on percolation clusters. It gives scaling predictions for the medium before cluster averages are performed and illuminates the emergence of two different length scales in the dynamic properties—the latter was demonstrated for the van Hove probability distribution in Chapter 2. Further, the van Hove function, which contains the statistical information about the dynamics, is generalized by including also the static structure, i. e., the cluster numbers. Therewith, a relation between the static correction exponent for the cluster numbers and the dynamic correction exponent for the anomalous diffusion can be established.

Transport in porous media has been modeled by diffusion on percolation clusters. Many experimental techniques, e. g., nuclear magnetic resonance, dielectric measurements and inelastic neutron scattering, probe the percolating cluster and finite clusters at the same time. Most theoretical work on percolation clusters focuses on the infinite cluster where the physics can be described using a single length scale, the correlation length ζ . As soon as cluster averages come into play, the picture becomes a little bit more involved, since two divergent length scales enter the description, see Chapter 2. Real experiments will hardly test the critical point exactly, and deviations from the universal scaling behavior should be considered. These dynamic corrections are again of universal character and can even be related to static corrections as will be demonstrated in this article. Although the presentation will be given along the example of the Lorentz model, it is valid for percolation clusters in general.

3.1 Self-Similarity and Scaling

Scale invariance is a property that gives rise to a series of predictions for many areas of physics and related natural sciences. You can find fractals ubiquitous in nature and many nice illustrations are available. Let us condense this observation in the principle of self-similarity and scale invariance. Scale invariance at criticality dictates that the system looks identical upon zooming in and out. The counting statistics under scale transformation, $L \mapsto \lambda L$, in such a scale invariant system remains identical, except that cluster “masses” rescale by a factor of $M \mapsto \lambda^{d_f} M$ —which defines the crucial quantity of the system: the fractal dimension d_f (*ben Avraham and Havlin, 2000; Stauffer and Aharony, 1994*).

In particular, the mass of the incipient infinite cluster is scale-dependent, i. e., the total mass of the cluster in a large sphere of radius L scales at criticality as $M_c(L) \sim L^{d_f}$. Obviously, the density $M_c L^{-d}$ becomes smaller and smaller as the scale factor L is increased: the volume fraction of this cluster on large scales is zero.

Assume that, at criticality, a specified site belongs to the infinite cluster; then, the conditional probability that another site separated at a distance \mathbf{r} also belongs to this cluster is denoted by $g_\infty^c(\mathbf{r})$. It follows that $M_c(L)$ is determined by

$$M_c(L) = \int_{r < L} d^d r g_\infty^c(\mathbf{r}) \sim L^{d_f}. \quad (3.1)$$

One expects $g_\infty^c(\mathbf{r})$ to be self-similar, i. e., to follow a power law, and it is required that

$$g_\infty^c(\mathbf{r}) \sim r^{-(d-d_f)} \quad \text{for } r \rightarrow \infty. \quad (3.2)$$

In addition to the incipient infinite cluster, a continuous hierarchy of finite clusters is present. Scale invariance at criticality requires that the probability n_s for a specified site to belong to an s -cluster does not exhibit a preferred size, i. e., is a power law in the cluster size again, $n_s \sim s^{-\tau}$ for $s \rightarrow \infty$. Equivalently, we consider the cumulative probability, i. e., the probability for a cluster to contain at least s sites, $N(s) \sim s^{1-\tau}$.

The number of clusters having at least s sites in a volume of L^d is given by $N(s)L^d$. Rescaling the unit of length by a factor of λ , i. e., $L \mapsto \lambda L$, we require

$$N(s)L^d = N(\lambda^{d_f} s)(\lambda L)^d, \quad (3.3)$$

i. e.,

$$s^{1-\tau} L^d = (\lambda^{d_f} s)^{1-\tau} (\lambda L)^d. \quad (3.4)$$

This yields the first relation between exponents, here the Fisher exponent τ and the fractal dimension,

$$\tau = 1 + \frac{d}{d_f}. \quad (3.5)$$

3.2 Cluster-Resolved Dynamic Scaling Theory

The conditional probability that, provided a specified site belongs to an s -cluster, a site separated at a distance \mathbf{r} also belongs to the same cluster is denoted by $g_s(\mathbf{r})$. At criticality, one expects that large finite clusters all look alike up to rescaling. The typical linear dimension of an s -cluster¹ is denoted by $R_s \sim s^{1/d_f}$, and we assume the following scaling form,

$$g_s^c(\mathbf{r}) = R_s^{-(d-d_f)} g_F^c(r/R_s), \quad s \rightarrow \infty. \quad (3.6)$$

It should be noted that no new exponent enters the expression. The relation merely manifests scale invariance at criticality. Indeed, rescaling lengths scales, $r \mapsto \lambda r$, $R_s \mapsto \lambda R_s$, $s \mapsto s \lambda^{d_f}$, reflects the invariance property,

$$\int d^d r g_s^c(\mathbf{r}) = R_s^{d_f} \int d^d \hat{r} g_F^c(\hat{r}) = \lambda^{d_f} \int d^d (\lambda r) g_{s \lambda^{d_f}}^c(\lambda \mathbf{r}). \quad (3.7)$$

Close to the percolation threshold

Away from criticality, the infinite cluster exists only on one side of the threshold, and it looks homogeneous on scales larger than the correlation length ζ . Denoting the distance to the threshold by $\varepsilon = (n - n_c)/n_c$, the correlation length diverges upon approaching the threshold as $\zeta \sim |\varepsilon|^{-\nu}$ introducing a new exponent ν . For distances much shorter than the correlation length, the infinite cluster still looks like at criticality; the correlation length is irrelevant at these scales. At scales much larger than the correlation length, the infinite cluster becomes homogeneous, and we extend the scaling for the two-point correlation function by

$$g_\infty(\mathbf{r}; \varepsilon) = \zeta^{-(d-d_f)} g_\infty(r/\zeta). \quad (3.8)$$

¹Away from the threshold, this interpretation holds only for not too large s -clusters, $s \ll \zeta^{d_f}$.

The scaling function $g_\infty(\hat{r})$ behaves as power law for short rescaled distances, $g_\infty(\hat{r}) \sim \hat{r}^{-(d-d_f)}$. For scales large compared to the correlation length, the conditional probability becomes independent of the distance, i. e., the joint probability factorizes,

$$g_\infty(r \gg \xi; \varepsilon) = \frac{\text{Prob}(\mathbf{r} \in \mathcal{C}_\infty \text{ and } \mathbf{0} \in \mathcal{C}_\infty)}{\text{Prob}(\mathbf{0} \in \mathcal{C}_\infty)} = P_\infty(\varepsilon) \quad (3.9)$$

where $P_\infty(\varepsilon) = \text{Prob}(\mathbf{r} \in \mathcal{C}_\infty)$ is the probability for a site \mathbf{r} to belong to the infinite cluster. A prediction resulting from the self-similarity hypothesis is

$$P_\infty(\varepsilon) \sim \xi^{-(d-d_f)} \sim |\varepsilon|^{\nu(d-d_f)}. \quad (3.10)$$

Defining another exponent β such that $P_\infty(\varepsilon) \sim |\varepsilon|^\beta$, we obtain the hyper-scaling relation,

$$d_f = d - \frac{\beta}{\nu}. \quad (3.11)$$

The mass of the infinite cluster within a sphere of radius L reflects that self-similarity is limited to scales of the order of the correlation length,

$$M(L; \varepsilon) = \int_{r < L} d^d r g_\infty(\mathbf{r}; \varepsilon) = \xi^{d_f} M(L/\xi). \quad (3.12)$$

For small arguments L/ξ , we require $M(\hat{L}) \sim \hat{L}^{d_f}$ in order to recover the result at criticality, $M(L; \varepsilon = 0) \equiv M_c(L) \sim L^{d_f}$.

If the system is only close to criticality, scaling suggests that some aspects of self-similarity are retained at least for length scales not too large. We have seen that scale invariance implies that the cluster distribution follows a power law, $n_s \sim s^{-\tau} \sim R_s^{-d-d_f}$. Close to the transition but away from it, we need an additional scaling law²

$$n_s(\varepsilon) = \xi^{-d-d_f} n^\pm(s \xi^{-d_f}) \quad \text{for } s \rightarrow \infty, \varepsilon \rightarrow 0, \quad (3.13)$$

where we have allowed for different master functions n^\pm above and below the transition. Again for clusters smaller than one with a linear extension of the correlation length, $s \ll \xi^{d_f}$, the distribution looks as if at criticality. For the scaling function this observation implies

$$n^\pm(\hat{s}) \sim \hat{s}^{-1-d/d_f} = \hat{s}^{-\tau}, \quad \text{for } \hat{s} \ll 1. \quad (3.14)$$

²Stauffer and Aharony (1994) introduce another exponent σ with no obvious physical content by writing the cluster distribution as $n_s(\varepsilon) = s^{-\tau} h(cs)$, where $c \sim |\varepsilon|^{1/\sigma} \sim \xi^{-d_f}$, i. e., $d_f = 1/\nu\sigma$.

Clusters with linear dimension significantly larger than ζ are known to be exponentially rare, thus, we require a rapid decay of $n^\pm(\hat{s})$ for $\hat{s} \gg 1$.

The proper extension for the two-site conditional probability reads

$$g_s(\mathbf{r}; \varepsilon) = R_s^{-(d-d_f)} g_F^\pm(r/R_s, \zeta/R_s), \quad (3.15)$$

with again two different master functions g_F^\pm for either side of the transition. In particular, scaling states that there are essentially two types of clusters:

- (i) clusters of linear dimensions $R_s \ll \zeta$ look like if generated at the critical point, $g_F^\pm(\hat{r}, \hat{\zeta} \rightarrow \infty) \equiv g_F^c(\hat{r})$. The correlation length ζ becomes irrelevant.
- (ii) very large clusters ($R_s \gg \zeta$) apart from being rare have a completely different structure: they are fractal on small scales, $r \ll \zeta$, and homogeneous on large scales, $r \gg \zeta$.

Hence, we require for the master functions g_F^\pm to behave asymptotically as

$$g_F^\pm(\hat{r}, \hat{\zeta}) \sim \begin{cases} \hat{r}^{-(d-d_f)} & \text{if } \hat{r} \ll \hat{\zeta} \text{ and } \hat{r} \ll 1, \\ \text{const} & \text{if } \hat{\zeta} \ll \hat{r} \ll 1, \\ O(e^{-\hat{r}}) & \text{if } \hat{r} \gg 1. \end{cases} \quad (3.16)$$

Cluster averages

In practice, measurements are often performed on clusters of all sizes at the same time. This introduces an average over all finite and the infinite cluster, the latter contributes only in the percolating regime. The probability $g(\mathbf{r}; \varepsilon)$ for a site separated a distance \mathbf{r} to belong to the same cluster can be inferred as

$$g(\mathbf{r}; \varepsilon) = \sum_s s n_s(\varepsilon) g_s(\mathbf{r}; \varepsilon) + P_\infty(\varepsilon) g_\infty(\mathbf{r}; \varepsilon) \quad (3.17)$$

$$= r^{-2(d-d_f)} g^\pm(r/\zeta) \quad (3.18)$$

and is known under the name pair-correlation function. For distances much larger than the correlation length, the pair correlation is exponentially small if no infinite cluster is present. If it is present, the pair correlation attains a constant value, given by the probability that *both* sites belong to the infinite

cluster, $P_\infty(\varepsilon)^2 \sim \xi^{-2(d-d_f)}$. For length scales small compared to the correlation length the pair correlation falls off according to a power law; it should be noted that the corresponding exponent is twice the one of the infinite cluster.

Moments of the pair-correlation function are calculated from the cluster-resolved moments. Since $g_s(\mathbf{r}; \varepsilon)$ is an absolute probability rather than a probability density, the averages need to be normalized,

$$\langle r^m \rangle_s = \frac{\int d^d r r^m g_s(\mathbf{r}; \varepsilon)}{\int d^d r g_s(\mathbf{r}; \varepsilon)} = R_s^m r^m(R_s/\xi), \quad (3.19)$$

$$\begin{aligned} \langle r^m \rangle_\infty &= \lim_{L \rightarrow \infty} \frac{\int_{r < L} d^d r r^m g_\infty(\mathbf{r}; \varepsilon)}{\int_{r < L} d^d r g_\infty(\mathbf{r}; \varepsilon)} \\ &\sim \lim_{L \rightarrow \infty} \frac{\xi^{m+d_f}(L/\xi)^d}{\xi^{d_f}(L/\xi)^d} \sim \xi^m. \end{aligned} \quad (3.20)$$

On the infinite cluster, the result $\langle r^m \rangle_\infty \sim \xi^m$ is readily interpreted by the observation that the correlation length ξ is the only present length scale in this case. On small clusters, $R_s \ll \xi$, the moments become independent of ξ requiring r^m to be constant for small arguments. Conversely, on very large finite clusters, R_s cancels due to the normalization, and the moments are determined by the correlation length approaching the result on the infinite cluster, hence, $r^m(x) \sim 1/x$ for $x \gg 1$. Averaging over all finite and the infinite cluster yields,

$$\langle r^m \rangle = \sum_s s n_s(\varepsilon) \langle r^m \rangle_s + P_\infty(\varepsilon) \langle r^m \rangle_\infty \sim \xi^{m-(d-d_f)}, \quad (3.21)$$

where both terms contribute equally.

In addition to the correlation length, another important length scale emerges when characterizing the properties of the medium: the root mean-square cluster size or radius of gyration ℓ . It diverges at the threshold as

$$\ell := \sqrt{\langle r^2 \rangle} \sim \xi^{1-(d-d_f)/2} \sim |\varepsilon|^{-\nu+\beta/2}. \quad (3.22)$$

It may be noted that the second moment of the *averaged* correlation function, $g(\mathbf{r}; \varepsilon)$, yields the squared correlation length,

$$\lim_{L \rightarrow \infty} \frac{\int_{r < L} d^d r r^2 g(\mathbf{r}; \varepsilon)}{\int_{r < L} d^d r g(\mathbf{r}; \varepsilon)} \sim \xi^2. \quad (3.23)$$

Dynamic correlation functions

In the Lorentz model, a test particle is placed on an arbitrary cluster which then is explored by the particle dynamics. The complete statistical information of this process is encoded in the cluster-resolved van-Hove self-correlation function,

$$G_s(\mathbf{r}, t) := \langle \delta(\mathbf{R}(t) - \mathbf{R}(0) - \mathbf{r}) | \mathbf{R}(0) \in \mathcal{C}_s \rangle, \quad (3.24)$$

where $\mathbf{R}(t)$ denotes the trajectory of the particle. The average is performed over a restricted phase space in order to fulfill the condition that the initial point is on an s -cluster, and over the realizations of the random medium. For long times, the static pair-correlation functions are recovered,

$$G_s(\mathbf{r}, t \rightarrow \infty) \sim R_s^{-d_f} g_s(\mathbf{r}). \quad (3.25)$$

On the infinite cluster, the same equations with $s = \infty$ hold.

Since the incipient infinite cluster is completely fractal, the dynamics of the particle is fractal again. A new independent exponent arises, the walk dimension d_w . For long times, the particle has explored a mean-square displacement, $\delta r_\infty^2(t) := \langle [\mathbf{R}(t) - \mathbf{R}(0)]^2 | \mathbf{R}(0) \in \mathcal{C}_\infty \rangle \sim t^{2/d_w}$. Away from the threshold, we expect fractal dynamics as long as the particle motion is restricted to distances much smaller than the correlation length, $\delta r_\infty^2(t) \ll \xi^2$. Beyond, the medium looks homogeneous and usual diffusion is recovered. The dynamic scaling Ansatz for the infinite cluster reads,

$$G_\infty(\mathbf{r}, t; \varepsilon) = \xi^{-d} \mathbf{G}_\infty(r/\xi, t\xi^{-d_w}) \quad \text{for } r, t \rightarrow \infty. \quad (3.26)$$

For large finite clusters, a single length scale R_s determines the dynamics at long length and time scales. We extend Eq. (3.15) to

$$G_s(\mathbf{r}, t; \varepsilon) = R_s^{-d} \mathbf{G}_F^\pm(r/R_s, tR_s^{-d_w}, \xi/R_s) \quad (3.27)$$

Essentially this states that clusters much smaller than the correlation length, $R_s \ll \xi$, all have identical dynamics up to rescaling length and time scales by intrinsic cluster properties. Furthermore, for lengths $r \ll R_s \ll \xi$ and times $t \ll R_s^{d_w}$ the clusters look like the incipient infinite cluster.

The size of the cluster where the particle is placed is not known *a priori* in a computer simulation without an additional analysis of the geometry. Therefore, one would like to have predictions for the unconditional correlation function, i. e., averaged over all clusters. In experiments, this average is inevitable,

and the averaged van Hove correlation function is the quantity containing all accessible statistical information. It is given by

$$G(\mathbf{r}, t; \varepsilon) := \sum_s s n_s(\varepsilon) G_s(\mathbf{r}, t; \varepsilon) + P_\infty(\varepsilon) G_\infty(\mathbf{r}, t; \varepsilon). \quad (3.28)$$

Exploiting the above scaling Ansatz, one easily derives

$$G(\mathbf{r}, t; \varepsilon) = \xi^{-2d+d_f} \tilde{G}^\pm(r/\xi, t\xi^{-d_w}). \quad (3.29)$$

It is favorable to rewrite this expression in order to introduce the dynamic exponent,

$$z := \frac{d_w}{1 - (d - d_f)/2} \quad \text{such that} \quad \ell^z \sim \xi^{d_w}, \quad (3.30)$$

Applying Eq. (3.11), the scaling Ansatz for the cluster-averaged van Hove correlation function is obtained, see Chapter 2 and (Kertész and Metzger, 1983),

$$G(\mathbf{r}, t; \varepsilon) = \xi^{-d-\beta/\nu} \mathbf{G}^\pm(r/\xi, t\ell^{-z}). \quad (2.1)$$

The roles of the exponent z and the length ℓ become apparent in the scaling form of the cluster-averaged mean-square displacement, which can be inferred from

$$\delta r^2(t; \varepsilon) = \int d^d \mathbf{r} r^2 G(\mathbf{r}, t; \varepsilon) = t^{2/z} \delta r_\pm^2(t\ell^{-z}). \quad (3.31)$$

In absence of an infinite cluster, the mean-square displacement saturates for long times, $\delta r_\pm^2(\hat{t} \gg 1) \sim \hat{t}^{-2/z}$, and the long-time limit of the mean-square displacement is given by the mean-square cluster size,

$$\delta r^2(t \rightarrow \infty) \sim \ell^2. \quad (3.32)$$

For not too large times, when the particle has only explored a region with linear dimension smaller than the cross-over length, $t \ll \ell^z$, the dynamics is fractal with exponent z and $\delta r_\pm^2(\hat{t} \ll 1) \sim \text{const}$.

If an infinite cluster is present, the test particle at large time scales, $t \gg \xi^{d_w}$, is either localized in a finite cluster, or it moves on a homogeneously looking infinite cluster. The latter results in normal diffusion, $\delta r_-(\hat{t} \gg 1) \sim \hat{t}^{1-2/z}$, which is characterized by a diffusion coefficient,

$$D = \lim_{t \rightarrow \infty} \frac{\delta r^2(t)}{2dt}. \quad (3.33)$$

From the scaling properties of the mean-squared displacement, it follows that D vanishes at the percolation threshold as,

$$D \sim (\ell^{-z})^{1-2/z} \sim |\varepsilon|^{(z-2)(\nu-\beta/2)}. \quad (3.34)$$

3.3 Universal Corrections to the Scaling Behavior

In this section, we give a unified description of scaling in the Lorentz problem that allows for a generalization including corrections to scaling. We recall from the preceding section the scaling form for the cluster distribution,

$$n_s(\varepsilon) = \zeta^{-d-d_f} n^\pm(s\zeta^{-d_f}), \quad (3.13)$$

as well as for the cluster-resolved van Hove correlation function, Eq. (3.27), which is rewritten as,

$$G_s(\mathbf{r}, t; \varepsilon) = \zeta^{-d} \tilde{\mathbf{G}}_F^\pm(r/\zeta, t\zeta^{-d_w}, s\zeta^{-d_f}). \quad (3.35)$$

In the percolating regime, the contribution of the infinite cluster has to be added,

$$G_\infty(\mathbf{r}, t; \varepsilon) = \zeta^{-d} \mathbf{G}_\infty(r/\zeta, t\zeta^{-d_w}). \quad (3.26)$$

This set of quantities contains the full statistical information of the system.

An even more general quantity that combines all information is the joint probability that a test particle is placed at an s -cluster at time $t = 0$ and has moved a distance \mathbf{r} after a time t ,

$$P_s(\mathbf{r}, t; \varepsilon) := s n_s(\varepsilon) G_s(\mathbf{r}, t; \varepsilon). \quad (3.36)$$

On the percolating cluster, we define,

$$P_\infty(\mathbf{r}, t; \varepsilon) := P_\infty(\varepsilon) G_\infty(\mathbf{r}, t; \varepsilon). \quad (3.37)$$

Integrating over \mathbf{r} yields the cluster distribution, since $G_s(\mathbf{r}, t; \varepsilon)$ is normalized to unity,

$$s n_s(\varepsilon) = \int d^d r P_s(\mathbf{r}, t; \varepsilon). \quad (3.38)$$

Furthermore, also the cluster-resolved van Hove function is contained in P_s ,

$$G_s(\mathbf{r}, t; \varepsilon) = \frac{P_s(\mathbf{r}, t; \varepsilon)}{\int d^d r P_s(\mathbf{r}, t; \varepsilon)} \quad (s \leq \infty). \quad (3.39)$$

The joint probability P_s obeys again scaling, and it is tempting to postulate an extended scaling Ansatz accounting for some irrelevant scaling variable u ,

$$P_s(\mathbf{r}, t; \varepsilon) = \zeta^{-2d} \mathcal{P}_F^\pm(r/\zeta, t\zeta^{-d_w}, s\zeta^{-d_f}, u\zeta^{-\omega}), \quad (3.40)$$

$$P_\infty(\mathbf{r}, t; \varepsilon) = \zeta^{d_f-2d} \mathcal{P}_\infty(r/\zeta, t\zeta^{-d_w}, u\zeta^{-\omega}). \quad (3.41)$$

The variable u can be thought of a parameter encoding the microscopic details of the system under consideration. This variable is connected with a new exponent ω which, in contrast to u , is again universal, i. e., independent of the microscopic details. This approach extends the scaling forms of both the cluster distribution, $n_s(\varepsilon)$, and the cluster-resolved van Hove function, $G_s(\mathbf{r}, t; \varepsilon)$. It introduces corrections to the scaling behavior and, at the same time, relates the corrections for both quantities to each other. The scaling form for the cluster distribution follows as,

$$n_s(\varepsilon) = \zeta^{-d-d_f} \mathcal{N}^\pm(s\zeta^{-d_f}, u\zeta^{-\omega}), \quad (3.42)$$

where \mathcal{N}^\pm is analytic in its second argument. Expanding in this argument yields,

$$n_s(\varepsilon) = \zeta^{-d-d_f} n^\pm(s\zeta^{-d_f}) [1 + \zeta^{-\omega} n_1^\pm(s\zeta^{-d_f})], \quad (3.43)$$

with another correction function n_1^\pm . Specifying to the critical point, i. e., $s\zeta^{-d_f} \rightarrow 0$, yields,

$$n_s(\varepsilon \rightarrow 0) \sim s^{-\tau} (1 + A s^{-\Omega}). \quad (3.44)$$

We identify $\Omega := \omega/d_f$ as the correction exponent that has been measured by *Lorenz and Ziff (1998)* for lattice percolation in three dimensions, $\Omega = 0.64 \pm 0.02$.

The extended scaling form of the van Hove correlation function is inferred as follows,

$$G(\mathbf{r}, t; \varepsilon) = \sum_s s n_s(\varepsilon) G_s(\mathbf{r}, t; \varepsilon) + P_\infty(\varepsilon) G_\infty(\mathbf{r}, t; \varepsilon) \quad (3.45)$$

$$= \sum_s P_s(\mathbf{r}, t; \varepsilon) + P_\infty(\mathbf{r}, t; \varepsilon) \quad (3.46)$$

$$\approx \int ds \zeta^{-2d} \mathcal{P}_F^\pm(r/\zeta, t\zeta^{-d_w}, s\zeta^{-d_f}, u\zeta^{-\omega}) \quad (3.47)$$

$$+ \zeta^{d_f-2d} \mathcal{P}_\infty(r/\zeta, t\zeta^{-d_w}, u\zeta^{-\omega}).$$

Both terms contribute equally, and we arrive with the hyperscaling relation, Eq. (3.11), at

$$G(\mathbf{r}, t; \varepsilon) = \zeta^{-d-\beta/v} \mathcal{G}^\pm(r/\zeta, t\zeta^{-d_w}, u\zeta^{-\omega}). \quad (3.48)$$

One readily obtains for the mean-square displacement,

$$\delta r^2(t; \varepsilon) = \int d^d r r^2 G(\mathbf{r}, t; \varepsilon) \quad (3.49)$$

$$= \xi^{2-\beta/\nu} \tilde{\mathcal{R}}_{\pm}^2(t \xi^{-d_w}, u \xi^{-\omega}), \quad (3.50)$$

making use of Eq. (3.30),

$$= t^{2/z} \mathcal{R}_{\pm}^2(t \ell^{-z}, u t^{-y}), \quad (3.51)$$

with the dynamic correction-to-scaling exponent,

$$y = \frac{\omega}{d_w} = \frac{\Omega d_f}{d_w}. \quad (3.52)$$

Expanding \mathcal{R}_{\pm}^2 in its second argument and specializing to the critical point, $t \ell^{-z} \rightarrow 0$, yields the correction to the critical law,

$$\delta r^2(t; \varepsilon = 0) \sim t^{2/z} (1 + C t^{-y}). \quad (3.53)$$

Our derivation of these corrections reveals its physical origin: it lies in the presence of a microscopic scale that cuts off the universal asymptotic properties. The amplitude C depends on these microscopic details, the exponent y is universal and related to static corrections. For the Lorentz model in three dimensions, we calculate $y \approx 0.34 < 1$, hence the correction term is not spoiled by analytic corrections. For diffusion on lattice percolation clusters, the walk dimension is smaller, $d_w^{\text{lat}} \approx 3.8$, and the dynamic correction exponent evaluates to $y^{\text{lat}} \approx 0.43$.

4 Dynamics Close to the Transition

Abstract

The dynamics of tracer particles between overlapping spheres slows critically down as a certain obstacle density n_c is approached. The essential physics of this localization phenomenon is described in terms of the percolation transition of the void space. We give a short review on the mapping between the Lorentz model and continuum percolation and on the origins of the hyperscaling relation for the conductivity exponent. Molecular Dynamics simulations are used to corroborate the mapping. A finite-size scaling analysis for the diffusion coefficient provides an accurate measurement of the critical density which collapses with the percolation threshold of the void space. A spatial resolution of the dynamics, i. e., analysis of the van Hove function, demonstrates the coexistence of localized and diffusing particles. Further, the behavior of the non-ergodicity parameters close to the transition is discussed.

4.1 Continuum Percolation

Mapping to random resistor networks

The underlying medium of the Lorentz model undergoes at high obstacle densities a percolation transition with the peculiarity that the percolating clusters are continuous geometric objects. It has been argued that dynamic properties of the medium such as conductivity or elasticity obey different critical properties than on lattices (*Halperin et al.*, 1985). This argumentation is based on the following mapping of the medium to a random resistor network (Fig. 4.1):

- (i) Construct a Voronoi tessellation around the obstacle centers which defines vertices being connected through edges. In three dimensions, each vertex either defines a “chamber” between the obstacles or is outside the void space. Each edge or bond defines a “gap” between three obstacles

at a time. (The plane through these obstacle centers separates adjacent chambers.) If a gap is blocked by these obstacles, remove the related bond. Then, any path in the void space can be transformed continuously into a path along the bonds without crossing the obstacles (*Kerstein, 1983*).

- (ii) Fix a chamber and one of its gaps. A transition rate W can be assigned to this gap which is given as the ratio of the phase space volume available for leaving through the gap to the total volume V of the chamber. The former is proportional to the cross-section area of the gap A , it holds $W \propto A/V$ (*Machta and Moore, 1985*). The transport properties of the Lorentz model depend only on the probability distribution $\rho(W)$ of small transition rates W . It turns out that $\rho(W)$ exhibits a singularity for small W which is merely determined by the distribution of small cross-sections A or narrow gaps; the volume V plays a minor role. In d dimensions, one calculates (*Machta and Moore, 1985*)

$$\rho(W) \sim W^{-\alpha}, \quad \text{where} \quad \alpha = \frac{d-2}{d-1}. \quad (4.1)$$

- (iii) Finally, drop the obstacles and keep only vertices and bonds in the void space, and interpret the transition rates through the gaps as conductances along the bonds. This defines the random resistor network with a fractal, i. e., power-law, distribution of the weak conductances.

Such random resistor networks have been investigated extensively by means of Monte-Carlo simulations (*Derrida et al., 1984; Gingold and Lobb, 1990*) and renormalization group techniques (*Harris et al., 1984; Lubensky and Tremblay, 1986*), providing reliable numeric and analytic results for the critical behavior (*Havlin and Ben-Avraham, 2002*).

Conductivity

In particular, the conductivity Σ of random resistor networks has been studied. As the infinite cluster becomes increasingly thinner upon approaching the threshold, the conductivity vanishes as well with a power law, $\Sigma \sim |\varepsilon|^\mu$, defining another exponent μ .

The fact that the percolating network looks homogeneous at length scales larger than the correlation length ξ is expressed in the “links, nodes and blobs”

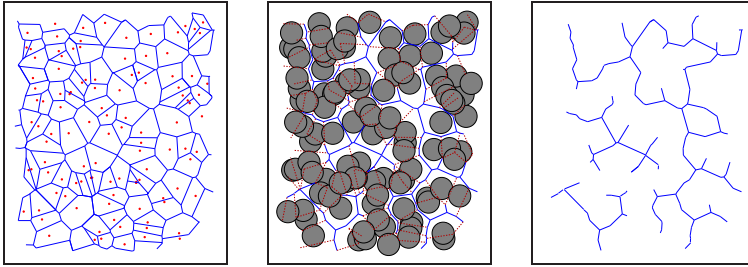


Figure 4.1 Mapping of the Lorentz model to a random resistor network. (Cartoons are in two dimensions.)

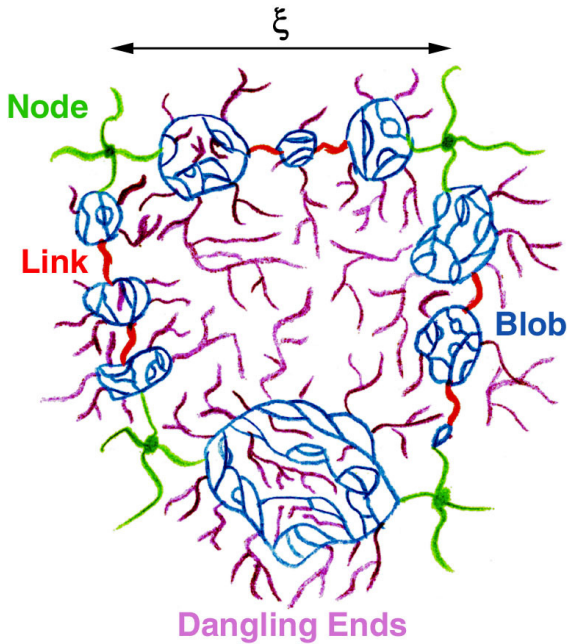


Figure 4.2 Cartoon of the nodes-links-blobs model: nodes, being distributed homogeneously with average spacing ξ , are connected by chains. A chain is made of a series of links and blobs; links are defined as bonds carrying the whole current of a chain. Most bonds of the network are dangling sites, i. e., they carry zero current.

model (Fig. 4.2) by *Skal* and *Shklovskii* (1975) and *de Gennes* (1976); for reviews see (*Nakayama et al.*, 1994) and the book by *Stauffer* and *Aharony* (1994). It simplifies the infinite cluster of the percolating network in the following way: the nodes are defined as vertices which can not be isolated from the cluster by cutting any two (not necessarily adjacent) bonds. The nodes are supposed to be distributed homogeneously with an average spacing of the correlation length ζ . Most vertices of the network belong to cul-de-sacs (“dangling ends”), i. e., they can be separated by cutting a single bond somewhere in the network. Nodes are connected by chains, i. e., objects that can be isolated by cutting two bonds adjacent to a node. A fraction of the bonds of a chain carries the whole current (“links” or “red bonds”), the remaining bonds of a chain form “blobs” which connect two links at a time.

The chains have an average resistance \mathcal{R} which diverges as the threshold is approached with a power law defining the exponent ζ ,

$$\mathcal{R} \sim |\varepsilon|^{-\zeta}. \quad (4.2)$$

Applying an electric field E , the potential drop between two nodes is of order ζE yielding a chain current $I = \zeta E / \mathcal{R}$. Then, the current density in the network is given by $j = I / \zeta^{d-1}$. Plugging in the definition of the conductivity, $j = \Sigma E$, yields $\Sigma \sim \zeta^{2-d} / \mathcal{R}$, and a hyperscaling relation follows,

$$\mu = (d - 2)\nu + \zeta. \quad (4.3)$$

The remaining task is to identify the exponent ζ for such random resistor networks that are relevant for the Lorentz model, i. e., that exhibit a power-law distribution of the conductances, $\rho(W) \sim W^{-\alpha}$ with $0 \leq \alpha < 1$. We will follow the argumentation of *Straley* (1982). The distribution of chain conductances $\rho_{\text{chain}}(W)$ can be considered as the renormalized distribution of bond conductances $\rho(W)$ in the sense of the real space renormalization group. The renormalization flow shifts the whole distribution; usually, the peak of the renormalized distribution $\rho_{\text{chain}}(W)$ is determined by the peak of the microscopic distribution $\rho(W)$. The low-conductivity tail, however, is shifted as well. Two different scenarios arise dependent on the value of α : either the peak absorbs the tail, yielding the universal form of the renormalized distribution, or the tail pulls weight out of the peak, leading to a final distribution with the same small- W tail, $\rho_{\text{chain}}(W) \sim W^{-\alpha}$. In the first scenario, the exponent for the chain resistance is found to be universal, ζ^{univ} . In the second scenario, the chain resistance is determined by the small conductances. The total resistance of parallel bonds, i. e., the blobs, can be neglected against the resistance

of the red bonds, and $\rho_{\text{chain}}(W)$ obeys for small W ,

$$\rho_{\text{chain}}(W) \sim N_{\text{red}}\rho(W), \quad (4.4)$$

where N_{red} is the number of red bonds within a chain. Dimensional analysis suggests a scaling form,

$$\rho_{\text{chain}}(W) = W_0^{-1} \tilde{\rho}_{\text{chain}}(W/W_0), \quad (4.5)$$

where W_0 denotes the typical chain conductance. From Eq. (4.4) one infers, $N_{\text{red}} \sim W_0^{\alpha-1}$, and the average chain resistance $\mathcal{R}^{-1} = \langle 1/W \rangle$ is identified with W_0 . For the divergence of the number of red bonds, we finally employ a result by *Coniglio* (1981),

$$N_{\text{red}} \sim |\varepsilon|^{-1}, \quad (4.6)$$

yielding $\zeta = (1 - \alpha)^{-1}$. It has been argued that the cross-over between both scenarios occurs such that (*Machta et al.*, 1986; *Straley*, 1982)

$$\zeta = \max \left[(1 - \alpha)^{-1}, \zeta^{\text{univ}} \right]. \quad (4.7)$$

Without resorting to the assumptions of the “links, nodes and blobs” model, *Stenull* and *Janssen* (2001) have proven directly by means of an expansion of the renormalization group equations in $\varepsilon = 6 - d$ to arbitrary order the equivalent relation,

$$\mu = \max \left[(d - 2)\nu + (1 - \alpha)^{-1}, \mu^{\text{lat}} \right], \quad (4.8)$$

where μ^{lat} is the universal exponent for lattice percolation.

From simulations, it is known that $1 \leq \zeta^{\text{univ}} \lesssim 1.3$ for $d \geq 2$ dimensions (*Stauffer* and *Aharony*, 1994). Using the above value of α for the Lorentz model, Eq. (4.1), it follows that ζ takes its universal value on lattices only for $d = 2$ dimensions, otherwise, $\zeta = d - 1$. Furthermore, the dynamic exponent z of anomalous diffusion of the Lorentz model which is connected with ζ via Eqs. (4.14) and (4.3), is not an independent exponent anymore for $d \geq 3$. Rather it can be calculated from the geometric exponents ν and β which are believed to equal their universal lattice values (*Elam et al.*, 1984); in three dimensions, we use $\nu = 0.88$ and $\beta = 0.41$ (*Stauffer* and *Aharony*, 1994) throughout this work.

4.2 The Mean-Square Displacement

Molecular Dynamics simulations allow for a direct numerical analysis of the dynamic properties of the Lorentz model without resorting to random resistor networks. A quantitative description over the full density range becomes accessible, in particular, we focus on both sides of the critical region.

Molecular Dynamics simulations

The hard-core potential of the obstacles allows for an event-oriented algorithm for the Molecular Dynamics simulation. Since the particle propagates freely between subsequent collisions, calculating the collision points only is sufficient. A possible collision of the the particle at \mathbf{r} with velocity \mathbf{v} against a single obstacle in the coordinate origin occurs after the time¹

$$t_{\text{coll}} = -\frac{b}{v^2} - \frac{1}{v^2} \sqrt{b^2 - v^2(r^2 - \sigma^2)}, \quad (4.9)$$

where $b = \mathbf{v} \cdot \mathbf{r}$. If $b > 0$, the particle departs from the obstacle and no collision will take place. If the radicand becomes negative, the particle misses and there won't be any collision at all. The particle velocity \mathbf{v}' after the collision is reflected at the surface of the obstacle,

$$\mathbf{v}' = \mathbf{v} - 2(\mathbf{v} \cdot \hat{\boldsymbol{\sigma}}) \hat{\boldsymbol{\sigma}}, \quad (4.10)$$

where $\hat{\boldsymbol{\sigma}} = (\mathbf{v}t_{\text{coll}} + \mathbf{r})/\sigma$ specifies the surface normal at the collision point. The employed algorithm is straightforward. In a preparation step, the obstacle positions, the initial particle position and its (normalized) velocity are drawn from a uniform distribution under the constraint that the particle starts in the void space. The box is divided into cubic cells of length L_{cell} , and each obstacle is associated uniquely with a cell. Then, the trajectory of the particle is calculated following the steps in Fig. 4.3.

Since a single trajectory can consist of several billion collisions, one easily runs out of computer memory if one would store the complete trajectory. A very efficient blocking scheme [“order-n algorithm” in (Frenkel and Smit, 2001)] takes care of this issue by arranging the trajectory on a logarithmic time grid and simultaneously calculating various correlation functions $C(t; t_0)$. The

¹The numerical error can be reduced using $t_{\text{coll}} = q/v^2, (r^2 - \sigma^2)/q$, where $q = -b + \sqrt{b^2 - v^2(r^2 - \sigma^2)}$ and $b < 0$. This formula avoids the calculation of the difference between two almost equal numbers which would occur for $b^2 \gg v^2(r^2 - \sigma^2)$.

1. Determine the index of the cell which the particle currently traverses
2. Calculate collision times for all obstacles in that cell and its adjacent neighbor cells in virtue of Eq. (4.9)
3. Is there any collision within these cells and which collision will occur next?
4. Increment timer by t_{coll} and update particle position and velocity according to Eq. (4.10), or let the particle simply travel straight on over a distance $L_{\text{cell}} - \sigma$
5. In case the particle has left the volume: impose periodic boundary conditions to the particle position and update an additional offset variable
6. Loop to No. 1 until final time is reached

Figure 4.3 Molecular Dynamics algorithm for the simulation of a single particle trajectory.

algorithm already averages over different time origins t_0 (“moving time average”), which, however, are not necessarily uncorrelated, especially for short time intervals $t - t_0$. Hence, we will not infer any estimate of the statistical error from this averaging procedure. Rather, a set of N_t trajectories with different initial positions for each of N_r different realizations of the obstacle disorder is simulated, and the statistical error is estimated from $N_t \times N_r$ independent measurements. At each density, we have simulated at least $N_r = 20$ realizations of the disorder. At intermediate densities, the total number of trajectories has been chosen $N_t \times N_r = 100$. This value has been increased up to 600 at very high densities, where the phase space is highly decomposed into small, disconnected parts. The longest trajectories span about a billion collisions, the demand on CPU time of a 1 GHz Alpha EV 6.8 processor for such a trajectory was about one day.

All numerical results presented in this work refer to fixed dimensionality, $d = 3$. The simulation box has periodic boundaries, its linear size was chosen as $L = 200\sigma$. A detailed finite-size analysis is presented in Section 4.3.

The long-time limit: diffusion and localization

The following discussion is based on measurements of the mean-square displacement of the test particle,

$$\delta r^2(t) = \left\langle |\mathbf{R}(t) - \mathbf{R}(0)|^2 \right\rangle. \quad (4.11)$$

In principle, the Lorentz model is a deterministic system. The initial velocity of the test particle, however, is quickly randomized through subsequent collisions with the scatterers, leading to diffusive motion. This randomization is not related to the random distribution of obstacles, it occurs also if the obstacles were on a lattice. In $d = 3$ dimensions, the mean free path l between the collisions follows from $\pi \sigma^2 l = 1/n$ since the differential scattering cross-section is isotropic. Employing the estimate for the diffusion coefficient $D_0 = vl/d$, the leading order of the low-density expansion from kinetic theory (Weijland and van Leeuwen, 1968) is recovered,

$$D_0 = \frac{v\sigma}{3\pi n^*}. \quad (4.12)$$

For higher densities, the collisions become correlated leading to non-analytic, logarithmic correction terms.

Close to the critical density, the dynamics can be understood as a hopping process at scales much larger than the correlation length ξ . We restrict the particle to the percolating void space; then, the hopping occurs between the nodes of the network (see Section 4.1), and ξ is the lattice constant. Along the (fractal) chains of the network, the dynamics exhibits anomalous diffusion characterized by the walk dimension $d_w > 2$, and the time scale associated with ξ obeys $t_\xi \sim \xi^{d_w}$. For long times, $t \gg t_\xi$, the dynamics becomes diffusive and the mean-square displacement obeys $\delta r^2(t) \simeq 2dDt$ defining the diffusion coefficient D . Since the diffusion coefficient vanishes for localized particles, the probability to be on the percolating void space has to be accounted for yielding an additional factor $P_\infty \sim |\varepsilon|^\beta$. Upon approaching the critical density, the diffusion coefficient is found to vanish as,

$$D \sim |\varepsilon|^\beta \xi^{z2}/t_\xi \sim |\varepsilon|^\beta \xi^{2-d_w}. \quad (4.13)$$

The phase space average involves both the percolating and finite clusters, therefore, the relevant dynamic length scale is the mean-cluster radius, $\ell \sim |\varepsilon|^{-\nu+\beta/2}$ and the dynamic exponent z characterizing anomalous diffusion, $\delta r^2(t) \sim t^{2/z}$, is different from d_w . It holds $\ell^z \sim \xi^{d_w}$ and $D \sim \ell^{2-z}$, see Section 3.2. Making use of the Einstein relation, $\Sigma \propto D$ (Havlin and Ben-Avraham, 2002), the diffusion coefficient vanishes with the same exponent μ as the conductivity and a scaling relation that connects μ with the dynamic exponent z follows,

$$z = \frac{2\nu - \beta + \mu}{\nu - \beta/2}. \quad (4.14)$$

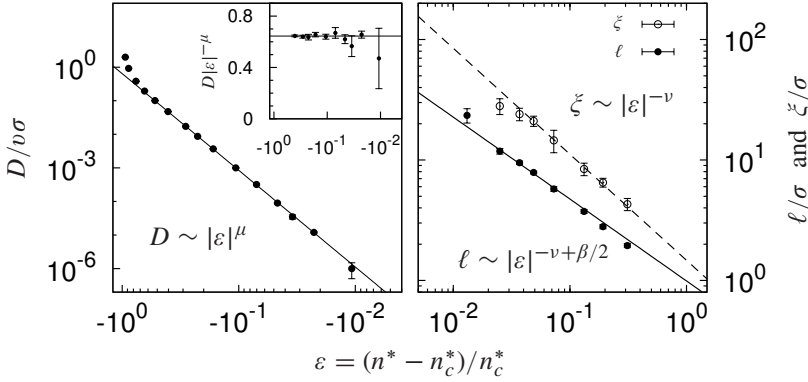


Figure 4.4 As the localization transition is approached, the diffusion coefficient D vanishes with exponent $\mu = 2.88$. The localization length ℓ diverges with exponent $\nu - \beta/2$ and can clearly be distinguished from the correlation length, $\zeta \sim |\varepsilon|^{-\nu}$.

In the localized regime, the long-time limit of the mean-square displacement yields directly the mean cluster radius, $\delta r^2(t) \simeq \ell^2$ for $t \gg t_\xi$. The correlation length ζ is easily accessible in the localized regime by the observation that the mean-quartic displacement, $\delta r^4(t) := \langle |\Delta \mathbf{R}(t)|^4 \rangle$, scales for long times as (Chapter 2)

$$\delta r^4(t) \simeq \zeta^2 \ell^2 \quad \text{for } t \gg t_\xi. \quad (4.15)$$

We have simulated trajectories of the test particle over a wide range of obstacle densities, above and below the localization transition. From the long-time limit of $\delta r^2(t)$ we have extracted the diffusion coefficient D which vanishes as a critical density n_c^* is approached from below. The power law, $D \sim |n^* - n_c^*|^\mu$, is observed over five orders of magnitude (Fig. 4.4).

The conjectured mapping between continuum percolation and the localization transition of the Lorentz model can be tested by means of Eq. (4.8), which provides together with the result $\alpha = \frac{1}{2}$ from *Machta and Moore (1985)* a value for the exponent $\mu = \nu + 2 \approx 2.88$. Further, we can test the deviation of μ from its value on lattices, $\mu^{\text{lat}} \approx 2.0$ (*Stauffer and Aharony, 1994*), as well as the competing result of *Halperin et al. (1985)*, $\mu = \nu + 3/2$. Using Eq. (4.14), these predictions are connected with different exponents z for the anomalous diffusion which are tested directly on the mean-square displacement at the nearly-critical density $n^* = 0.84$, see Fig. 4.5. The inset of the figure compares rectification plots of the diffusion coefficient with the various

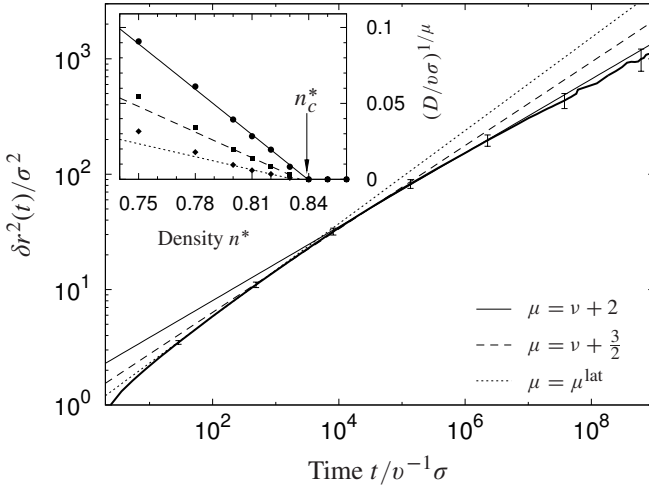


Figure 4.5 Anomalous diffusion of the mean-square displacement at $n^* = 0.84$; straight lines represent power laws $t^{2/z}$ where z is related to μ by Eq. (4.14). We compare three possibilities for the value of μ : the scaling relations $\mu = \nu + 2$ (Machta and Moore, 1985) and $\mu = \nu + 3/2$ (Halperin *et al.*, 1985) from Eq. (4.8), and the lattice value, $\mu^{\text{lat}} = 2.0$. Inset: rectification plot of the diffusion coefficient. The straight lines are fits to the four data points with $n^* \geq 0.80$.

values for μ , the best straight line is obtained for $\mu = 2.88$. We conclude that only the value $\mu = \nu + 2$ is consistent with our data, the other two possibilities can clearly be ruled out.

Knowing the value of μ , the critical density can be fitted quite precisely by means of the rectification plot, we obtain $n_c^* = 0.839(4)$. This value is much larger than the value $9/4\pi$ suggested in the literature (Götze *et al.*, 1981a). Our result for n_c^* coincides with the percolation threshold of the void space, $n_{\text{perc}}^* = 0.8363(24)$ (Elam *et al.*, 1984; Kertész, 1981; van der Marck, 1996; Rintoul, 2000), what can be interpreted in such a way that the particle will eventually squeeze through any, no matter how narrow gap. There are no regions, e. g. cul-de-sacs, on a cluster which are too improbable to be visited by the particle after an infinitely long time. This means further that the particle will diffuse as long as its surrounding phase space is connected with infinity.

In the localized regime, for densities above n_c^* , the divergence of the long-time limit of the mean-square displacement is compatible with an exponent

$\nu - \beta/2 = 0.68$, plugging in the exponents from lattice percolation in $d = 3$. In particular, we can identify the localization length ℓ with the mean-cluster radius introduced in Section 3.2 as already anticipated by the choice of our notation. Further, we have investigated the ratio $(\delta r^4(t)/\delta r^2(t))^{1/2}$, it diverges as $|\varepsilon|^{-\nu}$ and, hence, can be identified with the correlation length ζ , see Fig. 4.4. This result together with Eq. (4.15) not only corroborates the scaling form of $G(\mathbf{r}, t)$, Eq. (2.1), but also contrasts clearly the localization length ℓ with the correlation length ζ . In conclusion, two different length scales are present close to the critical density, and both are relevant for the dynamic properties.

4.3 Finite-Size Scaling

The size of the simulation box, L , limits the size of the largest finite clusters and, hence, acts as an upper cutoff on the correlation length, ζ . For very small system, $L \ll \zeta$, the correlation length becomes irrelevant, and the intrinsic (macroscopic) length scale is given by the box size. For very large systems, $L \gg \zeta$, the finiteness of the box can be neglected. Observables as well as the master functions are decorated with an additional parameter, L and L/ζ , resp. For the mean-square displacement, we extend the scaling Ansatz, Eq. (3.31),

$$\delta r^2(t; \varepsilon, L) = t^{2/z} \delta r_{\pm}^2(t \ell^{-z}, L/\zeta), \quad (4.16)$$

and infer for the diffusion coefficient,

$$D(\varepsilon, L) = \zeta^{-\mu/\nu} D^{\pm}(\zeta/L) \quad (4.17)$$

$$\sim \begin{cases} L^{-\mu/\nu} & \text{for } L \ll \zeta, \\ O(e^{-L/\zeta}) & \text{for } L \gg \zeta \text{ and } \varepsilon > 0, \\ |\varepsilon|^{\mu} & \text{for } L \gg \zeta \text{ and } \varepsilon < 0. \end{cases} \quad (4.18)$$

Note that in small systems, the diffusion coefficient becomes independent of ε close to the critical density.

Our simulation results not only corroborate the scaling form of $D(\varepsilon, L)$ very nicely, but also demonstrate the occurrence of two different master functions D^{\pm} distinguishing the regimes above and below n_c , see Fig. 4.6. The master function D^+ expresses the fact that diffusion is not blocked for $n^* > n_c^*$ as long as the box size is much smaller than the correlation length ($L \ll \zeta$). Due to the periodic boundary conditions, large finite clusters, $R_s \gg L$, are

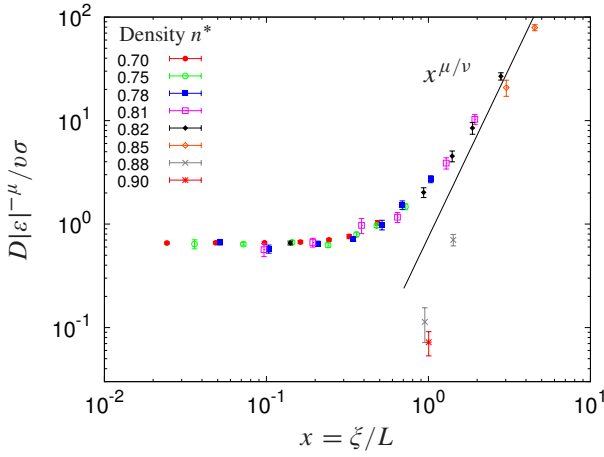


Figure 4.6 Rescaled diffusion coefficients collapse on the master functions $D^\pm(x)$ describing the finite-size effects.

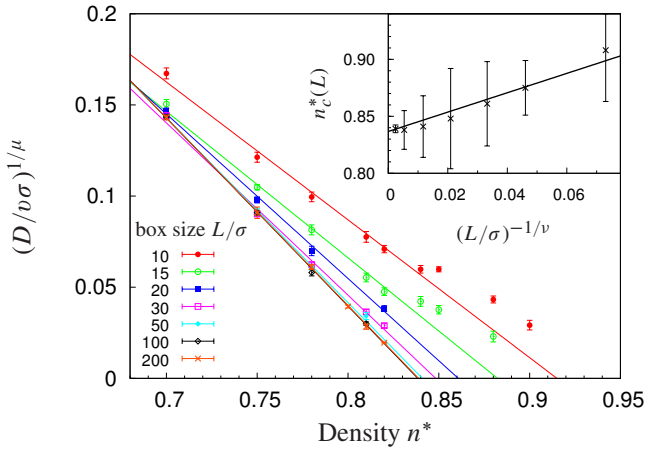


Figure 4.7 Rectification plots of the diffusion coefficient for various box sizes. The straight lines are fits to the data for $n^* \leq 0.82$, their zeros yield the effective critical densities $n_c^*(L)$. Inset: scaling of $n_c^*(L)$ and extrapolation to infinite systems.

turned into infinite clusters, yielding diffusing particles above n_c^* . In particular, the percolation threshold seems to be shifted towards the localized regime, i. e., the effective critical density $n_c^*(L)$, increases with decreasing box size, L . We have measured $n_c^*(L)$ as the axis intercept of the linear extrapolation of $D(n^*)^{1/\nu}$ (Fig. 4.7). The true critical density is approached as (Stauffer and Aharony, 1994)

$$n_c^*(L) - n_c^* \sim L^{-1/\nu}, \quad (4.19)$$

which is made plausible by the observation that the scaling variable ξ/L can also be expressed in terms of $|\varepsilon|L^{1/\nu}$.

The finite-size scaling allows for a more precise determination of the critical density yielding $n_c^* = 0.8367 \pm 0.0010$. We have checked that our result is robust against a possible error in the critical exponent ν of the order of 0.01. This finding improves our previous result, $n_c^* = 0.839 \pm 0.004$, for fixed box size, $L = 200\sigma$. It is compatible with the result from Rintoul (2000), $n_c^* = 0.8363 \pm 0.0024$.

4.4 Space-Resolved Dynamics

The van Hove correlation function

A complete statistical description of the dynamical properties of the Lorentz model is given in terms of the van Hove self-correlation function, $G(\mathbf{r}, t) = \langle \delta(\mathbf{R}(t) - \mathbf{R}(0) - \mathbf{r}) \rangle$. At fixed time t , this quantity can be interpreted as the probability density describing the distribution of a set of test particles that was placed at the coordinate origin $\mathbf{r} = 0$ at time $t = 0$. After averaging over the random obstacle configurations, the system is isotropic and $G(\mathbf{r}, t)$ depends only on the distance $r = |\mathbf{r}|$. Integrating out the dependence on the solid angle, we are left with the reduced correlation function, $\tilde{G}(r, t) = 4\pi r^2 G(\mathbf{r}, t)$.

In Fig. 4.8, it can be seen that already at densities well below the critical density, $\tilde{G}(r, t)$ exhibits two distinct peaks. One peak is of diffusive nature, it moves to larger distances with increasing time and vanishes finally. The second peak is located at small distances and remains fixed, it describes the localized particles. Writing

$$G(\mathbf{r}, t) = G_{\text{loc}}(\mathbf{r}, t) + G_{\text{diff}}(\mathbf{r}, t), \quad (4.20)$$

the amount of localized particles is quantified by

$$f_0 := \int d^d r G(\mathbf{r}, t \rightarrow \infty) = \int d^d r G_{\text{loc}}(\mathbf{r}, t). \quad (4.21)$$

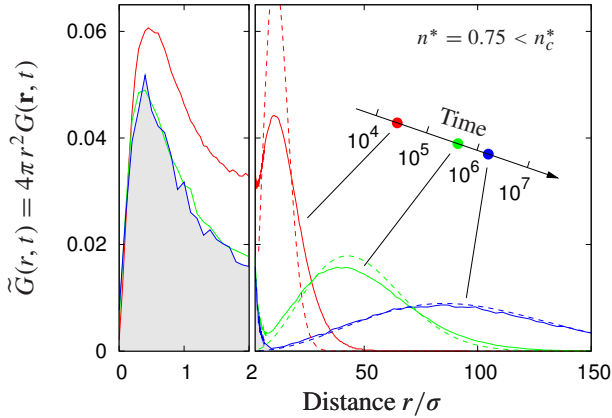


Figure 4.8 Time evolution of the reduced van Hove function $\tilde{G}(r, t)$ at a high density, but far from criticality, $n^* = 0.75$. It exhibits two peaks, a diffusive peak vanishing for large times and a sharp peak at short distances. Dashed lines: the solution of the diffusion equation approximates the diffusive peak. The shaded area represents the trapped particles which make about $f_0 = 8\%$ in the present case.

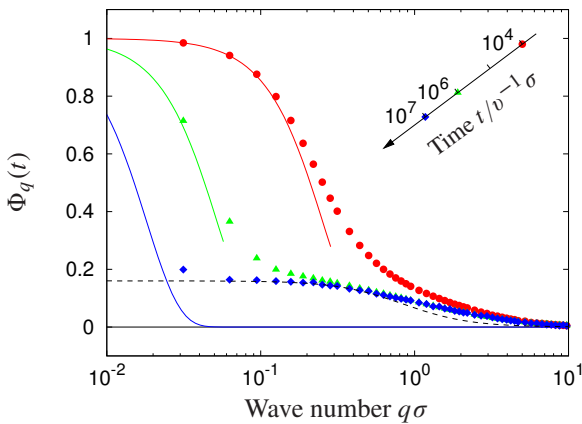


Figure 4.9 Time evolution of the incoherent intermediate scattering function $\Phi_q(t)$ at an exemplary density $n^* = 0.78$. Solid lines show the Gaussian approximation, Eq. (4.24). At long times, the non-ergodicity parameter f_q remains, the dashed line is a fit to the Lorentzian, Eq. (4.26).

The second equality holds at all times since $G_{\text{diff}}(\mathbf{r}, t \rightarrow \infty) \equiv 0$ and since localized particles cannot become diffusive and vice versa. Fig. 4.8 demonstrates that for long time and length scales, $t \gg \ell^z$ and $r \gg \xi$, the diffusive peak indeed can be described by the result of the three-dimensional diffusion equation,

$$G_{\text{diff}}(\mathbf{r}, t) = \frac{1 - f_0}{(4\pi D_\infty t)^{3/2}} \exp\left(-\frac{r^2}{4D_\infty t}\right). \quad (4.22)$$

The normalization factor has been modified taking into account the presence of non-diffusing particles; consequently, the correct diffusion coefficient is $D_\infty = D/(1 - f_0)$ for particles on the infinite cluster. Deviations at short time and length scales are attributed to the fractal structure of the percolating cluster at distances smaller than ξ .

Non-ergodicity parameters

Scattering experiments give access to the incoherent intermediate scattering function, $\Phi_{\mathbf{q}}(t)$, which is simply the Fourier transform of the van Hove function,

$$\Phi_{\mathbf{q}}(t) := \left\langle e^{i\mathbf{q} \cdot [\mathbf{R}(t) - \mathbf{R}(0)]} \right\rangle = \int d^d r e^{i\mathbf{q} \cdot \mathbf{r}} G(\mathbf{r}, t). \quad (4.23)$$

As well as the van Hove function, the scattering function is isotropic and, hence, depends only on the magnitude of the wave vector $q = |\mathbf{q}|$. Only the localized particles contribute to the long-time limit of the scattering function, $f_q := \Phi_q(t \rightarrow \infty)$; it is called non-ergodicity parameter since it measures the disconnectivity of the phase space. It vanishes in systems without localized particles, e. g., in fluids, otherwise the limit $f_{q \rightarrow 0} = f_0$ yields the fraction of localized particles as anticipated by the choice of our notation.

In liquids, sometimes a cumulant expansion is applied to the correlation function $\Phi_q(t)$, the latter being interpreted as the moment-generating functional of the probability distribution $G(\mathbf{r}, t)$ (Boon and Yip, 1991). Systems *without memory* yield Gaussian correlation functions, they are well described by the leading order of this expansion,

$$\Phi_q(t) \approx \exp\left[-\frac{1}{6}q^2 \delta r^2(t)\right]; \quad (4.24)$$

the Lorentz model, however, exhibits strong memory effects as indicated by the divergence of the non-Gaussian parameter (Chapter 2), and the approximation is only trivially valid for small arguments of the exponential, $q^2 \ll$

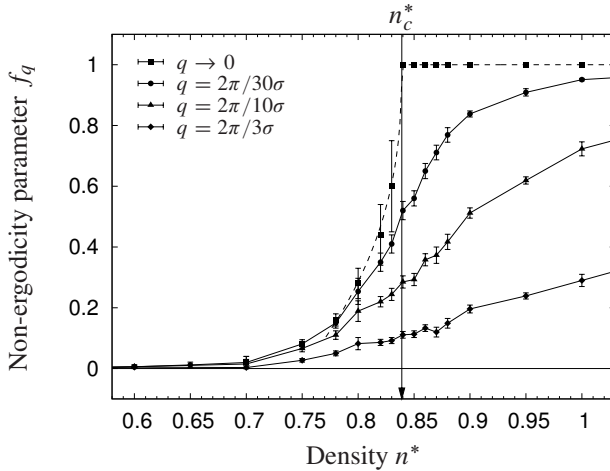


Figure 4.10 Density-dependence of the non-ergodicity parameter f_q . The values for f_0 (black squares) result from fits to Eq. (4.26) extrapolating $q \rightarrow 0$; the dashed line is a fit to the singular behavior, Eq. (4.27), and solid lines are guides to the eye.

$6/\delta r^2(t)$. The memory effects become apparent in particular for long times, i. e., $t \gg \ell^z$, where the localized particles have completely explored their clusters, and their contribution has already attained its long-time limit f_q . Since the linear size of the finite clusters is limited by the correlation length ξ , the non-ergodicity parameters are constant, $f_q \simeq f_0$ for $q \ll \xi^{-1}$. Fourier transformation of Eq. (4.20) and using Eq. (4.22) yields,

$$\Phi_q(t) = (1 - f_0) \exp(-D_\infty q^2 t) + f_q \quad \text{for } t \gg \ell^z. \quad (4.25)$$

At these time scales, it holds $D_\infty t \gg D_\infty \ell^z \sim \xi^2$, making use of Eq. (4.13), and the scattering function splits in two different parts near $q \approx \xi^{-1}$, see Fig. 4.9. The non-vanishing part at long wave numbers stems from the localized particles, whereas the short wave numbers describe the diffusive particles; the latter regime, however, being modified by a constant contribution f_0 . Only in the small regime $q \ll 1/\sqrt{D_\infty t} \ll \xi^{-1}$, shrinking with elapsing time, Eq. (4.25) is equivalent with the Gaussian approximation, Eq. (4.24).

For small wave numbers the non-ergodicity parameter takes the generic form of a Lorentzian (Götze *et al.*, 1981b),

$$f_q = \frac{f_0}{1 + \frac{1}{6}(q\ell)^2}; \quad (4.26)$$

its inverse width defines the localization length ℓ . We have determined the values for f_0 and ℓ by fitting our data for f_q to this form. In the localized regime, the values for ℓ collapse with those obtained from the long-time limit of the mean-square displacement.

For $n > n_c^*$, and at the localization transition in particular, all particles are trapped, and it holds $f_0 = 1$. This value is approached from the diffusive regime ($n^* < n_c^*$) as the volume of the percolating cluster vanishes. The fraction of diffusing particles is given by $1 - f_q$; it equals the probability that a particle is in the infinite cluster,

$$1 - f_0(\varepsilon) = P_\infty(\varepsilon) \sim |\varepsilon|^\beta. \quad (4.27)$$

Hence, f_0 exhibits a singularity at the transition which is qualitatively reproduced by our data, though the error bars are large (Fig. 4.10). Making use of Eq. (4.26), the singular behavior is also found at finite wave numbers,

$$f_q(\varepsilon) \sim f_q(0) + O(|\varepsilon|^\beta) \quad \text{for } \varepsilon < 0, \quad (4.28)$$

yielding a small kink in f_q ; its experimental observation, however, will be difficult.

Part II

Rod-Like Macromolecules

5 Dynamics of a Rod in the Dilute Limit

Abstract

A simplified model for the dynamics of a semi-dilute solution of rigid rods is introduced. It is closely related to the Lorentz model and describes the two-dimensional motion of a needle in an disordered static environment of point obstacles. We give a theoretical description of the dynamics within the Boltzmann approximation of uncorrelated collisions. In particular, we obtain results for the diffusion coefficients of center-of-mass motion and of rotation, which are valid in the low density regime.

5.1 Introduction

Semi-dilute solutions of stiff polymers as well as macromolecular liquids show distinct dynamical properties due to entanglement effects, that is due to the topological constraint that polymer chains cannot pass through one another. These dynamical features, however, depend sensitively on a variety of parameters such as the specific interaction between the polymers, hydrodynamic interactions, the ratio between polymer diameter and length and the stiffness. Therefore, it is of importance to establish simplified theoretical models allowing for disentangling the influence of the different parameters.

A very appealing and challenging model is a liquid of rigid, thin needles, i. e., the polymers are roughly approximated as rigid and treated in the limit of vanishing diameter. Biopolymers such as F-actin come close to this limit: its diameter is about 5 nm while filament lengths range from several microns to 20 μm and more, e. g., in the cell cortex (*Alberts et al.*, 2002). The latter has to be compared with a persistent length of about 17 μm (*Le Goff et al.*, 2002). A concentrated solution of thin needles fulfills the requirements of a semi-dilute polymer solution: strong entanglement and the absence of excluded volume interactions. Since the static properties of such a system are trivially those of an ideal gas, purely dynamic effects such as entanglement can be

studied in isolation. In particular, the model does not allow for a nematic phase transition.

A first theoretical description of solutions of rod-like polymers is due to *Doi* and *Edwards* (1978, 1986); using a tube model, they predict a strong suppression of the rotational diffusion coefficient with length L and number density n : $D_{\text{rot}} \sim (nL^3)^{-2}$. The tube is defined through the steric hindrance of a test polymer by the surrounding polymers; the test polymer is restricted to move mainly back and forth inside the tube. There, it can change its orientation only very little, and in order to rotate, it has to disengage from its tube being, however, confined in another tube. The formation of an adjacent tube is strongly correlated with the previous one. Consequently, a large number of tubes is necessary for the polymer to change its orientation macroscopically.

The needle liquid was investigated in early computer simulations by *Frenkel* and *Maguire* (1981, 1983). Being, however, limited to rather dilute situations, their data do not allow to draw any conclusions about the high density behavior. Nevertheless, they make an interesting prediction using scaling arguments that the coefficient of center-of-mass diffusion should diverge at high densities, i. e., in highly entangled situations, as $D_{\text{cm}} \sim (nL^3)^{1/2}$. The cross-over to the semi-dilute regime was studied a few years later (*Magda et al.*, 1986), hinting at an exponent -2 in the rotational diffusion D_{rot} . But an exploration of the power law over several decades is strongly limited by the huge demand on computer resources for the model. In Chapter 6, we will present Molecular Dynamics simulations for a simplified model which allows for a thorough investigation of the high density regime.

Another approach was chosen by *Doi et al.* (1984) in order to confirm the tube model. For the simulation of needles in a solvent, i. e., with Brownian dynamics, they use a Monte Carlo algorithm with an *ad hoc* reflection rule accounting for the collisions. The obtained results reflect the onset of the asymptotic high-density behavior of D_{rot} with the predicted exponent. Other Brownian dynamics simulations lift the limit of thin needles and use a soft interaction potential (*Bitsanis et al.*, 1988, 1990; *Fixman*, 1985), and it is not clear how much these results are spoiled by excluded volume effects. These simulations cover only the cross-over to the semi-dilute regime, but the data are well described by a theory based on binary interactions (*Fixman*, 1985).

Next to the tube model, there are only a few theoretical approaches to the needle liquid. We mentioned already the description of the cross-over regime. A more elaborate theory was derived recently within a Boltzmann-Enskog approximation (*Otto et al.*, 2006) explaining from a microscopic point of view

anisotropic diffusion. However, the theory is applicable only in the dilute regime. Another interesting theory modifies the model by fixing the center of mass positions of the needles on a simple cubic lattice, thus freezing the translational degrees of freedom (Schilling and Szamel, 2003a,b). The needles are much longer than the lattice constant and hinder mutually their free rotation. This model is predicted to undergo a glass transition being fundamentally different from structural glass formers due to the absence of static correlations.

A different line of approach simplifies the liquid of rod-like polymers further in order to capture the main features of entangled dynamics: It focuses on the dynamics of a single rod freezing the positions of all others. Further, the motion of this rod is restricted to a plane, which is riddled by the other rods. Effectively, the model describes a single rod moving in a static, random array of fixed disks—a variant of the Lorentz model with a highly anisotropic test particle.

A first investigation of this model was based on Molecular Dynamics simulations. *Moreno and Kob* (2004a,b) used a soft interaction potential and imitated the rod by a string of linearly aligned beads (“shish kebab”). They studied the breakdown of the isotropy of rotational dynamics close to the cross-over to the semi-dilute regime, i. e., when the mesh size between the obstacles becomes comparable with the rod length. Besides, they found a suppression of rotational diffusion, being compatible with the predictions of a two-dimensional variant of the tube model, and an increase of the translational diffusion coefficient by a factor two compared to the Boltzmann result.

5.2 Definition of the Model

We investigate a model similar to the one mentioned in the preceding paragraph, reducing the number of parameters to one. Instead of a soft potential and the shish kebab-like rod, the rod interacts with the obstacles via a hard potential. Since all excluded volume can be assigned to the obstacles, we reduce the rod to a needle avoiding all ambiguities about its detailed modeling. Further, we restrict to the limit of point obstacles—thus, the model corresponds to the liquid of thin needles.¹ In this limit, the void space formed by the obstacles does not undergo a percolation transition. Thereby, we avoid the whole scenario of critical slowing down as known from the usual Lorentz model; the

¹We are grateful to Rolf Schilling for pointing out this particularly interesting limit of our model.

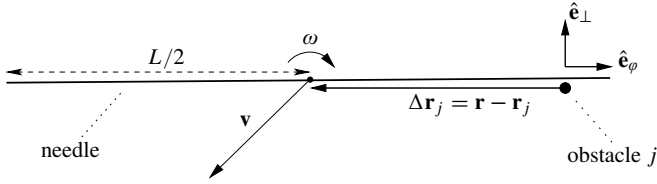


Figure 5.1 Geometry for the derivation of the law of collision.

dynamic effects are not spoiled and can be studied in great detail.

In conclusion, our model describes a needle of length L moving ballistically in a two-dimensional environment of randomly distributed, fixed point obstacles of number density n . The needle has a mass m and its moment of inertia with respect to rotations about the midpoint is given by $I = am(L/2)^2$, a homogeneous mass distribution along the needle is parametrized by $\alpha = \frac{1}{3}$. The configuration space is spanned by the position of the midpoint of the needle, \mathbf{r} , and its orientation angle φ . The conjugated momenta are proportional to the center-of-mass velocity, $\mathbf{v} = \dot{\mathbf{r}}$, and the rotational velocity, $\omega = \dot{\varphi}$. The kinetic energy is conserved, but distributed between two translational and one rotational degrees of freedom. Our fundamental units are the length L , the average velocity $v := \langle \mathbf{v}^2 \rangle^{1/2}$, and the mass m . Then, the only parameter is the reduced density, $n^* := nL^2$.

Kinetics of a single collision

Let \mathbf{v}_i and ω_i be the initial velocities of the needle, and $\Delta \mathbf{r}_j = \mathbf{r} - \mathbf{r}_j$ be the vector pointing from obstacle j to the midpoint of the needle (Fig. 5.1). A coordinate system is introduced via the orientation of the needle (denoted by the unit vector $\hat{\mathbf{e}}_\varphi$) and a perpendicular direction $\hat{\mathbf{e}}_\perp$, where $\hat{\mathbf{e}}_\varphi \times \hat{\mathbf{e}}_\perp = 1$. We make use of a two-dimensional definition of the cross product as $\mathbf{a} \times \mathbf{b} := \det(\mathbf{a}, \mathbf{b})$. The relations $\mathbf{a} \times \hat{\mathbf{e}}_\perp = \mathbf{a} \cdot \hat{\mathbf{e}}_\varphi$ and $\mathbf{a} \cdot \hat{\mathbf{e}}_\perp = -\mathbf{a} \times \hat{\mathbf{e}}_\varphi$ will render useful for eliminating $\hat{\mathbf{e}}_\perp$. Next, we exploit that the momentum transfer occurs perpendicular to the needle, $\Delta \mathbf{p} = \Delta p \hat{\mathbf{e}}_\perp$. The interaction with the obstacle induces a torque on the needle, and the change of angular momentum is given by $-\Delta \mathbf{r}_j \times \Delta \mathbf{p} = a \Delta p$ with $a := -\Delta \mathbf{r}_j \cdot \hat{\mathbf{e}}_\varphi$. Thus, the final velocities read,

$$\mathbf{v}_f = \mathbf{v}_i + \frac{\Delta \mathbf{p}}{m} \quad \text{and} \quad \omega_f = \omega_i + \frac{a \Delta p}{I}. \quad (5.1)$$

Equating the kinetic energy before and after the collision,

$$\frac{(m\mathbf{v}_i)^2}{2m} + \frac{(I\omega_i)^2}{2I} = \frac{1}{2m}(m\mathbf{v}_i + \Delta\mathbf{p})^2 + \frac{1}{2I}(I\omega_i + a\Delta p)^2, \quad (5.2)$$

yields the momentum transfer,

$$\Delta p = 2mI \frac{\mathbf{v}_i \times \hat{\mathbf{e}}_\phi - \omega_i a}{I + ma^2}. \quad (5.3)$$

Note that the final velocities are invariant under the symmetry transformation $\hat{\mathbf{e}}_\phi \mapsto -\hat{\mathbf{e}}_\phi$ (involving $\hat{\mathbf{e}}_\perp \mapsto -\hat{\mathbf{e}}_\perp$).

5.3 Linearized Boltzmann Theory

The Liouville operator

The dynamics of the needle is encoded in the Liouville operator L , in particular, the equation of motion for some dynamic variable A reads,

$$\partial_t A(t) = iLA(t). \quad (5.4)$$

Dynamic correlation functions between two variables A and B describe the response of the system to some perturbation at the time $t_0 = 0$; they are conveniently expressed in terms of the Mori product, $C_{AB}(t) := \langle A(t)|B \rangle$; suppressed time arguments refer to t_0 . The Mori product is a scalar product in the vector space of dynamic variables, or more precisely of their fluctuations (Mori, 1965b). It is defined as, $\langle A|B \rangle := \langle \delta A^* \delta B \rangle$, where $\delta X := X - \langle X \rangle$, and the star denotes the complex conjugate. The Liouville operator is Hermitian with respect to the Mori product, $\langle LA|B \rangle = \langle A|LB \rangle$, as can be seen from its definition by means of a Poisson bracket. Plugging in the formal solution of Eq. (5.4), it follows that

$$C_{AB}(t) = \langle e^{iLt} A|B \rangle = \langle A|e^{-iLt} B \rangle = C_{BA}(-t)^*, \quad (5.5)$$

and in particular, real-valued auto-correlation functions, $C_{AA}(t)$ are invariant under time reversal.

Due to the singular potential of the interaction between the needle and the obstacles, the Liouville operator does, rigorously spoken, not exist. However, pseudo-Liouville operators, L_\pm , can be defined in a similar spirit as for the

hard-sphere interaction (*Ernst et al.*, 1969). Then, the equation of motion changes to

$$\partial_t A(t) = iL_{\pm}A(t) \quad \text{for } t \geq t_0, \quad (5.6)$$

and the operators L_{\pm} are adjoint to each other, $L_{+}^{\dagger} = L_{-}$. The Liouville operator is composed of a free-streaming and a collision part,

$$\begin{aligned} L_{\pm} &= L_{\text{free}} + L_{\text{coll}}^{\pm} \\ &= -i\mathbf{v} \cdot \frac{\partial}{\partial \mathbf{r}} - i\omega \frac{\partial}{\partial \varphi} + i \sum_j T_{\pm}(j); \end{aligned} \quad (5.7)$$

the sum runs over all obstacles. The collision operator $T_{\pm}(j)$ describes a single collision between the needle and obstacle j , it has the form,

$$\begin{aligned} T_{\pm}(j) &= \delta(\Delta \mathbf{r}_j \times \hat{\mathbf{e}}_{\varphi}) \Theta\left(\frac{L}{2} - |\Delta \mathbf{r}_j|\right) \\ &\quad \times \Theta\left(\mp \frac{d}{dt}(\Delta \mathbf{r}_j \times \hat{\mathbf{e}}_{\varphi})\right) \left[\mp \frac{d}{dt}(\Delta \mathbf{r}_j \times \hat{\mathbf{e}}_{\varphi})\right] (b_{\Delta \mathbf{r}_j, \varphi} - 1) \end{aligned} \quad (5.8)$$

$$= \delta(t - t^*) \Theta\left(\mp \frac{d}{dt}(\Delta \mathbf{r}_j \times \hat{\mathbf{e}}_{\varphi})\right) (b_{\Delta \mathbf{r}_j, \varphi} - 1). \quad (5.9)$$

The δ - and Θ -functions encode the (properly normalized) geometric constraints on a collision, they can be rewritten as $\delta(t - t^*)$ where t^* denotes the point in time of the collision. The second Θ -function ensures that the point of contact on the needle actually approaches the obstacle. The last factor contains the operator $b_{\Delta \mathbf{r}_j, \varphi}$ which incorporates the law of collision, Eqs. (5.1) and (5.3); it acts only on the velocities and replaces them by their final values,

$$b_{\Delta \mathbf{r}_j, \varphi} f(\mathbf{v}_i, \omega_i) := f(\mathbf{v}_f, \omega_f). \quad (5.10)$$

The operator $b_{\Delta \mathbf{r}_j, \varphi} - 1$ annihilates expressions that are independent of the velocities.

Densities and currents

A physically important dynamic variable is the tagged particle density; in our case, it describes the probability distribution of the position \mathbf{r} and the orientation φ of the needle. Its Fourier transform is given by

$$\rho_{\nu}(\mathbf{q}) := e^{i\nu\varphi} e^{i\mathbf{q} \cdot \mathbf{r}}. \quad (5.11)$$

Since the particle number (viz. one) is conserved, there are associated current densities, $\mathbf{j}_v^T(\mathbf{q})$ and $j_v^R(\mathbf{q})$, describing the temporal changes of the center-of-mass position and of the orientation of the needle, resp. They satisfy the continuity equation,

$$\partial_t \rho_v(\mathbf{q}) - i \mathbf{q} \cdot \mathbf{j}_v^T(\mathbf{q}) - i v j_v^R(\mathbf{q}) = 0. \quad (5.12)$$

Making use of the equation of motion, Eq. (5.6), and the definition of $\rho_v(\mathbf{q})$, we infer,

$$\mathbf{L}_{\pm} \rho_v(\mathbf{q}) = \mathbf{q} \cdot \mathbf{j}_v^T(\mathbf{q}) + v j_v^R(\mathbf{q}), \quad (5.13)$$

yielding for the longitudinal part of the translational current,

$$j_v^T(\mathbf{q}) := \hat{\mathbf{q}} \cdot \mathbf{j}_v^T(\mathbf{q}) = (\hat{\mathbf{q}} \cdot \mathbf{v}) \rho_v(\mathbf{q}), \quad (5.14)$$

and for the rotational current,

$$j_v^R(\mathbf{q}) = \omega \rho_v(\mathbf{q}); \quad (5.15)$$

$\hat{\mathbf{q}}$ designates the unit vector \mathbf{q}/q .

Static correlations between density and currents are determined by the homogeneity and isotropy of the system. All the $\rho_v(\mathbf{q})$, $j_v^T(\mathbf{q})$, and $j_v^R(\mathbf{q})$ are mutually orthogonal,

$$\langle \rho_\mu(\mathbf{q}) | \rho_\nu(\mathbf{k}) \rangle = \delta_{\mu\nu} \delta_{\mathbf{q}\mathbf{k}}, \quad \langle \rho_\mu(\mathbf{q}) | j_\nu^T(\mathbf{k}) \rangle = \langle \rho_\mu(\mathbf{q}) | j_\nu^R(\mathbf{k}) \rangle = 0. \quad (5.16)$$

The non-vanishing current-current correlations describe the total energy of the needle,

$$\langle j_\mu^T(\mathbf{q}) | j_\nu^T(\mathbf{k}) \rangle = \frac{1}{2} \langle \mathbf{v}^2 \rangle \delta_{\mu\nu} \delta_{\mathbf{q}\mathbf{k}}, \quad (5.17a)$$

$$\langle j_\mu^R(\mathbf{q}) | j_\nu^R(\mathbf{k}) \rangle = \langle \omega^2 \rangle \delta_{\mu\nu} \delta_{\mathbf{q}\mathbf{k}}. \quad (5.17b)$$

For later use, we introduce generalized velocities ω_T and ω_R such that $2\omega_T^2 = \langle \mathbf{v}^2 \rangle$ and $\omega_R^2 = \langle \omega^2 \rangle$.

The incoherent intermediate scattering function

The auto-correlation function of the tagged particle density is called incoherent intermediate scattering function being defined as,

$$\Phi_{\mu\nu}(\mathbf{q}, t) := \langle \rho_\mu(\mathbf{q}, t) | \rho_\nu(\mathbf{q}, 0) \rangle. \quad (5.18)$$

$\Phi_{\mu\nu}(\mathbf{q}, t)$ shares several symmetry properties. For example, it is sufficient to know its values along a single wave number direction, say along the x-axis: Let R_χ be a rotation of the coordinate frame about an angle χ . Thus, we can change the coordinate frame in such a way that the x-axis and \mathbf{q} coincide: $R_\chi \mathbf{q} = q \hat{\mathbf{e}}_x$. As a consequence, the orientation angle φ changes as well, $R_\chi \varphi = \varphi - \chi$. For the correlation function, it follows

$$\begin{aligned} \Phi_{\mu\nu}(\mathbf{q}, t) &= \left\langle e^{-i\mu\varphi(t)} e^{i\nu\varphi(0)} e^{-i(R_\chi^{-1}q\hat{\mathbf{e}}_x) \cdot [\mathbf{r}(t) - \mathbf{r}(0)]} \right\rangle \\ &= \left\langle e^{-i\mu[R_\chi\varphi(t) + \chi]} e^{i\nu[R_\chi\varphi(0) + \chi]} e^{-iq\hat{\mathbf{e}}_x \cdot R_\chi[\mathbf{r}(t) - \mathbf{r}(0)]} \right\rangle \\ &= e^{-i(\mu-\nu)\chi} \Phi_{\mu\nu}(q\hat{\mathbf{e}}_x, t) \end{aligned} \quad (5.19)$$

In the last step, we made use of the rotational invariance of the system after disorder averaging. In particular, if $\Phi_{\mu\nu}(\mathbf{q}, t)$ is diagonal in the helicities μ and ν , it is spherically symmetric in the wave number \mathbf{q} as well.

The formal solution of the equation of motion for the density correlators, Eq. (5.6), can be written as matrix elements of the time evolution operator,

$$\Phi_{\mu\nu}(\mathbf{q}, t) = \langle \rho_\mu(\mathbf{q}) | e^{-iL-t} | \rho_\nu(\mathbf{q}) \rangle. \quad (5.20)$$

It is convenient to Laplace transform the time domain,

$$\mathcal{L}_z[f] := i \int_0^\infty e^{izt} f(t) dt \quad \text{for } \text{Im } z > 0, \quad (5.21)$$

which converts Eq. (5.20) into matrix elements of the resolvent of the Liouville operator,

$$\Phi_{\mu\nu}(\mathbf{q}, z) = \left\langle \rho_\mu(\mathbf{q}) \left| \frac{1}{L_- - z} \right| \rho_\nu(\mathbf{q}) \right\rangle. \quad (5.22)$$

By means of the Mori-Zwanzig projection technique (Mori, 1965a; Zwanzig, 1961, 1965), an equation of motion is derived which relates the time evolution of the density correlations, $\Phi_{\mu\nu}(\mathbf{q}, t)$, with the current correlation functions, $K_{\mu\nu}^{\alpha\beta}(t)$, to be introduced later. We consider the densities $\rho_\nu(\mathbf{q})$ as slow variables and start by defining a projector onto their subspace,

$$P := \sum_\nu | \rho_\nu(\mathbf{q}) \rangle \langle \rho_\nu(\mathbf{q}) |, \quad (5.23)$$

and its orthogonal complement $Q := 1 - P$. Exploiting the operator identity,

$$\frac{z}{L_- - z} = \frac{z}{L_- Q - z} - \left(L_- Q \frac{1}{QL_- Q - z} QL_- - L_- \right) P \frac{1}{L_- - z}, \quad (5.24)$$

yields,

$$z\Phi_{\mu\nu}(\mathbf{q}, z) = -\delta_{\mu\nu} + \sum_{\sigma} \langle \rho_{\mu}(\mathbf{q}) | L_{-} | \rho_{\sigma}(\mathbf{q}) \rangle \Phi_{\sigma\nu}(\mathbf{q}, z) \\ - \sum_{\sigma} \langle Q_{L_{+}\rho_{\mu}}(\mathbf{q}) | \frac{1}{QL_{-}Q - z} | Q_{L_{-}\rho_{\sigma}}(\mathbf{q}) \rangle \Phi_{\sigma\nu}(\mathbf{q}, z). \quad (5.25)$$

Utilizing Eq. (5.13), the matrix elements $\langle \rho_{\mu}(\mathbf{q}) | L_{-} | \rho_{\sigma}(\mathbf{q}) \rangle$ vanish, and we see that the matrix elements in the second line describe current-current correlations,

$$K_{\mu\nu}^{\alpha\beta}(\mathbf{q}, z) := \frac{1}{\omega_{\alpha}\omega_{\beta}} \langle j_{\mu}^{\alpha}(\mathbf{q}) | \frac{1}{QL_{-}Q - z} | j_{\nu}^{\beta}(\mathbf{q}) \rangle, \quad (5.26)$$

where $\alpha, \beta \in \{T, R\}$ denote either translational or rotational parts. Note that the dynamics of these correlations is driven by a reduced Liouville operator, $QL_{\pm}Q$, which has been decoupled from the slow variables, i. e., the density modes. Introducing the frequencies $\Omega_v^T(\mathbf{q}) := q\omega_T$ and $\Omega_v^R(\mathbf{q}) := v\omega_R$ and going back to the time domain, we obtain a set of integro-differential equations relating density and current correlations,

$$\partial_t \Phi_{\mu\nu}(\mathbf{q}, t) + \sum_{\substack{\sigma \\ \alpha\beta}} \int_0^t d\tau \Omega_{\mu}^{\alpha}(\mathbf{q}) K_{\mu\sigma}^{\alpha\beta}(\mathbf{q}, \tau) \Omega_{\sigma}^{\beta}(\mathbf{q}) \Phi_{\sigma\nu}(\mathbf{q}, t - \tau) = 0, \quad (5.27)$$

with initial conditions $\Phi_{\mu\nu}(\mathbf{q}, 0) = \delta_{\mu\nu}$. This equation has the general form of a time evolution equation allowing for memory effects if the kernels $K_{\mu\nu}^{\alpha\beta}(\mathbf{q}, t)$ are non-local in time.

The correlators $K_{\mu\nu}^{\alpha\beta}(\mathbf{q}, t)$ can be interpreted as modified velocity auto-correlation functions. In the hydrodynamic limit, i. e., for small wavenumbers and large time scales, it holds, e. g.,

$$K_{\mu\nu}^{TT}(q \rightarrow 0, t \rightarrow \infty) = \frac{1}{\langle v^2 \rangle} \langle \mathbf{v}(t) \cdot \mathbf{v}(0) \rangle; \quad (5.28)$$

in particular, the dynamics in this limit is driven by the full Liouville operator, L_{\pm} (Boon and Yip, 1991).

Boltzmann approximation

Until here, the derivation was rigorous and applies at all obstacle densities. But in order to obtain a closed set of equations for the density and current

correlators, it is inevitable to introduce approximations. We will make the simplest choice and ignore correlated collisions in the spirit of Boltzmann's Stoßzahlansatz.

An equation of motion for the current correlators similar to Eq. (5.25) is obtained by repeating the above procedure with a projector onto the currents,

$$\tilde{\mathbb{P}} := \sum_{\alpha, \nu} |j_\nu^\alpha(\mathbf{q})\rangle \frac{1}{\omega_\alpha^2} \langle j_\nu^\alpha(\mathbf{q})|, \quad (5.29)$$

and its complement, $\tilde{\mathbb{Q}} = 1 - \tilde{\mathbb{P}}$. An operator identity analogous to Eq. (5.24) holds, and we approximate,

$$z K_{\mu\nu}^{\alpha\beta}(\mathbf{q}, z) \approx -\delta_{\mu\nu} \delta^{\alpha\beta} + \sum_{\gamma, \sigma} \frac{1}{\omega_\alpha \omega_\gamma} \langle j_\mu^\alpha(\mathbf{q}) | \mathbb{L}_- | j_\sigma^\gamma(\mathbf{q}) \rangle K_{\sigma\nu}^{\gamma\beta}(\mathbf{q}, z). \quad (5.30)$$

Here, matrix elements of the generalized forces, $\tilde{\mathbb{Q}} \mathbb{L}_\pm j_\nu^\alpha(\mathbf{q})$, have been neglected. They describe higher order collision terms and are responsible for memory effects. This approximation is good as long as the collision events are rare and uncorrelated, i. e., in the dilute limit.

We are left with the evaluation of the matrix elements of the Liouville operator in the subspace of currents. Due to time inversion symmetry, current-current matrix elements of the *free* Liouville operator vanish,

$$\langle j_\mu^\alpha(\mathbf{q}) | \mathbb{L}_{\text{free}} | j_\nu^\beta(\mathbf{q}) \rangle = 0, \quad (5.31)$$

and the remaining task is the calculation of matrix elements of the collision operator,

$$\langle j_\mu^\alpha(\mathbf{q}) | \mathbb{L}_- | j_\nu^\beta(\mathbf{q}) \rangle = iN \langle j_\mu^\alpha(\mathbf{q}) | \mathbb{T}_-(1) | j_\nu^\beta(\mathbf{q}) \rangle \quad (5.32)$$

Since $\mathbb{T}_\pm(1)$ does not act on the space variables, \mathbf{r} and φ , the matrix elements vanish for $\mu \neq \nu$, and they are independent of \mathbf{q} and μ . Further, $\mathbb{T}_\pm(1)$ and the angular velocity ω are invariant under rotation of the reference frame whereas the velocity vector \mathbf{v} is not. Thus, mixed matrix elements, $\alpha \neq \beta$, vanish as well, and we are left with two microscopic frequencies,

$$v_T := -\frac{N}{2\omega_T^2} \langle \mathbf{v} \cdot \mathbb{T}_-(1) \mathbf{v} \rangle, \quad (5.33a)$$

$$v_R := -\frac{N}{\omega_R^2} \langle \omega \mathbb{T}_-(1) \omega \rangle. \quad (5.33b)$$

The calculation is tedious and deferred to Appendix A; we find,

$$v_T = \frac{3}{8} \sqrt{3\alpha} \operatorname{Arsinh}(\alpha^{-1/2}) \frac{n^* \omega_T}{L}, \quad (5.34a)$$

$$v_R = \frac{3}{16} \sqrt{3} \left[\sqrt{1+\alpha} - \alpha \operatorname{Arsinh}(\alpha^{-1/2}) \right] n^* \omega_R, \quad (5.34b)$$

which reduces to a homogeneous mass distribution along the needle, i. e., for $\alpha = \frac{1}{3}$, to

$$v_T \approx 0.49359 \frac{n^* \omega_T}{L} \quad \text{and} \quad v_R \approx 0.23244 n^* \omega_R. \quad (5.35)$$

Our approximation for the current correlators, Eq. (5.30), collapses and is simply given by

$$K_{\mu\nu}^{\alpha\beta}(\mathbf{q}, z) = \frac{-\delta_{\mu\nu} \delta_{\alpha\beta}}{z + i\nu_\alpha}. \quad (5.36)$$

Hence, there are only two non-vanishing current correlators; in time domain they have the form

$$K^\alpha(t) = \exp(-\nu_\alpha t) \quad \text{for} \quad \alpha \in \{T, R\}. \quad (5.37)$$

Using that both functions decay exponentially with rates independent of q and μ, ν , it can be shown that the diffusion coefficients of center-of-mass motion and of rotation follow from the relations,

$$D_{\text{cm}} = \frac{v^2}{2} \int_0^\infty K^T(t) dt = \frac{v^2}{2\nu_T}, \quad (5.38a)$$

$$D_{\text{rot}} = \omega^2 \int_0^\infty K^R(t) dt = \frac{\omega^2}{\nu_R}. \quad (5.38b)$$

Since the frequencies obey $\nu_T, \nu_R \sim n^*$, the diffusion coefficients are linearly suppressed with increasing density.

6 Entanglement and Enhanced Diffusion

Abstract

The modified Lorentz model introduced in Chapter 5 is investigated by means of extensive Molecular Dynamics simulations. A novel algorithm for the collision detection makes an exploration of the full density range feasible. Our results for the rotational diffusion coefficient provide a thorough verification of the predictions of the tube model for highly entangled networks of rigid rods. A surprising and novel finding is the enhancement of center-of-mass diffusion with increasing density due to the confinement of the needle in tubes.

In the previous chapter, we have presented a solution of the dynamic problem of a needle in a random environment in the spirit of the linearized Boltzmann theory. Having neglected correlations between subsequent collisions, the result will be applicable in dilute situations where the density of the obstacles is low and collisions are rare. Molecular Dynamics simulations are a useful tool for investigating the more interesting case of a dense obstacle environment.

6.1 Molecular Dynamics Simulations

We have extended our algorithm from Section 4.2 in order to incorporate the additional features and peculiarities of a needle. First, the phase space spans not only the center-of-mass position and velocity, but also the orientation angle of the needle and its angular velocity. But the major change is in the calculation of the trajectory involving sophisticated collision tests and modified velocity updates after a collision according to Eqs. (5.1) and (5.3).

The aim of the collision tests is the determination of the point in time of the next collision event between the needle and one of the obstacles. All obstacles in the neighborhood of the needle are tested individually, finally, the very next

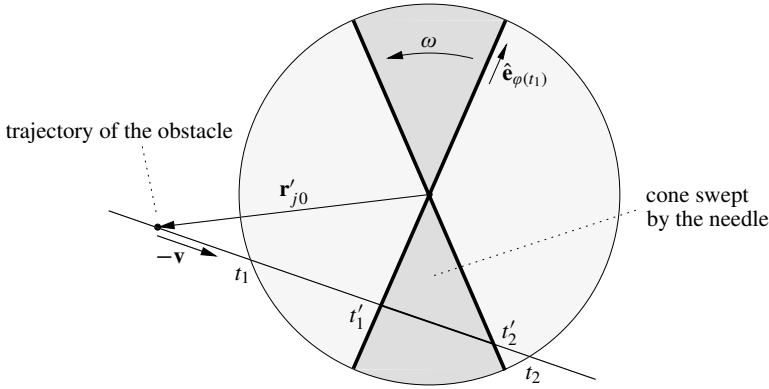


Figure 6.1 Geometry in the center-of-mass system of the needle for the first two stages of the collision test.

event is chosen. Once a collision has been detected after a time t_{coll} , the subsequent tests can be reduced to the time interval $T = (0, t_{\text{coll}})$. Initially, t_{coll} is limited by the time which the needle would need in order to cross its associated obstacle cell (see Section 4.2). The actual tests consist of three stages and are described best in the center-of-mass system of the needle, see Fig. 6.1. There, the needle is fixed in space, but rotates about its center, and the obstacle moves with velocity $-\mathbf{v}$; its initial position is given by $\mathbf{r}'_{j0} = \mathbf{r}_j - \mathbf{r}_0$.

Stage 1

The needle is always contained in a disk of radius $L/2$ about its midpoint, $\mathbf{r}' = 0$. A collision can only take place if the obstacle crosses this disk, i. e., in the time interval $T_1 = (t_1, t_2)$ delimited by

$$T_1 = \left(-\frac{b}{v^2} - \frac{\sqrt{q}}{v^2}, -\frac{b}{v^2} + \frac{\sqrt{q}}{v^2} \right) \quad (6.1)$$

with the short-cuts, $b = \mathbf{v} \cdot \mathbf{r}$ and $q = b^2 - v^2 [r^2 - (L/2)^2]$. If the discriminant q becomes negative, the particle misses, there won't be any collision at all, and the test stops. Otherwise, the interval of interest for the next stage is given by the intersection of the two preceding intervals, replacing $T \leftarrow T \cap T_1$. By doing so, we automatically satisfy the length constraint of the needle which can be dropped in the following stages.

Stage 2

During the time interval T , the needle doesn't actually cover the whole disk but only a small segment. Its intersection with the trajectory of the obstacle yields sharper bounds on a possible collision. In particular, a significant number of obstacles can be rejected here since they miss the segment completely. The trajectory of the obstacle is described by the point set, $\{\mathbf{x} \mid \mathbf{x} \times \mathbf{v} = \mathbf{r}'_{j0} \times \mathbf{v}\}$. Let the needle be oriented along the direction $\hat{\mathbf{e}}_\varphi$, then, it contains all points of the disk with $\mathbf{x} \times \hat{\mathbf{e}}_\varphi = 0$. The intersection of both straight lines yields the point,

$$\mathbf{x} = \frac{\mathbf{v} \times \mathbf{r}'_{j0}}{\mathbf{v} \times \hat{\mathbf{e}}_\varphi} \hat{\mathbf{e}}_\varphi. \quad (6.2)$$

It is reached by the obstacle at time t when $\mathbf{x} = \mathbf{r}'_{j0} - \mathbf{v}t$. Scalar multiplication with \mathbf{v} solves for t ,

$$t = \frac{1}{v^2} \left[\mathbf{v} \cdot \mathbf{r}'_{j0} - \frac{\mathbf{v} \times \mathbf{r}'_{j0}}{\mathbf{v} \times \hat{\mathbf{e}}_\varphi} (\mathbf{v} \cdot \hat{\mathbf{e}}_\varphi) \right]. \quad (6.3)$$

This expression can be simplified by introducing polar coordinates for the velocity, $\mathbf{v} = v\hat{\mathbf{e}}_\psi$. Then, it holds for the ratio,

$$\frac{\mathbf{v} \cdot \hat{\mathbf{e}}_\varphi}{\mathbf{v} \times \hat{\mathbf{e}}_\varphi} = \frac{1}{\tan(\varphi - \psi)}. \quad (6.4)$$

Next, we need to find the interval $T_2 = (t'_1, t'_2)$ of times when the obstacle traverses the segment covered by the needle. The boundaries are obtained by evaluating Eq. (6.3) for $\varphi = \varphi_0 + \omega t_{1/2}$ with the initial orientation φ_0 . However, if the point t_1 already belongs to the segment, it is guaranteed that no collision will take place in the interval T_2 , and actually, its complement yields the desired restriction. This issue and the question of splitting the interval into two is elegantly solved in terms of interval arithmetics. Since it is at the heart of the algorithm of stage 3, we will make use of it here as well; Appendix B gives a short introduction to this topic, more details can be found in the book by Hansen and Walster (2004). All we have to do is to replace the real number φ in Eq. (6.3) by the interval of possible orientations, $\Phi = \varphi_0 + \omega T$, and evaluate the obtained expression according to the rules of interval arithmetics,¹

$$T_2 = \frac{1}{v^2} \left[\mathbf{v} \cdot \mathbf{r}'_{j0} - \frac{1}{\tan(\Phi - \psi)} (\mathbf{v} \times \mathbf{r}'_{j0}) \right]. \quad (6.5)$$

¹Note that the obtained interval is tight, there is no dependence problem here since Φ enters the expression only once, and the tangent function is monotonic.

Strictly speaking, T_2 is a generalized interval, a so-called containment set or simply a union of disjoint intervals. Finally, this result is applied to the interval T by replacing $T \leftarrow T \cap T_2$.

Stage 3

While the foregoing stages merely yield bounds on a possible collision, the actual collision point t^* will be calculated in this last stage. The (oriented) distance between the obstacle and the needle is given by,

$$d(t) = \mathbf{r}'_j(t) \times \hat{\mathbf{e}}_{\varphi(t)} = (\mathbf{r}'_{j0} - \mathbf{v}t) \times \hat{\mathbf{e}}_{\varphi_0 + \omega t}. \quad (6.6)$$

The orientation angle φ is measured from the x-axis, and we have

$$\hat{\mathbf{e}}_{\varphi} = \begin{pmatrix} \cos(\varphi) \\ \sin(\varphi) \end{pmatrix}. \quad (6.7)$$

If $t \in T$, the vanishing of the distance, $d(t^*) = 0$, is the necessary and sufficient condition for a collision since the finite length of the needle is already accounted for in the reduction of T in stage 1. Finding the zeros of the transcendent function $d(t)$ in the interval T is a considerably difficult task. *A priori*, it is not known how many zeros exist or whether there is no zero at all. However, all usual numerical methods require some knowledge about the zero in advance. If a simple zero is bracketed, iterating some algorithm can make the brackets tight—but if we don't have the initial bracket, we're lost. A wonderful solution out of this dilemma is pointed out by interval analysis: we calculate the zeros by means of the interval version of the Newton algorithm which is superior to the usual Newton algorithm with respect to the following points:

- without any *a priori* knowledge, the algorithm separates all zeros and bounds them correctly
- only little requirements are posed on the function under consideration: it must be continuous and be given by an algebraic expression
- the non-existence of a zero is rapidly proven

Further, since for simple zeros the convergence of the algorithm is as fast as with the usual Newton algorithm, the interval Newton method is the algorithm of choice for our problem of collision detection (*Hansen and Walster, 2004*); it is described in Appendix B. In particular, the algorithm avoids any sampling

of the search interval being the bottle neck of other Molecular Dynamics approaches to thin needles (Frenkel and Maguire, 1983; Huthmann *et al.*, 1999; de la Pena *et al.*, 2006). In an efficient and robust way, the algorithm tells us if the needle hits the obstacle at all and at which time t^* this next collision will take place. If this is the case, it is checked whether the next so far known collision with a different obstacle at t_{coll} is later than the just found one, and we update $t_{\text{coll}} \leftarrow \min\{t^*, t_{\text{coll}}\}$.

6.2 Diffusion Coefficients

The simplest quantities characterizing the long-time dynamics of the needle are the diffusion coefficients D_{cm} and D_{rot} of the center of mass and of the orientation of the needle, resp. They are measured from the long-time limits of the mean-square displacements,

$$D_{\text{cm}} = \lim_{t \rightarrow \infty} \frac{\delta r^2(t)}{4t} \quad \text{and} \quad D_{\text{rot}} = \lim_{t \rightarrow \infty} \frac{\delta \varphi^2(t)}{2t}, \quad (6.8)$$

with the mean-square center-of-mass and mean-square angular displacements being defined as

$$\delta r^2(t) := \langle |\mathbf{r}(t) - \mathbf{r}(0)|^2 \rangle, \quad (6.9a)$$

$$\delta \varphi^2(t) := \langle |\varphi(t) - \varphi(0)|^2 \rangle. \quad (6.9b)$$

At low densities, the diffusive motion is caused by uncorrelated collisions with the obstacles, and the Boltzmann result from Section 5.3 applies, $D_{\text{cm}}, D_{\text{rot}} \sim 1/n^*$, see Eqs. (5.35) and (5.38).

An intrinsic length scale of the medium is the average mesh size,

$$\xi_{\text{m}} \approx \frac{1}{\sqrt{n}}. \quad (6.10)$$

Once the length of the needle and the mesh size become comparable, $L \approx \xi_{\text{m}}$ or $n^* \approx 1$, the collisions become correlated. Then, the free rotation of the needle is hindered, and diffusion is suppressed, $D_{\text{rot}} < D_{\text{rot}}^{(0)}$. This cross-over can clearly be seen in the results of our simulation (Fig. 6.2): after following the Boltzmann result, the rotational diffusion is additionally suppressed with increasing density. Our data corroborate an asymptotic power law,

$$D_{\text{rot}} \sim (n^*)^{-2}, \quad (6.11)$$

for very high densities, i. e., for $n^* \gtrsim 10^2$ or $L/\xi_m \gtrsim 10$. Over the complete simulated range of densities, the rotational diffusion coefficient spans more than eight decades, and we observe this power law over three decades.

This asymptotic suppression can be explained in terms of the tube model by Doi and Edwards (*Doi and Edwards*, 1978, 1986). In this model, the needle is thought to be confined in a tube of diameter d and length L . The diameter is estimated from the requirement to have no obstacles in the tube, $nLd \approx 1$, as

$$d \approx \frac{1}{nL}. \quad (6.12)$$

Inside the tube, the motion of the needle is basically restricted to translation along its axis. After travelling half its length, the needle is found in a new tube which is on average tilted against the old one by an angle, $\varepsilon \approx d/L$. The change of the orientation occurs at any one time the needle has left its tube to either direction. The time to disengage from a tube, τ_d , is estimated from the mean-square displacement, $\delta r^2(\tau_d) \approx (L/2)^2$; anticipating that the translational motion is still ballistic at the time scale τ_d , we find $\tau_d \approx L/v$. Altogether, the orientation performs a random walk with step size ε and hopping rate $1/\tau_d$ yielding a mean-square angular displacement, $\delta\varphi^2(t) = \varepsilon^2 t/\tau_d$, and an estimate of the rotational diffusion coefficient,

$$D_{\text{rot}}^{\text{tube}} \approx \frac{(d/L)^2}{L/v} \approx \frac{v}{n^2 L^5}. \quad (6.13)$$

While the rotational diffusion is suppressed with increasing obstacle density, the translational diffusion, D_{cm} , has a minimum near $n^* \approx 1$ and increases again, see Fig. 6.2. Within the density range covered by our simulations, D_{cm} is enhanced by two orders of magnitude compared to its minimum value. Our data indicate a power-law divergence,

$$D_{\text{cm}} \sim (n^*)^\zeta \quad \text{for } n^* \rightarrow \infty, \quad (6.14)$$

and are compatible with an exponent $\zeta = 0.8$.

It is a surprising and at the first glance counter-intuitive observation that the system becomes *faster* in the presence of more obstacles! The overall picture up to here was that the motion of the needle is hindered due to collisions, leading to diffusion in general and to a decreasing diffusion coefficient—this is a direct result of the linearized Boltzmann theory. The tube model also tells us that the rotational diffusion is even stronger suppressed at high densities where

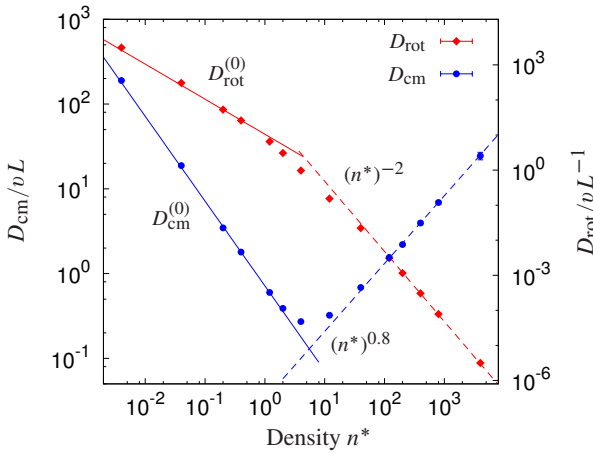


Figure 6.2 Simulation results for the diffusion coefficients of the needle. Blue dots refer to the center-of-mass diffusion D_{cm} ; red diamonds to rotational diffusion D_{rot} . Solid lines show the result from the linearized Boltzmann theory (Chapter 5). Dashed lines are fits to the asymptotic high-density behavior.

The Legend of the Ulm Sparrow

Once upon a time, the continuing construction of the Ulmer Münster towers made it necessary to haul big pieces of lumber through the narrow gates of the city. It is a famous tale that once a teamster and his lorry were prevented from entering the city by logs which lay crosswise on the cart but were wider than the gate. The first reaction of the stupefied citizens was to enlarge or tear down the gate. Fortunately, this desperate measure was made unnecessary when the people observed a sparrow with a straw in his beak trying to fly through the narrow entrance of his nest. While passing the slit he rotated the straw to line it up with his path. Since then the sparrow has become a symbol of Ulm and till today he rests on the roof top of the Ulmer Münster.




Figure 6.3 The legend of the Ulm sparrow illustrates the facilitation of longitudinal motion in the presence of a dense obstacle environment.

the Boltzmann approximation is no longer valid. However, for the center-of-mass diffusion things are upside down. The motion is sped up in the presence of a dense obstacle environment. Instead of hindering the needle, the obstacles guide the needle to follow its own orientation and, thus, Brownian motion is avoided. At one hand side, the needle is confined by the obstacles; on the other hand, this confinement facilitates translational motion. This paradox is nicely illustrated by the legend of the Ulm Sparrow, see Fig. 6.3.

6.3 A Twofold Persistence

The previous discussion of the diffusion coefficients has shown that the dynamics of a long needle in a dense environment, $L \gg \zeta_m$, is far beyond the description in terms of single collisions. Strong collective effects arise and dominate the physics. They lead to a persistence of both the translational motion and the orientation and introduce new macroscopic time scales.

Persistence of orientation

While the ideas of the tube model are quite intuitive, it is important to test this picture in detail against the results of the simulation. The confinement of the needle is directly observed in the mean-square angular displacement, $\delta\varphi^2(t)$: with increasing density, it develops an intermediate plateau, see Fig. 6.4. In a certain time window, the needle can't relax its initial orientation. The plateau begins at the microscopic time scale of the collisions, $\tau_{\text{coll}} \sim 1/n^*$; its value is denoted by ε^2 . Since the rotation of the needle is restricted to the angle $\varepsilon = d/L$, it measures directly the width d of the tube. The ballistic motion at short times implies $\delta\varphi^2(\tau_{\text{coll}}) \sim \tau_{\text{coll}}^2 \sim (n^*)^{-2}$, and the tube width vanishes as $1/nL$ with a prefactor of order 1—we measure (inset of Fig. 6.4)

$$\varepsilon \approx \frac{1.41}{n(L/2)^2}, \quad \text{and hence,} \quad d = \varepsilon L \approx \frac{5.66}{nL}. \quad (6.15)$$

The end of the plateau defines the disengagement time τ_d , i. e., the time the needle takes to leave its tube. As indicated by our data, this time is of the order L/v and does not depend on the density. Beyond the plateau, the mean-square angular displacement increases linearly, reflecting normal diffusion. The disengagement time is defined by matching the plateau with the extrapolation of the diffusive regime,

$$\varepsilon^2 = 2D_{\text{rot}}\tau_d, \quad (6.16)$$

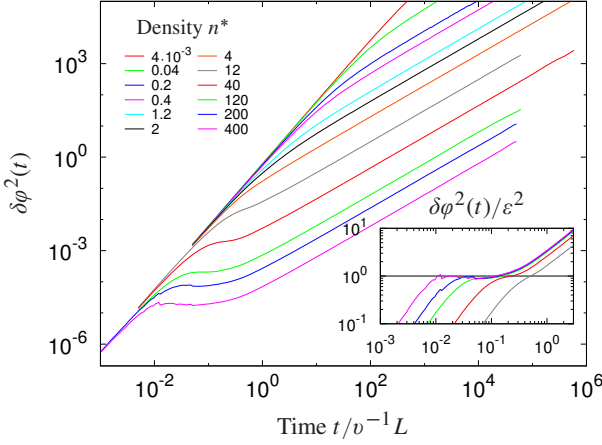


Figure 6.4 Mean-square angular displacement $\delta\varphi^2(t)$ over a wide range of obstacle densities n^* . At high densities, an intermediate plateau develops between the ballistic and the diffusive regime, i. e., for $\tau_{\text{coll}} \ll t \ll \tau_d$. Inset: Plotting $\delta\varphi^2(t)/\varepsilon^2$ against t demonstrates that the plateau value is given by ε^2 as defined in Eq. (6.15), and that the disengagement time τ_d does not depend on the density.

plugging in our result for ε , Eq. (6.15),

$$D_{\text{rot}} \approx \frac{1.0}{\tau_d n^2 (L/2)^4}. \quad (6.17)$$

A fit to our data yields the prefactor for the diffusion coefficient,

$$D_{\text{rot}} \approx 1.5 \frac{v}{n^2 (L/2)^5}, \quad (6.18)$$

and hence, for the disengagement time,

$$\tau_d \approx 0.3L/v. \quad (6.19)$$

Anticipating the results for translational motion, we find that this value for τ_d is related to a translation along the tube over a distance $0.4L$, which fits well with the expected $L/2$.

We have seen that the mean-square angular displacement, $\delta\varphi^2(t)$, is well described in terms of the tube model. Next, we turn to the question how fast

the orientation of the needle relaxes. This relaxation becomes slow due to the confinement of the needle in a narrow channel. The orientation exhibits some persistence, which is measured by the orientation correlation function

$$\Psi_1(t) := \langle \hat{\mathbf{e}}_{\varphi(t)} \cdot \hat{\mathbf{e}}_{\varphi(0)} \rangle; \quad (6.20)$$

it is related to the intermediate scattering function $\Phi_{\mu\nu}(q, t)$ from Chapter 5 in the limit $q \rightarrow 0$ and $\mu = \nu$,

$$\Psi_{\mu}(t) := \langle \cos(\mu \Delta\varphi(t)) \rangle \equiv \Phi_{\mu\mu}(0, t). \quad (6.21)$$

An analogous quantity is known from polymer physics: the tangent-tangent correlation function along the back bone of the polymer. Here, thermal fluctuations change the orientation of the tangent vector and compete with the bending stiffness. In the dynamical quantity $\Psi_1(t)$, the interplay of random collisions with the environment, confinement and inertia leads to the decorrelation of the orientation.

At high densities, $n^* \gg 1$, the orientation relaxation is well approximated by an exponential (Fig. 6.5),

$$\Psi_1(t) \simeq \exp(-t/\tau_{\text{rot}}). \quad (6.22)$$

Therewith, a new time scale, τ_{rot} , is introduced quantifying the persistence of the orientation of the needle. Expanding the cosine for small angles,

$$\langle \cos(\Delta\varphi(t)) \rangle = 1 - \frac{1}{2}\delta\varphi^2(t) + O[\delta\varphi^4(t)], \quad (6.23)$$

the connection to the mean-square angular displacement, $\delta\varphi^2(t)$, is established. Thus, the confinement in the tube is also reflected in a plateau in the orientation correlator, $\Psi_1(t)$, at $1 - \frac{1}{2}\varepsilon^2$. This plateau is made visible in our data by plotting the deviation of $\Psi_1(t)$ from 1, see Fig. 6.6. Note that the plateau is limited to times smaller than the disengagement time, $t \ll \tau_d$, and thus, doesn't extend to longer times with increasing density. In sequel to the plateau, a linear relaxation follows being identified with the short-time expansion of the exponential, Eq. (6.22), i. e., for times $t \ll \tau_{\text{rot}}$. At the same time, it can be matched with the diffusive regime in the mean-square angular displacement, and we obtain the connection between the persistence of orientation and the rotational diffusion coefficient,

$$\tau_{\text{rot}} = \frac{1}{D_{\text{rot}}} \sim n^2 L^5 \quad (6.24)$$

With increasing obstacle density or increasing length of the needle, the rotational relaxation time, τ_{rot} , diverges rapidly.

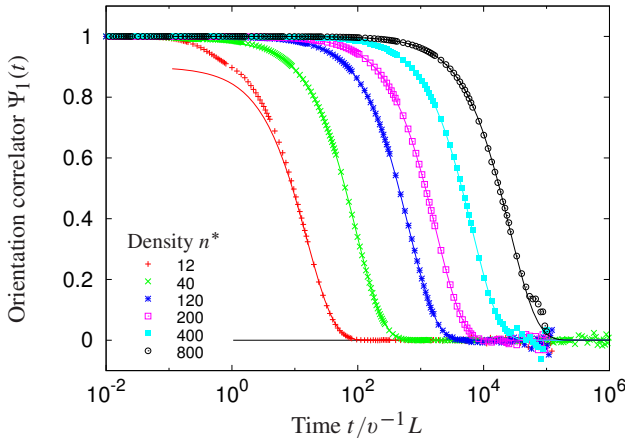


Figure 6.5 In dense environments, i.e., for large n^* , the orientation of the needle relaxes exponentially setting the time scale τ_{rot} . Symbols show simulation data, lines represent exponential fits to long times.

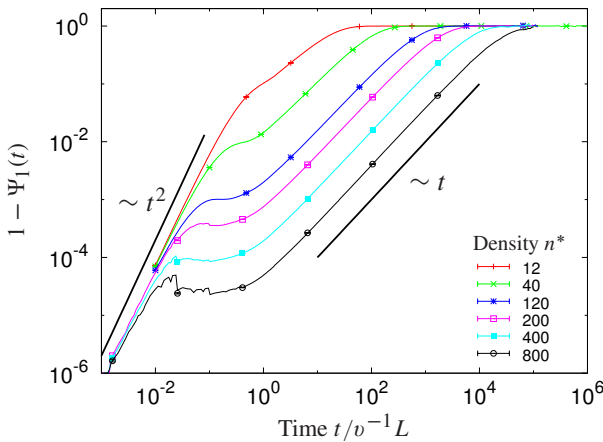


Figure 6.6 A double-logarithmic plot of the initial decay of the orientation correlations, $1 - \Psi_1(t)$, resembles the mean-square angular displacement, $\delta\varphi^2(t)$, cf. Fig. 6.4

Persistence of translation

More insight into the influence of the tube on the translational motion of the needle is gained by looking at the mean-square displacement of the center of mass, $\delta r^2(t)$. Its equation of motion follows from Eq. (5.27),

$$\partial_t \delta r^2(t) = 2v^2 \int_0^t d\tau \psi_{\text{cm}}(\tau), \quad (6.25)$$

observing that

$$\delta r^2(t) = -2 \frac{\partial^2}{\partial q^2} \Phi_{\mu\nu}(\mathbf{q}, t) \Big|_{\substack{\mu=\nu=0 \\ q \rightarrow 0}}. \quad (6.26)$$

Recall that according to the Boltzmann approximation, the velocity auto-correlation function, $\psi_{\text{cm}}(t)$, decays exponentially in the dilute limit, Eq. (5.37). Plugging in this result yields a cross-over in the mean-square displacement near $t \approx \nu_{\text{cm}}^{-1}$ from ballistic motion, $\delta r^2(t) \simeq v^2 t^2$, for short times to diffusion, $\delta r^2(t) \simeq 4D_{\text{cm}}^{(0)} t$, for long times. Deviations from this behavior are inspected in Fig. 6.7 by plotting the ratio $\delta r^2(t)/4D_{\text{cm}}^{(0)} t$ against the average number of collisions, t/τ_{coll} . The collision rate is proportional to ν_{cm} , we have measured,

$$\tau_{\text{coll}}^{-1} \approx 0.845 nLv. \quad (6.27)$$

The data for the six lowest simulated densities completely collapse over the whole time window demonstrating that the Boltzmann approximation works very well at low obstacle densities, $n^* \lesssim 1$. At large densities, however, the ballistic regime is considerably extended and covers many hundred collisions, shifting the long-time limit—and therewith the diffusion coefficient D_{cm} —to higher values. Note that the cross-over near $t \approx \nu_{\text{cm}}^{-1}$ is still present even if it is hardly distinguished by eye. But the underlying mechanisms are completely different: at short times, motion is ballistic due to the *absence* of obstacles, whereas at intermediate times, motion is ballistic in spite of the *presence* of obstacles. This intermediate ballistic regime reflects a persistence of the translational motion, which is connected with the emergence of another divergent time scale.

The cross-over between the two ballistic regimes is seen much clearer by directly looking at the velocity auto-correlation function, $\psi_{\text{cm}}(t)$. While the Boltzmann result is reproduced at low densities, the exponential decay stops near the value $\frac{1}{2}$ for large densities, $n^* \gg 1$, and a shoulder or intermediate plateau develops (Fig. 6.8). The end of this plateau is associated with the end

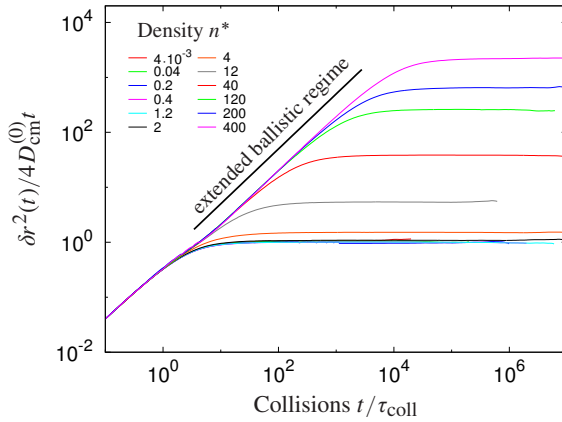


Figure 6.7 The scaling plot of the mean-square displacement, $\delta r^2(t)$, tests the validity of the Boltzmann approximation. The data for the six lowest densities, $n^* < 1$, collapse. Further, the plot proves the emergence of an extended ballistic regime covering several hundred collisions at high densities.

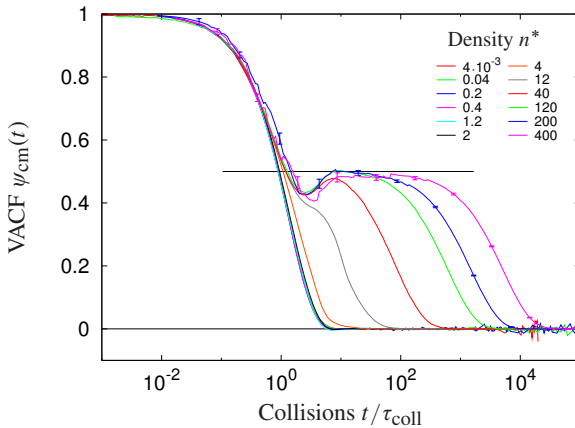


Figure 6.8 Velocity auto-correlation functions plotted against the number of collisions. Whereas the six lowest densities, $n^* < 1$, collapse again on the Boltzmann result, an intermediate plateau develops with increasing density leading to a second exponential relaxation with the time scale τ_{turn} . The black line indicates the plateau value $\frac{1}{2}$.

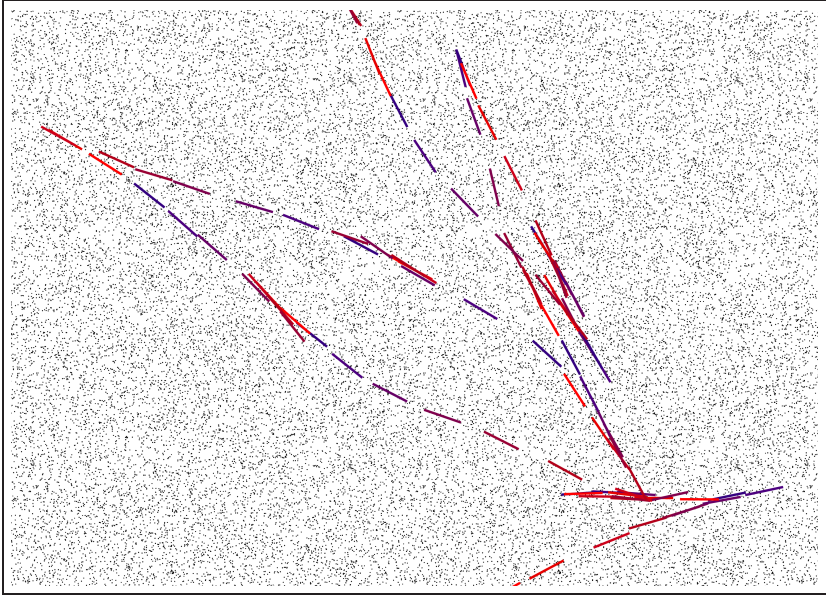


Figure 6.9 Snapshots of the needle in a single realization of point obstacles at $n^* = 120$. The time interval between subsequent exposures, $\Delta t = 1.8 L/v$, covers about one hundred collisions. Time flows from red needles to blue ones, starting with red again. Note the long straight trajectories and the cuspid turning-back points. The figure corroborates the picture of the tube model: the needle is confined in a narrow channel where translation—though being restricted to one dimension—is nearly unobstructed by collisions.

of the extended ballistic regime, and a second relaxation follows. The value of the plateau being at the half height of the initial correlation, can be explained by a reduction of the translational degrees of freedom from two to one, i. e., by the confinement of the needle into a narrow channel.

Up to here, we have explained the emergence of the extended ballistic regime by the confinement of the needle between the obstacles. But what mechanism limits this regime? The snapshots of the needle in Fig. 6.9 show that the trajectories are mainly composed of long, slightly bend segments. This straight motion is interrupted by situations where the needle rests for a short while until it either continues its way or completely turns back. It seems that such turning-back events occur spontaneously and cause the needle to run back

in the same channel it came from. The orientation of the needle is merely changed during such events yielding cusps in the trajectory.

For the further analysis, we split up the center-of-mass velocity in components longitudinal and transverse to the current axis of the needle,

$$v_{\parallel}(t) := \mathbf{v} \cdot \hat{\mathbf{e}}_{\varphi(t)} \quad \text{and} \quad v_{\perp}(t) := -\mathbf{v} \times \hat{\mathbf{e}}_{\varphi(t)}. \quad (6.28)$$

The time series of both components differ strongly for a given realization, see Fig. 6.10. While the transverse velocity, $v_{\perp}(t)$, fluctuates fast, the longitudinal velocity, $v_{\parallel}(t)$, varies slowly. On long time scales, both components explore the whole range $(-v_{\max}, v_{\max})$; the maximum value is attained when all kinetic energy is in a single degree of freedom; hence, $v_{\max}^2 = \frac{3}{2}v^2$. Since each velocity component is uniformly distributed over its domain, the fluctuations are large and of the order of v_{\max}^2 . The same holds for the rescaled angular velocity, $\sqrt{\alpha} \omega L$.

Remarkably, the time series of $v_{\parallel}(t)$ exhibits many segments with only small fluctuations where it remains essentially constant over many hundred collisions. At the same time, there is only little kinetic energy in the transverse and rotational degrees of freedom; in particular, the needle merely rotates. A non-rotating needle is in a metastable state where it can travel straight over long distances in spite of collisions. The needle is said to be in such a “persistent” state A as long as its longitudinal velocity exceeds some threshold, $|v_{\parallel}(t)| > \theta$. Therewith, the time series is coarsened and can be subjected to further analysis, see bottom panels in Fig. 6.10. In particular, the distribution of persistent times τ_p , i. e., how long the needle remains in state A , can be measured. We find that the persistent times are Poisson-distributed, giving evidence for the spontaneous character of the “decay” of this metastable state and for the random distribution of the turning-back events. The average persistence time yields the desired limit on the extended ballistic regime, a new time scale τ_{turn} . Once this time scale is known, the translational diffusion coefficient D_{cm} is easily estimated by matching the extended ballistic and the diffusive regimes at the cross-over, $\frac{1}{2}v^2\tau_{\text{turn}}^2 \approx 4D_{\text{cm}}\tau_{\text{turn}}$, yielding

$$D_{\text{cm}} \approx \frac{1}{8}v^2\tau_{\text{turn}}. \quad (6.29)$$

Consequently, the time scale at which the turning-back events take place diverges for $n^* \rightarrow \infty$ as the diffusion coefficient D_{cm} does, $\tau_{\text{turn}} \sim (n^*)^{\zeta}$.

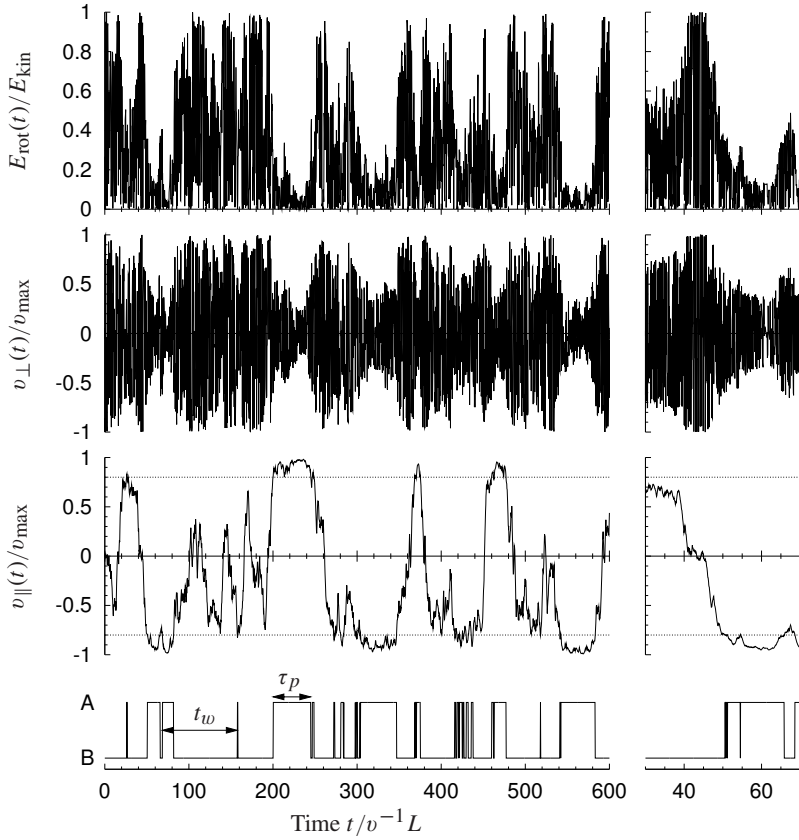


Figure 6.10 A realization of the time series of various variables at high density, $n^* = 120$: the kinetic energy of the rotational degree of freedom, $E_{\text{rot}}(t)$, and the transverse and longitudinal parts of the velocity, $v_{\perp}(t)$ and $v_{\parallel}(t)$. While the first two variables fluctuate fast, the longitudinal velocity fluctuates slowly and exhibits an affinity to its maximum values. The panels at the bottom display the coarse-grained, binary function $\Theta(|v_{\parallel}(t)| > \theta)$. Right panels: blow up of a turning-back event.

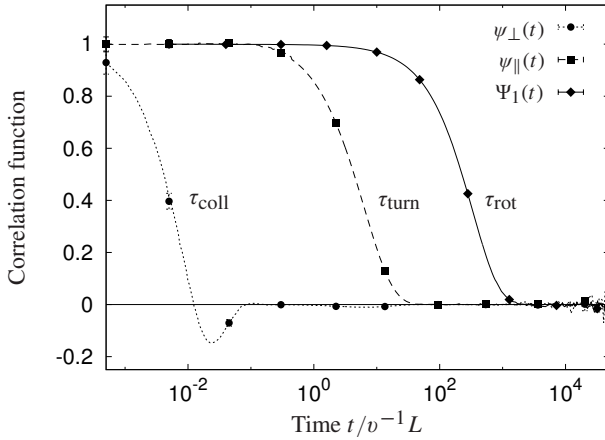


Figure 6.11 Correlation functions $\psi_{\perp}(t)$, $\psi_{\parallel}(t)$ and $\Psi_1(t)$ for dense obstacles, $n^* = 120$. Compare $\psi_{\perp}(t)$ and $\psi_{\parallel}(t)$ with the total velocity auto-correlation function $\psi_{\text{cm}}(t)$ in Fig. 6.8.

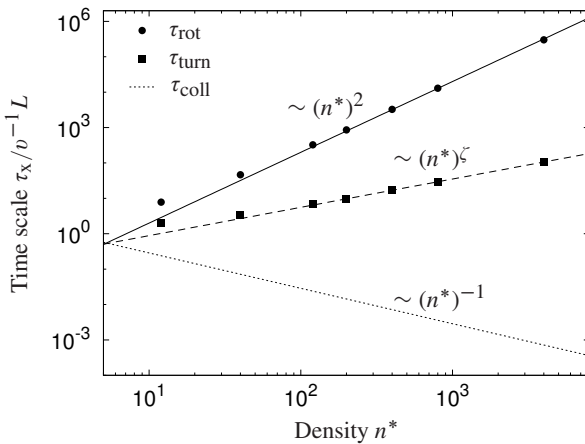


Figure 6.12 Three different time scales are relevant for the dynamics: the inverse collision rate, τ_{coll} , the rate of turning-back events, τ_{turn} , and the relaxation time of orientation, τ_{rot} .

Separation of time scales

The presented approach has the flaw to depend on the threshold θ and on the sampling rate of the time series; therefore, it is not fully conclusive. A more fruitful analysis is based on the auto-correlation functions of both velocity components separately,

$$\psi_{\parallel}(t) := \frac{2}{v^2} \langle v_{\parallel}(t) v_{\parallel}(0) \rangle \quad \text{and} \quad \psi_{\perp}(t) := \frac{2}{v^2} \langle v_{\perp}(t) v_{\perp}(0) \rangle. \quad (6.30)$$

At high obstacle densities, these functions reflect the two-step relaxation of the combined velocity correlation function, $\psi_{\text{cm}}(t)$. The connection follows from a decomposition of the latter; starting from $\mathbf{v} = v_{\parallel} \hat{\mathbf{e}}_{\varphi} + v_{\perp} \hat{\mathbf{e}}_{\perp}$, it follows

$$\langle \mathbf{v}(t) \cdot \mathbf{v}(0) \rangle = \left\langle [v_{\parallel}(t) v_{\parallel}(0) + v_{\perp}(t) v_{\perp}(0)] \cos(\Delta\varphi(t)) \right\rangle \quad (6.31)$$

The cosine term describes the relaxation of orientation, see Eq. (6.21), which we assume to be even slower than the decay of the persistent state—this is reasonable at high densities, see Fig. 6.11. Then, the average can be factorized, yielding

$$\psi_{\text{cm}}(t) \approx \frac{1}{2} [\psi_{\parallel}(t) + \psi_{\perp}(t)] \Psi_1(t). \quad (6.32)$$

The three correlation functions essentially show an exponential decay, defining three different time scales. These time scales diverge as the density increases (Fig. 6.12). The transverse velocity relaxes on the time scale of the individual collisions, $\tau_{\text{coll}} \sim (n^*)^{-1}$, see Eq. (6.27); the negative minimum in $\psi_{\perp}(t)$ after 2 or 3 collisions illustrates the rattling of the needle in its tube. The relaxation of the longitudinal velocity limits the extended ballistic regime; the characteristic time scale, τ_{turn} , is attributed to the waiting-time distribution of turning-back events and increases with the density, $\tau_{\text{turn}} \sim (n^*)^{\zeta}$. Eventually, the orientation of the needle relaxes on the time scale $\tau_{\text{rot}} \sim (n^*)^2$, given by the inverse of the rotational diffusion coefficient, Eq. (6.24).

Conclusion

We have studied a novel model for transport of rods in a disordered environment exhibiting interesting dynamic phenomena. Though translation and rotation depend strongly on each other, collective effects lead to the emergence of two different macroscopic time scales decoupling translation and rotation on long time scales. The dynamics of rotation and in particular the suppression of

the diffusion coefficient as $D_{\text{rot}} \sim 1/n^2 L^5$ is well explained in terms of a tube model. The center-of-mass motion exhibits the interesting feature of enhanced diffusion in the presence of a dense obstacle environment, $D_{\text{cm}} \sim n^\zeta L^{1+2\zeta}$ where $\zeta \approx 0.8$, which is related to a macroscopic zig-zag motion; its origin, however, is still unresolved.

In Christ are hidden all the treasures of wisdom and knowledge.

(Colossians 2:3)

7 Synopsis

Nature as well as modern technology presents us a variety of heterogeneous materials ranging from sedimented rock over composites and gels to the cytoskeleton of eukaryotic cells. The anomalous transport properties of simple and macro-molecules within such materials are highly relevant for technical applications or for physiological functioning. The cytoskeleton, a fiber network of biopolymers, determines the mechanical properties of biological tissue, and it is of great interest to understand the dynamics of single fibers in such networks. Such fibers being stiff may be modeled in a first approach by rigid rods.

A generic model for transport in heterogeneous materials, namely the Lorentz model, is in the focus of this thesis. It describes the motion of a tracer particle between overlapping spherical obstacles. In the regime of high obstacle density, the tracer dynamics becomes subdiffusive, and the model is well suited to give a microscopic explanation of anomalous transport. Above a critical density, diffusion vanishes, and the tracers are trapped—this critical phenomenon, known as localization, is related to the percolation transition of the void space between the obstacles.

Using extensive Molecular Dynamics simulations, the localization transition and its critical properties were investigated. A coherent and quantitative explanation of the dynamics was given in terms of continuum percolation theory, and an excellent matching of the critical exponents was obtained. The measurements were subjected to a finite-size scaling analysis for the diffusion coefficient providing an accurate result for the critical density, which collapses with the percolation threshold. A spatially resolved analysis considered the van Hove function, i. e., the temporal and spatial probability distribution of the tracer particle, and its Fourier transform, the incoherent intermediate scattering function. Therewith, the coexistence of localized and diffusing particles below the critical density was demonstrated. Further, a hyperscaling relation that is peculiar to continuum percolation was verified; it relates the dynamic

exponent to the static exponents.

Furthermore, the thesis established the intimate connection between the Lorentz model at high densities and continuum percolation, originating in a series of conjectured, but so far unproven mappings. In the literature, the diffusivity of the Lorentz model was related to the conductivity in continuum percolation models, being investigated further by mappings to random resistor networks, and next to regular lattices. These mappings are rather convincing from a theoretical point of view to analyze the universal properties of such models as soon as the temporal and spatial scales, as well as the relevant correlation times and lengths are large. However, it is of great interest to establish in detail the predictions for universal exponents and scaling functions for a specific model of paramount importance as the Lorentz model.

The quality of the obtained data for the mean-square displacements allowed for carrying out a scaling analysis that identifies the leading corrections to scaling. Including these corrections substantially improved the data collapse in the regime of anomalous transport. It was demonstrated that the corrections to scaling are relevant in the experimentally accessible window of time and length scales; there, the corrections pretend exponents of the anomalous transport varying with the obstacle density.

For diffusion on general percolation clusters, a prediction was made relating the universal dynamic correction-to-scaling exponent to the leading static correction exponent. The latter is easier accessible, e. g., by measurements of the distribution of cluster sizes, and known for the three-dimensional Lorentz model. This prediction is based on a generalization of the van Hove function, which was extended to the static structure of the medium. The generalized van Hove function further allowed for a cluster-resolved statistical description of the dynamics and illuminated the emergence of two different length scales in the dynamic properties close to the transition. Both length scales, the correlation length and the localization length, enter the dynamic scaling Ansatz for the usual van Hove function. This interesting feature is in contrast to other critical phenomena where a single length scale, the correlation length, governs the physics close to the transition. It was shown that the presence of two length scales manifests itself in the divergence of the non-Gaussian parameter, a quantity being discussed in the context of structural glasses.

In the second part of the thesis, a novel variant of the two-dimensional Lorentz model was investigated, which describes the dynamics of a rod in a disordered static environment of point obstacles. It may serve as a toy model for the dynamics of a semi-dilute solution of rigid rods and provide fundamental insight into the complex physics of such systems. In contrast to the conven-

tional Lorentz model, the tracer particle is enriched by a rotational degree of freedom and exhibits a striking asymmetric geometry. Next to the obstacle density, a second control parameter appears: the aspect ratio between length and diameter of the rod.

The limit of thin rods, i. e., needles, is of particular interest reflecting exactly the notion of a semi-dilute solution: the polymers are highly entangled, and excluded volume effects are absent. Reducing the model parameters to one again and completely suppressing the percolation scenario, the needle limit is also theoretically of great importance: it describes a system with trivial static properties, but highly non-trivial, “entangled” dynamics. Thus, completely new aspects of the dynamics in heterogeneous materials are revealed, pure entanglement effects can be studied without being spoiled by the critical slowing down due to the percolation transition of the medium.

The analysis started with a theoretical description within the Boltzmann approximation of uncorrelated collisions which accounts for the low density regime, where the translational and rotational diffusion coefficients both are linearly suppressed with increasing obstacle density. The more interesting high density regime, however, is so far merely accessible by Molecular Dynamics simulations. These simulations pose considerable algorithmic challenges since the collision detection is not straightforward anymore as in the case of spherical particles—it crucially depends on automatically proving the non-existence of zeros of transcendental equations. Applying methods from interval analysis, an efficient and robust algorithm for the collision detection was developed. This algorithm allowed for a deep exploration of the high density regime yielding diffusion coefficients and correlation functions over the full density range.

The tube model for highly entangled networks of rigid rods makes predictions on the suppression of the rotational diffusion coefficient due to the entanglement of long needles. Since this model assumes the surrounding rods to be frozen as well, the presented simulations provided also a thorough verification of these predictions.

The strong entanglement effects lead to another surprising and novel observation: the enhancement of center-of-mass diffusion with increasing density. Analyzing mean-square displacements of position and orientation and velocity auto-correlation functions as well as directly inspecting trajectories, this effect was attributed to the confinement of the needle in tubes and the emergence of an intermediate ballistic regime. Further, it was pointed out that a hierarchy of well-separated time scales exists leading to fast and slow relaxation channels for density fluctuations. In particular, translational and rotational dynamics

are well separated at high densities.

In conclusion, the first “experimental” data for the high density regime of the Lorentz model were obtained. Using the results from continuum percolation theory achieved a comprehensive and detailed understanding of the localization transition. Its description comprised a dynamic scaling Ansatz with two divergent length scales and the inclusion of leading corrections to scaling. Further, a novel variant of the Lorentz model was introduced, using a needle as tracer particle and reducing the obstacles to points; this model gives insight into the dynamics of entangled networks of stiff polymers. Many aspects of the dynamics were explained qualitatively by identifying a hierarchy of different time scales. A surprising finding was the enhancement of diffusion with increasing obstacle density. The model belongs to a class of purely dynamic models exhibiting novel collective phenomena; their future investigation will yield fundamental insight into collective dynamics.

Appendix

A Matrix Elements of the Collision Operator

The matrix elements of the collision operator $T_{\pm}(j)$ determine the microscopic frequencies ν_{cm} and ν_{rot} that describe the relaxation of the current correlators (Chapter 5). The aim of this appendix is to evaluate these matrix elements.

The phase space element for microcanonic states in an infinitesimal energy shell around E is given by

$$d\Gamma = \frac{1}{2\pi V} w(v, \omega) d^2r d\varphi d^2v d\omega, \quad (\text{A.1})$$

with the short cut,¹

$$w(v, \omega) := \frac{m}{4\pi} \sqrt{\frac{I}{2E}} \delta\left(\frac{1}{2}mv^2 + \frac{1}{2}I\omega^2 - E\right). \quad (\text{A.2})$$

Assuming obstacle 1 in the coordinate origin, we have $\Delta\mathbf{r}_1 = \mathbf{r}$, and we start with the evaluation of ν_R :

$$\nu_R = -\omega_R^{-2} N \langle \omega T_-(1) \omega \rangle \quad (\text{A.3})$$

$$= -\frac{N}{\omega_R^{-2}} \left\langle \delta(\mathbf{r} \times \hat{\mathbf{e}}_\varphi) \Theta\left(\frac{L}{2} - r\right) \Theta(\mathbf{v} \times \hat{\mathbf{e}}_\varphi - \omega a) 2m\omega a \frac{(\mathbf{v} \times \hat{\mathbf{e}}_\varphi - \omega a)^2}{I + ma^2} \right\rangle, \quad (\text{A.4})$$

¹The normalization factor is obtained from the following integral,

$$\int d^2v d\omega \delta\left(\frac{1}{2}mv^2 + \frac{1}{2}I\omega^2 - E\right) = 4\pi \int_0^\infty v dv d\omega \delta\left(\frac{1}{2}mv^2 + \frac{1}{2}I\omega^2 - E\right)$$

substituting $\varepsilon_T = \frac{1}{2}mv^2$ and $\varepsilon_R = \frac{1}{2}I\omega^2$,

$$= \frac{4\pi}{m} \int_0^\infty d\varepsilon_T \int_0^\infty \frac{d\varepsilon_R}{\sqrt{2I\varepsilon_R}} \delta(\varepsilon_T + \varepsilon_R - E) = \frac{4\pi}{m} \int_0^E \frac{d\varepsilon_R}{\sqrt{2I\varepsilon_R}} = \frac{4\pi}{m} \sqrt{\frac{2E}{I}}.$$

with the abbreviations $a = -\mathbf{r} \cdot \hat{\mathbf{e}}_\varphi$ and $r = |\mathbf{r}|$. The δ -function enforces $a = \pm r$, and we substitute r by a ,

$$= -\frac{N}{2\pi V \omega_R^2} \int_{-L/2}^{L/2} da \int_{-\pi}^{\pi} d\varphi d^2v d\omega w(v, \omega) \times \Theta(\mathbf{v} \times \hat{\mathbf{e}}_\varphi - \omega a) 2m\omega a \frac{(\mathbf{v} \times \hat{\mathbf{e}}_\varphi - \omega a)^2}{I + ma^2}. \quad (\text{A.5})$$

In the second line, the velocity enters only via $\mathbf{v} \times \hat{\mathbf{e}}_\varphi$; introducing polar coordinates (v, ψ) for \mathbf{v} , we can exploit the periodicity in the angles,

$$\int d\varphi d^2v f(\mathbf{v} \times \hat{\mathbf{e}}_\varphi) = \int_{-\pi}^{\pi} d\varphi \int_0^{\infty} v dv \int_{-\pi}^{\pi} d\psi f(v \sin(\varphi - \psi)) \quad (\text{A.6})$$

$$= 4\pi \int_0^{\infty} v dv \int_{-\pi/2}^{\pi/2} d\varphi f(v \sin(\varphi)). \quad (\text{A.7})$$

Substituting φ by $u = \sin(\varphi)$ and ω by $x = -\omega a/v$, we obtain

$$v_R = \frac{4mN}{V \omega_R^2} \int_{-L/2}^{L/2} da \int_0^{\infty} v^5 dv \int_{-1}^1 \frac{du}{\sqrt{1-u^2}} \int_{-\infty}^{\infty} dx \frac{1}{|a|} w\left(v, \frac{xv}{a}\right) \times \Theta(u+x) x \frac{(u+x)^2}{I + ma^2}. \quad (\text{A.8})$$

The u -integral is treated next,

$$F_R(x) := \int_{-1}^1 \frac{du}{\sqrt{1-u^2}} \Theta(u+x) (u+x)^2 \quad (\text{A.9})$$

$$= \begin{cases} \pi(x^2 + \frac{1}{2}) & \text{for } x > 1, \\ \frac{3}{2}x\sqrt{1-x^2} + (x^2 + \frac{1}{2})\left(\arcsin(x) + \frac{\pi}{2}\right) & \text{for } |x| \leq 1, \\ 0 & \text{for } x < -1. \end{cases} \quad (\text{A.10})$$

The v -dependence has factorized, and its integral is easily carried out,

$$\int_0^{\infty} v^5 dv w\left(v, \frac{xv}{a}\right) = \frac{m}{4\pi} \sqrt{\frac{I}{2E}} \times \frac{4E^2}{(m + Ix^2a^{-2})^3}. \quad (\text{A.11})$$

Collecting results, recalling that $I = am(L/2)^2$ and $n^* = NL^2/V$, and substituting $y = 2a/L$, Eq. (A.8) reduces to

$$\nu_R = \frac{\alpha^2 n^*}{4\pi \omega_R^2} \left(\frac{2E}{I}\right)^{\frac{3}{2}} \int_{-1}^1 \frac{dy}{|y|} \int_{-\infty}^{\infty} dx \frac{1}{(1 + \alpha x^2 y^{-2})^3} \frac{x F_R(x)}{\alpha + y^2}. \quad (\text{A.12})$$

Observing that rotation constitutes one out of three degrees of freedom, it holds $\frac{1}{2}I\omega_R^2 = \frac{1}{3}E$, and the prefactor simplifies,

$$= \frac{3\sqrt{3}}{2\pi} \alpha^2 n^* \omega_R \int_0^1 dy \int_{-\infty}^{\infty} dx \frac{y^5}{(y^2 + \alpha x^2)^3} \frac{x F_R(x)}{\alpha + y^2}. \quad (\text{A.13})$$

The remaining two integrals can be solved using MATHEMATICA,

$$\int_{-\infty}^{\infty} dx \frac{x F_R(x)}{(y^2 + \alpha x^2)^3} = \frac{\pi \sqrt{\alpha + y^2}}{4\alpha^2 y^3}, \quad (\text{A.14})$$

$$\int_0^1 dy \frac{y^2}{\sqrt{\alpha + y^2}} = \frac{1}{2} \sqrt{1 + \alpha} - \frac{\alpha}{2} \text{Arsinh}\left(\alpha^{-1/2}\right), \quad (\text{A.15})$$

yielding the final result for the microscopic frequency for rotation,

$$\nu_R = \frac{3\sqrt{3}}{16} n^* \omega_R \left(\sqrt{1 + \alpha} - \alpha \text{Arsinh}\left(\alpha^{-1/2}\right) \right), \quad (\text{A.16})$$

$$\approx 0.23244 n^* \omega_R \quad \text{for } \alpha = \frac{1}{3}. \quad (\text{A.17})$$

The evaluation of the matrix element for ν_T is carried out in a similar fash-

ion,

$$v_T = -\frac{N}{2\omega_T^2} \langle \mathbf{v} \cdot T_-(1) \mathbf{v} \rangle \quad (\text{A.18})$$

$$= -\frac{N}{2\omega_T^2} \left\langle \delta(\mathbf{r} \times \hat{\mathbf{e}}_\varphi) \Theta\left(\frac{L}{2} - r\right) \right. \\ \left. \times \Theta(\mathbf{v} \times \hat{\mathbf{e}}_\varphi - \omega a) 2I \mathbf{v} \cdot \hat{\mathbf{e}}_\perp \frac{(\mathbf{v} \times \hat{\mathbf{e}}_\varphi - \omega a)^2}{I + ma^2} \right\rangle; \quad (\text{A.19})$$

noting that $\mathbf{v} \cdot \hat{\mathbf{e}}_\perp = -\mathbf{v} \times \hat{\mathbf{e}}_\varphi$ and again substituting r by $a = -\mathbf{r} \cdot \hat{\mathbf{e}}_\varphi$,

$$= \frac{NI}{2\pi V \omega_T^2} \int_{-L/2}^{L/2} da \int_{-\pi}^{\pi} d\varphi \int d^2v d\omega w(v, \omega) \\ \times \Theta(\mathbf{v} \times \hat{\mathbf{e}}_\varphi - \omega a) (\mathbf{v} \times \hat{\mathbf{e}}_\varphi) \frac{(\mathbf{v} \times \hat{\mathbf{e}}_\varphi - \omega a)^2}{I + ma^2}. \quad (\text{A.20})$$

Integrating over the orientation of \mathbf{v} and substituting $u = \sin(\varphi)$ and $x = -\omega a/v$, yields [cf. Eq. (A.8)]

$$= \frac{2NI}{V \omega_T^2} \int_{-L/2}^{L/2} \frac{da}{|a|} \int_0^\infty v^5 dv \int_{-1}^1 \frac{du}{\sqrt{1-u^2}} \int_{-\infty}^\infty dx w\left(v, \frac{xv}{a}\right) \\ \times \Theta(u+x) u \frac{(u+x)^2}{I + ma^2}. \quad (\text{A.21})$$

The u -integral introduces another function $F_T(x)$,

$$F_T(x) := \int_{-1}^1 \frac{du}{\sqrt{1-u^2}} \Theta(u+x) u (u+x)^2 \quad (\text{A.22})$$

$$= \begin{cases} \pi x & \text{for } x > 1, \\ \frac{1}{3}(x^2 + 2)\sqrt{1-x^2} + x \left(\arcsin(x) + \frac{\pi}{2}\right) & \text{for } |x| \leq 1, \\ 0 & \text{for } x < -1. \end{cases} \quad (\text{A.23})$$

Making use of Eq. (A.11) and substituting $y = 2a/L$, we arrive at

$$v_T = \frac{\alpha^2 n^* E^2}{2\pi \omega_T^2 m I} \sqrt{\frac{I}{2E}} \int_{-1}^1 \frac{dy}{|y|} \int_{-\infty}^{\infty} dx \frac{1}{(1 + \alpha x^2 y^{-2})^3} \frac{F_T(x)}{\alpha + y^2}, \quad (\text{A.24})$$

using $\frac{1}{2}m\omega_T^2 = \frac{1}{3}E$,

$$= \frac{3\sqrt{3}}{2\pi} \alpha^{3/2} \frac{n^* \omega_T}{L} \int_0^1 dy \int_{-\infty}^{\infty} dx \frac{y^5}{(y^2 + \alpha x^2)^3} \frac{F_T(x)}{\alpha + y^2}. \quad (\text{A.25})$$

Employing MATHEMATICA again for the x -integration,

$$\int_{-\infty}^{\infty} dx \frac{F_T(x)}{(y^2 + \alpha x^2)^3} = \frac{\pi \sqrt{\alpha + y^2}}{4\alpha y^5}, \quad (\text{A.26})$$

renders the remaining y -integral basic,

$$\int_0^1 dy \frac{1}{\sqrt{\alpha + y^2}} = \text{Arsinh}\left(\alpha^{-1/2}\right). \quad (\text{A.27})$$

This yields the final result,

$$v_T = \frac{3}{8} \sqrt{3\alpha} \text{Arsinh}\left(\alpha^{-1/2}\right) \frac{n^* \omega_T}{L}, \quad (\text{A.28})$$

$$\approx 0.49359 \frac{n^* \omega_T}{L} \quad \text{for } \alpha = \frac{1}{3}. \quad (\text{A.29})$$

We express the diffusion coefficients in units of $v = \sqrt{2} \omega_T$ and L , noting that $\omega_R = 2\omega_T/(\sqrt{\alpha} L)$; for a homogeneous mass distribution along the needle ($\alpha = \frac{1}{3}$), the prefactors evaluate to

$$D_{\text{cm}} = \frac{v^2}{2\nu_T} \approx 1.432 \frac{vL}{n^*}, \quad (\text{A.30})$$

and

$$D_{\text{rot}} = \frac{\omega_R^2}{\nu_R} \approx 10.54 \frac{vL^{-1}}{n^*}. \quad (\text{A.31})$$

B The Interval Newton Method

Interval analysis is a generalization of real analysis; intervals replace real numbers, interval arithmetic combines them, and interval analysis is used to study the properties of intervals and their arithmetic. In numeric computations, interval analysis is able to account for rounding errors due to a finite machine precision. Therefore, interval analysis may yield mathematically rigorous solutions for numerical problems such as global optimization or solving nonlinear equations. A detailed introduction into this field may be found in the book by *Hansen and Walster (2004)*.

B.1 A Short Introduction to Interval Analysis

An *interval number* X is defined as a closed interval of real numbers, $X := [a, b] = \{x \in \mathbb{R} \mid a \leq x \leq b\}$. A *degenerate* interval contains only a single number, $X = [a, a] = \{a\}$. The endpoints of an interval might be results of a computation; if they are not representable on a given computer, a is rounded downwards and b upwards, which guarantees that the obtained interval encloses the true result.

The four basic arithmetic operations $+$, $-$, \times , \div between two intervals are defined such that the outcome contains every possible result from combining elements of the involved intervals,

$$X \bullet Y := \{x \bullet y \mid x \in X \text{ and } y \in Y\}. \quad (\text{B.1})$$

This definition produces the following rules for generating the endpoints of two intervals $X = [a, b]$ and $Y = [c, d]$:

$$X + Y = [a + c, b + d] \quad (\text{B.2a})$$

$$X - Y = [a - d, b - c] \quad (\text{B.2b})$$

$$X \times Y = \begin{cases} [ac, bd] & \text{if } X \geq 0 \text{ and } Y \geq 0 \\ [bc, bd] & \text{if } X \geq 0 \text{ and } 0 \in Y \\ [bc, ad] & \text{if } X \geq 0 \text{ and } Y \leq 0 \\ \vdots & \end{cases} \quad (\text{B.2c})$$

$$\frac{1}{Y} = \left[\frac{1}{d}, \frac{1}{c} \right], \quad \frac{X}{Y} = X \times \frac{1}{Y}, \quad \text{if } 0 \notin Y \quad (\text{B.2d})$$

An interval X is *positive*, $X > 0$, if $x > 0$ for all $x \in X$, etc. For later convenience, we introduce a notation for the midpoint and the width of an interval $X = [a, b]$,

$$m(X) := (a + b)/2 \quad \text{and} \quad \text{wd}(X) := b - a. \quad (\text{B.3})$$

A consistent handling of division by zero, i. e., the case $0 \in Y$, becomes possible by extending the real axis to $-\infty$ and $+\infty$ and by extending the concept of intervals to finite unions of disjoint intervals, so-called *containment sets*. The latter subtlety leads to loops in the numerical algorithms and otherwise will tacitly be ignored in this introduction. We define $1/\{0\} := \{-\infty\} \cup \{+\infty\}$; therewith, splitting $Y = [c, 0] \cup \{0\} \cup [0, d]$ leads to

$$\frac{1}{Y} = \left[-\infty, \frac{1}{c} \right] \cup \left[\frac{1}{d}, \infty \right]. \quad (\text{B.4})$$

In general, division by an interval which contains zero splits the result into two disjoint intervals.

Armed with this arithmetic, the definition of interval extensions of real functions becomes straightforward. An *interval function* is an interval-valued function of one or more interval arguments. Let f be a real-valued function of real variables x_1, \dots, x_n , and let f^I be a corresponding interval function of interval variables X_1, \dots, X_n . The interval function f^I is said to be an *interval extension* of f if

$$f^I(\{x_1\}, \dots, \{x_n\}) = \{f(x_1, \dots, x_n)\} \quad (\text{B.5})$$

for any values of the x_i . An interval function f^I is said to be *inclusion isotonic* if $X_i \subset Y_i$ ($i = 1, \dots, n$) implies $f^I(X_1, \dots, X_n) \subset f^I(Y_1, \dots, Y_n)$, meaning simply that the resulting interval becomes sharper (or at least not wider) if the arguments become tighter intervals.

The above interval arithmetic is inclusion isotonic, and it follows that rational interval functions are inclusion isotonic as well—provided that we restrict a given rational function to a single form using only interval arithmetic operations. This restriction is necessary since the interval extension of a real function is not unique, a consequence of the so-called *dependence problem*. According to their definition, Eq. (B.1), the interval arithmetic operators yield sharp bounds on expressions such as $X - Y$ or $X \times Y$. If we, however, evaluate $X - X$ or $X \times X$, the resulting interval encloses all possible values of $x - x = 0$ or x^2 for $x \in X$, but does not provide a sharp bound. (Convince yourself by evaluating the expressions for $X = [-1, 2]$.) The interval arithmetic treats each occurrence of the interval X independently, i. e., evaluates $X - Y$ first and then lets $Y = X$. One way out of this problem is to define special rules for integer powers of intervals taking into account that even powers can't be negative. Another solution is to write interval expressions in such a way that the same interval occurs as sparsely as possible, for example $(X - 1)^2 - 1$ instead of $X^2 - 2X$.

The following theorem shows how easy it is to bound the range of a function; it is the most important theorem in interval analysis and referred to as the *fundamental theorem* of this field. One of its far reaching consequences is that it allows for the solution to the global optimization problem, which is, however, not covered in this appendix.

Fundamental theorem Let $f^I(X_1, \dots, X_n)$ be an infinite precision inclusion isotonic interval extension of a real function $f(x_1, \dots, x_n)$. Then $f^I(X_1, \dots, X_n)$ contains the range of values of $f(x_1, \dots, x_n)$ for all $x_i \in X_i$ ($i = 1, \dots, n$).

It states that the direct evaluation of a function using interval arithmetic produces rigorous bounds on the set of all function values over the argument intervals. The major benefit of the interval method is the calculation of bounds using only a single function evaluation. In particular, no sampling of the argument intervals is necessary! The computational effort is usually only twice the effort for evaluating a single real value of the given function. The obtained bounds are sharp if each variable occurs only once, and widened due to the dependence problem. Monotonically non-decreasing functions, e. g., the exponential function, provide another route to sharp bounds by defining $f^I(X) = [f(a), f(b)]$ for $X = [a, b]$.

B.2 The Interval Newton Method

The standard algorithm for numerically finding the roots of a high-degree polynomial or any arbitrary non-linear, real function f of a single variable is the Newton method. It converges fast, but the function has to satisfy certain requirements within a neighborhood of the root. In particular, one has to know the location of the root in advance, but if the initial estimate of the root is too far from the true root, convergence of the Newton method is not guaranteed; the method hopelessly fails. The author is not aware of any standard algorithm for root finding that dispenses with initial bracketing. It would be highly desirable to have a general purpose algorithm that would tell us for any supplied function whether it has real roots and how many, and would calculate them efficiently and precisely.

The interval Newton method is such an algorithm. It is *robust*, i. e., every zero of f in an initial interval X_0 is always found and correctly bounded. If there is no zero of f in X_0 , the algorithm automatically *proves* this fact in a finite number of iterations. As a by-product, it may even prove the existence of a simple zero. Second, the algorithm is *efficient*, i. e., if $0 \notin f'(X)$, then at least half of X is eliminated in each iteration, and the asymptotic ratio of convergence to a zero of f in X is quadratic (as is the ordinary Newton method). Finally, the algorithm works for a quite general class of functions: the only requirement on f is that it must be differentiable in X_0 with bounded derivative, and even this requirement can be relaxed by a variant of the algorithm.

The interval Newton method was derived by Moore (1966) in the following manner. The mean value theorem states that there is some point ζ between x and x^* such that

$$f(x) - f(x^*) = (x - x^*) f'(\zeta). \quad (\text{B.6})$$

If x^* is a zero of f , then $f(x^*) = 0$, and it follows

$$x^* = x - \frac{f(x)}{f'(\zeta)}. \quad (\text{B.7})$$

Let X be an interval containing both x and x^* , therewith $\zeta \in X$ as well. Then, the fundamental theorem implies that¹ $f'(\zeta) \in f'(X)$. Hence, $x^* \in N(x, X)$ where

$$N(x, X) := x - \frac{f^I(x)}{f'(X)}, \quad (\text{B.8})$$

¹To not overload the notation, the superscript I for interval extensions of derivatives will be suppressed, so $f'(X)$ is to be understood as an interval extension of the real function $f'(x)$.

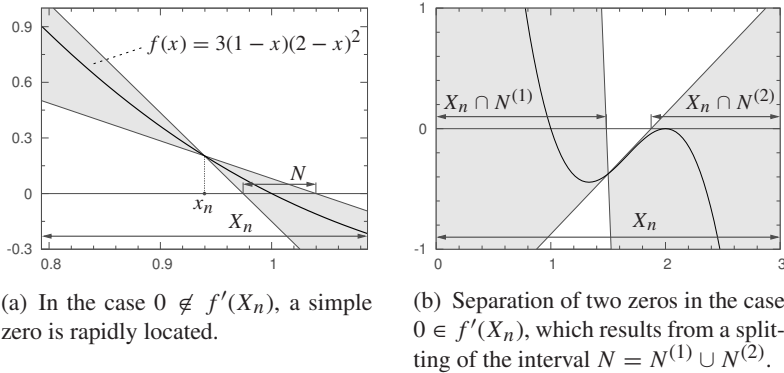


Figure B.1 Illustrations of the interval Newton method for $f(x) = 3(1-x)(2-x)^2$. The shaded areas correspond to all straight lines with slope in the range $f'(X_n)$ which pass through the point $[x_n, f(x_n)]$.

and we use $f^I(x)$ to denote the interval evaluation of $f(x)$ in order to bound rounding errors. Temporarily assume $0 \notin f'(X)$ so that $N(x, X)$ is a finite interval. In this case, the interval X contains only a single simple zero of f . Since any zero of f in X is also in $N(x, X)$, it is in the intersection $X \cap N(x, X)$, see Fig. B.1a.

Using this fact, the zero x^* is found from the following simple algorithm: Let X_0 be an interval containing x^* , then iterate

$$x_n = m(X_n), \quad X_{n+1} = X_n \cap N(x_n, X_n), \quad n \geq 0. \quad (\text{B.9})$$

If $0 \notin f'(X_m)$, then $0 \notin f'(X_n)$ for all $n > m$; this follows from inclusion isotonicity and the fact that $X_n \subset X_m$ for all $n > m$. Stop the iteration when $X_{n+1} = X_n$, i. e., no further reduction of the interval can be achieved due to rounding errors. In this case, $0 \in f^I(x_n)$, and x_n is a zero of f or at least near to one; the uncertainty is smaller than $\text{wd}(X_n)$.

The case $0 \in f'(X_n)$ is very different, but easily handled as long as $0 \notin f^I(x_n)$. The calculation of $N(x_n, X_n)$ involves a division by zero; according to Eq. (B.4), this yields two disjoint intervals $N = N^{(1)} \cup N^{(2)}$, both possibly containing a zero of f . In this situation, the algorithm branches and handles each interval separately (Fig. B.1b). Technically, the second interval is put on a stack and treated as initial interval for the search of another zero. It is the separation of zeros in the initial interval that makes the present algorithm so

powerful.

A singular case remains, and this one is really difficult to handle: if $0 \in f'(X_n)$ and $0 \in f^I(x_n)$. According to our rules, Eqs. (B.2) and (B.4), it would yield $N = [-\infty, \infty]$, which is a useless result. A possible solution is to change the point of expansion x_n , it can be chosen anywhere from $X_n = [a, b]$ and doesn't need to be the midpoint. One could try the interval boundaries a or b for example. Bad luck if $f^I(a)$ and $f^I(b)$ both contain zero as well. In that case, one could argue that the interval X_n is probably so small that rounding errors make the function indistinguishable from a function being constantly zero in X_n , e. g., in case of a multiple zero. Then, a criterion for stopping could be

$$\text{wd}(X_n) < \varepsilon_R x_n, \quad \text{or} \quad \text{wd}[f'(X_n)] / \text{wd}[f^I(x_n)] < R, \quad (\text{B.10})$$

with ε_R denoting the relative machine precision and R large, e. g., $R = 1000$. In practice, the second criterion never occurred, and the reader is referred to the book by Hansen and Walster (2004) for a further discussion.

This appendix will be closed by quoting some rigorous results concerning essential properties of the interval Newton method.

Theorem 1 (*Prove the existence of simple zeros*) Let X be a finite interval. If $N(x, X) \subset X$, there exists a simple zero of f in $N(x, X)$.

Theorem 2 (*Prove the uniqueness of a zero*) Assume $0 \notin f'(X)$. Then if X contains a zero of f , the zero is simple, i.e. unique.

Theorem 3 (*Prove the absence of a zero in a finite number of iterations*) Assume $|f(x)| \geq \delta > 0$ for all $x \in X_0$ and $|f'(X_0)| \leq M$ for some $M > 0$. Then X_0 is entirely eliminated in m steps of the algorithm, i. e., $X_m = \emptyset$, where $m \leq M \text{wd}(X_0) / 2\delta$.

Theorem 4 (*Convergence is fast even for wide intervals*) If $0 \notin f^I(x_n)$ and $0 \notin f'(X_n)$, then $\text{wd}(X_{n+1}) \leq \frac{1}{2} \text{wd}(X_n)$.

Theorem 5 (*Convergence is quadratic asymptotically*) If $0 \notin f'(X_n)$, then there exists a constant C such that $\text{wd}(X_{n+1}) = C \text{wd}(X_n)^2$.

Bibliography

The references are listed alphabetically; a dash indicates a repeated author list.

Alberts, B., A. Johnson, J. Lewis, M. Raff, K. Roberts, and P. Walter: *Molecular Biology of the Cell* (Garland Science, New York, 2002), 4th ed.

Alder, B. J. and W. E. Alley: *Long-time correlation effects on displacement distributions*, J. Stat. Phys. **19**, 341 (1978).

— *Decay of correlations in the Lorentz gas*, Physica A **121**, 523 (1983).

Alder, B. J. and T. E. Wainwright: *Studies in molecular dynamics. I. General method*, J. Chem. Phys. **31**, 459 (1959).

— *Velocity autocorrelations for hard spheres*, Phys. Rev. Lett. **18**, 988 (1967).

— *Decay of the velocity autocorrelation function*, Phys. Rev. A **1**, 18 (1970).

Amblard, F., A. C. Maggs, B. Yurke, A. N. Pargellis, and S. Leibler: *Subdiffusion and anomalous local viscoelasticity in actin networks*, Phys. Rev. Lett. **77**, 4470 (1996).

Aon, M. A., B. O'Rourke, and S. Cortassa: *The fractal architecture of cytoplasmic organization: Scaling, kinetics and emergence in metabolic networks*, Mol. Cell. Biochem. **256/257**, 169 (2004).

Arrio-Dupont, M., G. Foucault, M. Vacher, P. F. Devaux, and S. Cribier: *Translational diffusion of globular proteins in the cytoplasm of cultured muscle cells*, Biophys. J. **78**, 901 (2000).

ben Avraham, D. and S. Havlin: *Diffusion and Reactions in Fractals and Disordered Systems* (Cambridge University Press, Cambridge, 2000).

Bausch, A. R. and K. Kroy: *A bottom-up approach to cell mechanics*, Nat. Phys. **2**, 231 (2006).

- Bedaux, D. and P. Mazur: *Long time tails for the diffusion of tagged particles through a fluid*, Phys. Lett. A **43**, 401 (1973).
- Berthier, L., G. Biroli, J.-P. Bouchaud, L. Cipelletti, D. E. Masri, D. L'Hôte, F. Ladieu, and M. Pierno: *Direct experimental evidence of a growing length scale accompanying the glass transition*, Science **310**, 1797 (2005).
- Bertin, E., J.-P. Bouchaud, and F. Lequeux: *Subdiffusion and dynamical heterogeneities in a lattice glass model*, Phys. Rev. Lett. **95**, 15702 (2005).
- Binder, P.-M. and D. Frenkel: *Direct measurement of correlation functions in a lattice Lorentz gas*, Phys. Rev. A **42**, 2463 (1990).
- Bitsanis, I., H. T. Davis, and M. Tirrell: *Brownian dynamics of nondilute solutions of rodlike polymers. 1. Low concentrations*, Macromolecules **21**, 2824 (1988).
- *Brownian dynamics of nondilute solutions of rodlike polymers. 2. high concentrations*, Macromolecules **23**, 1157 (1990).
- Boon, J. P. and S. Yip: *Molecular Hydrodynamics* (Dover Publications, Inc., New York, 1991), reprint.
- Bruin, C.: *Logarithmic terms in the diffusion coefficient for the Lorentz gas*, Phys. Rev. Lett. **29**, 1670 (1972).
- *A computer experiment on diffusion in the Lorentz gas*, Physica **72**, 261 (1974).
- Campbell, A. I., V. J. Anderson, J. S. van Duijneveldt, and P. Bartlett: *Dynamical arrest in attractive colloids: The effect of long-range repulsion*, Phys. Rev. Lett. **94**, 208301 (2005).
- Caspi, A., R. Granek, and M. Elbaum: *Diffusion and directed motion in cellular transport*, Phys. Rev. E **66**, 011916 (2002).
- Coniglio, A.: *Thermal phase transition of the dilute s -state Potts and n -vector models at the percolation threshold*, Phys. Rev. Lett. **46**, 250 (1981).
- Derrida, B., J. G. Zabolitzky, J. Vannimenus, and D. Stauffer: *A transfer matrix program to calculate the conductivity of random resistor networks*, J. Stat. Phys. **36**, 31 (1984).
- Doi, M. and S. F. Edwards: *Dynamics of rod-like macromolecules in concentrated solution. Part 1*, J. Chem. Soc., Faraday Trans. 2 **74**, 560 (1978).
- *The Theory of Polymer Dynamics* (Oxford University Press, New York, 1986).

- Doi, M., I. Yamamoto, and F. Kano: *Monte carlo simulation of the dynamics of thin rodlike polymers in concentrated solution*, J. Phys. Soc. Jpn. **53**, 3000 (1984).
- Dorfman, J. R. and E. G. Cohen: *Velocity correlation functions in two and three dimensions*, Phys. Rev. Lett. **25**, 1257 (1970).
- Dorfman, J. R. and E. G. D. Cohen: *On the density expansion of the pair distribution function for a dense gas not in equilibrium*, Phys. Lett. **16**, 124 (1965).
- Dorfman, J. R. and E. G. D. Cohen: *Velocity-correlation functions in two and three dimensions: Low density*, Phys. Rev. A **6**, 776 (1972).
- *Velocity-correlation functions in two and three dimensions. II. Higher density*, Phys. Rev. A **12**, 292 (1975).
- Elam, W. T., A. R. Kerstein, and J. J. Rehr: *Critical properties of the void percolation problem for spheres*, Phys. Rev. Lett. **52**, 1516 (1984).
- Ernst, M. H., J. R. Dorfman, W. R. Hoegy, and J. M. J. van Leeuwen: *Hard-sphere dynamics and binary-collision operators*, Physica **45**, 127 (1969).
- Ernst, M. H., E. H. Hauge, and J. M. J. van Leeuwen: *Asymptotic time behavior of correlation functions*, Phys. Rev. Lett. **25**, 1254 (1970).
- *Asymptotic time behavior of correlation functions and mode-mode coupling theory*, Phys. Lett. A **34**, 419 (1971).
- Ernst, M. H., J. Machta, J. R. Dorfman, and H. van Beijeren: *Long time tails in stationary random media. I. Theory*, J. Stat. Phys. **34**, 477 (1984).
- Ernst, M. H. and A. Weijland: *Long time behaviour of the velocity auto-correlation function in a Lorentz gas*, Phys. Lett. A **34**, 39 (1971).
- Ferrell, R. A., N. Menyhárd, H. Schmidt, F. Schwabl, and P. Szépfalussy: *Dispersion in second sound and anomalous heat conduction at the lambda point of liquid helium*, Phys. Rev. Lett. **18**, 891 (1967).
- *Fluctuations and lambda phase transition in liquid helium*, Ann. Phys. (N. Y.) **47**, 565 (1968).
- Fixman, M.: *Dynamics of semidilute polymer rods: An alternative to cages*, Phys. Rev. Lett. **55**, 2429 (1985).
- Frenkel, D.: *Velocity auto-correlation functions in a 2d lattice Lorentz gas: Comparison of theory and computer simulation*, Phys. Lett. A **121**, 385 (1987).

- Frenkel, D. and J. F. Maguire: *Molecular Dynamics study of infinitely thin hard rods: Scaling behavior of transport properties*, Phys. Rev. Lett. **47**, 1025 (1981).
- *Molecular Dynamics study of the dynamical properties of an assembly of infinitely thin hard rods*, Mol. Phys. **49**, 503 (1983).
- Frenkel, D. and B. J. Smit: *Understanding Molecular Simulation* (Academic Press, London, 2001), 2nd ed.
- Frenkel, D., F. van Luijn, and P.-M. Binder: *Evidence for universal asymptotic decay of velocity fluctuations in lorentz gases*, Europhys. Lett. **20**, 7 (1992).
- Gardel, M. L., M. T. Valentine, J. C. Crocker, A. R. Bausch, and D. A. Weitz: *Microrheology of entangled F-actin solutions*, Phys. Rev. Lett. **91**, 158302 (2003).
- de Gennes, P. G.: *La percolation: un concept unificateur*, La Recherche **7**, 919 (1976).
- de Gennes, P.-G.: *Scaling Concepts in Polymer Physics* (Cornell University Press, Ithaca, NY, 1979).
- Gingold, D. B. and C. J. Lobb: *Percolative conduction in three dimensions*, Phys. Rev. B **42**, 8220 (1990).
- Gittes, F., B. Mickey, J. Nettleton, and J. Howard: *Flexural rigidity of microtubules and actin filaments measured from thermal fluctuations in shape*, J. Cell Biol. **120**, 923 (1993).
- Golding, I. and E. C. Cox: *Physical nature of bacterial cytoplasm*, Phys. Rev. Lett. **96**, 098102 (2006).
- Götze, W., E. Leutheusser, and S. Yip: *Correlation functions of the hard-sphere Lorentz model*, Phys. Rev. A **24**, 1008 (1981a).
- *Dynamical theory of diffusion and localization in a random, static field*, Phys. Rev. A **23**, 2634 (1981b).
- *Diffusion and localization in the two-dimensional Lorentz model*, Phys. Rev. A **25**, 533 (1982).
- Haines, L. K., J. R. Dorfman, and M. H. Ernst: *Divergent transport coefficients and the binary-collision expansion*, Phys. Rev. **144**, 207 (1966).
- Halperin, B. I., S. Feng, and P. N. Sen: *Differences between lattice and continuum percolation transport exponents*, Phys. Rev. Lett. **54**, 2391 (1985).
- Halperin, B. I. and P. C. Hohenberg: *Generalization of scaling laws to dynamical properties of a system near its critical point*, Phys. Rev. Lett. **19**, 700 (1967).

- Hansen, E. and G. W. Walster: *Global Optimization Using Interval Analysis* (Marcel Dekker, New York, 2004), 2nd ed.
- Harris, A. B., S. Kim, and T. C. Lubensky: ε expansion for the conductivity of a random resistor network, *Phys. Rev. Lett.* **53**, 743 (1984).
- Havlin, S. and D. Ben-Avraham: *Diffusion in disordered media*, *Adv. Phys.* **51**, 187 (2002).
- Hellriegel, C., J. Kirstein, and C. Bräuchle: *Tracking of single molecules as a powerful method to characterize diffusivity of organic species in mesoporous materials*, *New J. Phys.* **7**, 23 (2005).
- Hinner, B., M. Tempel, E. Sackmann, K. Kroy, and E. Frey: *Entanglement, elasticity, and viscous relaxation of actin solutions*, *Phys. Rev. Lett.* **81**, 2614 (1998).
- Höfling, F., T. Franosch, and E. Frey: *Localization transition of the three-dimensional Lorentz model and continuum percolation*, *Phys. Rev. Lett.* **96**, 165901 (2006).
- Hohenberg, P. C. and B. I. Halperin: *Theory of dynamic critical phenomena*, *Rev. Mod. Phys.* **49**, 435 (1977).
- Huthmann, M., T. Aspelmeier, and A. Zippelius: *Granular cooling of hard needles*, *Phys. Rev. E* **60**, 654 (1999).
- Isambert, H. and A. Maggs: *Dynamics and rheology of actin solutions*, *Macromolecules* **29**, 1036 (1996).
- Käs, J., H. Strey, and E. Sackmann: *Direct imaging of reptation for semiflexible actin filaments*, *Nature* **368**, 226 (1994).
- Käs, J., H. Strey, J. Tang, D. Finger, R. Ezzell, E. Sackmann, and P. Janmey: *F-actin, a model polymer for semiflexible chains in dilute, semidilute, and liquid crystalline solutions*, *Biophys. J.* **70**, 609 (1996).
- Kawasaki, K.: *Application of extended mode-coupling theory to long-time behavior of correlation functions*, *Prog. Theor. Phys.* **45**, 1691 (1971).
- Kerstein, A. R.: *Equivalence of the void percolation problem for overlapping spheres and a network problem*, *J. Phys. A* **16**, 3071 (1983).
- Kertész, J.: *Percolation of holes between overlapping spheres: Monte carlo calculation of the critical volume fraction*, *J. Phys. (Paris)* **42**, L 393 (1981).
- Kertész, J. and J. Metzger: *Properties of the density relaxation function in classical diffusion models with percolation transition*, *J. Phys. A* **16**, L735 (1983).

- Knoblich, B. and T. Gerber: *The arrangement of fractal clusters dependent on the pH value in silica gels from sodium silicate solutions*, J. Non-Cryst. Solids **296**, 81 (2001).
- Kroy, K.: *Elasticity, dynamics and relaxation in biopolymer networks*, Curr. Opin. Colloid Interface Sci. **11**, 56 (2006).
- Le Goff, L., O. Hallatschek, E. Frey, and F. m. c. Amblard: *Tracer studies on F-actin fluctuations*, Phys. Rev. Lett. **89**, 258101 (2002).
- van Leeuwen, J. M. J. and A. Weijland: *Non-analytic density behaviour of the diffusion coefficient of a Lorentzgas I*, Physica (Amsterdam) **36**, 457 (1967).
- Levi, V., Q. Ruan, and E. Gratton: *3-d particle tracking in a two-photon microscope: Application to the study of Molecular Dynamics in cells*, Biophys. J. **88**, 2919 (2005).
- Lorentz, H. A.: *Le mouvement des electrons dans les metaux*, Arch. Néerl. **10**, 336 (1905).
- Lorenz, C. D. and R. M. Ziff: *Precise determination of the bond percolation thresholds and finite-size scaling corrections for the sc, fcc, and bcc lattices*, Phys. Rev. E **57**, 230 (1998).
- Lowe, C. P. and A. J. Masters: *The long-time behaviour of the velocity autocorrelation function in a Lorentz gas*, Physica A **195**, 149 (1993).
- Lübeck, S.: *Universal scaling behavior of non-equilibrium phase transitions*, Int. J. Mod. Phys. B **18**, 3977 (2005).
- Lubensky, T. C. and A.-M. S. Tremblay: *ε expansion for transport exponents of continuum percolating systems*, Phys. Rev. B **34**, 3408 (1986).
- Luby-Phelps, K., P. E. Castle, D. L. Taylor, and F. Lanni: *Hindered diffusion of inert tracer particles in the cytoplasm of mouse 3T3 cells*, Proc. Natl. Acad. Sci. USA **84**, 4910 (1987).
- Luby-Phelps, K., D. Taylor, and F. Lanni: *Probing the structure of cytoplasm*, J. Cell Biol. **102**, 2015 (1986).
- Machta, J., R. A. Guyer, and S. M. Moore: *Conductivity in percolation networks with broad distributions of resistances*, Phys. Rev. B **33**, 4818 (1986).
- Machta, J. and S. M. Moore: *Diffusion and long-time tails in the overlapping Lorentz gas*, Phys. Rev. A **32**, 3164 (1985).

- Magda, J. J., H. T. Davis, and M. Tirrell: *The transport properties of rod-like particles via molecular dynamics. I. Bulk fluid*, J. Chem. Phys. **85**, 6674 (1986).
- Manley, S., H. M. Wyss, K. Miyazaki, J. C. Conrad, V. Trappe, L. J. Kaufman, D. R. Reichman, and D. A. Weitz: *Glasslike arrest in spinodal decomposition as a route to colloidal gelation*, Phys. Rev. Lett. **95**, 238302 (2005).
- van der Marck, S. C.: *Network approach to void percolation in a pack of unequal spheres*, Phys. Rev. Lett. **77**, 1785 (1996).
- Masters, A. and T. Keyes: *Diffusion, percolation, and trapping in the Lorentz gas via variational kinetic theory*, Phys. Rev. A **26**, 2129 (1982).
- Medalia, O., I. Weber, A. S. Frangakis, D. Nicastro, G. Gerisch, and W. Baumeister: *Macromolecular architecture in eukaryotic cells visualized by cryoelectron tomography*, Science **298**, 1209 (2002).
- Metzler, R. and J. Klafter: *The random walk's guide to anomalous diffusion: a fractional dynamics approach*, Phys. Rep. **339**, 1 (2000).
- Moore, R. E.: *Interval Analysis* (Prentice-Hall, Englewood Cliffs, New Jersey, 1966).
- Moreno, A. J. and W. Kob: *Dynamics of a rigid rod in a glassy medium*, Europhys. Lett. **67**, 820 (2004a).
- *Relaxation dynamics of a linear molecule in a random static medium: A scaling analysis*, J. Chem. Phys. **121**, 380 (2004b).
- Mori, H.: *A continued-fraction representation of the time-correlation functions*, Progr. Theor. Phys. **34**, 399 (1965a).
- *Transport, collective motion, and brownian motion*, Progr. Theor. Phys. **33**, 423 (1965b).
- Morse, D. C.: *Tube diameter in tightly entangled solutions of semiflexible polymers*, Phys. Rev. E **63**, 031502 (2001).
- Nakayama, T., K. Yakubo, and R. L. Orbach: *Dynamical properties of fractal networks: Scaling, numerical simulations, and physical realizations*, Rev. Mod. Phys. **66**, 381 (1994).
- Odijk, T.: *The statistics and dynamics of confined or entangled stiff polymers*, Macromolecules **16**, 1340 (1983).
- Okabe, H. and M. J. Blunt: *Prediction of permeability for porous media reconstructed using multiple-point statistics*, Phys. Rev. E **70**, 066135 (2004).

- Ott, A., M. Magnasco, A. Simon, and A. Libchaber: *Measurement of the persistence length of polymerized actin using fluorescence microscopy*, Phys. Rev. E **48**, R1642 (1993).
- Otto, M., T. Aspelmeier, and A. Zippelius: *Microscopic dynamics of thin hard rods*, J. Chem. Phys. **124**, 154907 (2006).
- Palmer, A., T. G. Mason, J. Xu, S. C. Kuo, and D. Wirtz: *Diffusing wave spectroscopy microrheology of actin filament networks*, Biophys. J. **76**, 1063 (1999).
- de la Pena, L. H., R. van Zon, J. Schofield, and S. B. Opps: *Discontinuous molecular dynamics for semi-flexible and rigid bodies*, cond-mat/0607527 (2006).
- Rintoul, M. D.: *Precise determination of the void percolation threshold for two distributions of overlapping spheres*, Phys. Rev. E **62**, 68 (2000).
- Ruzicka, B., L. Zulian, and G. Ruocco: *Routes to gelation in a clay suspension*, Phys. Rev. Lett. **93**, 258301 (2004).
- Sahimi, M.: *Heterogeneous Materials*, vol. 22 of *Interdisciplinary Applied Mathematics* (Springer, New York, 2003).
- Saxton, M. J. and K. Jacobson: *Single-particle tracking: Applications to membrane dynamics*, Annu. Rev. Biophys. Biomol. Struct. **26**, 373 (1997).
- de Schepper, I. M. and M. H. Ernst: *Long time expansion of two-dimensional correlation functions*, Physica A **87**, 35 (1977).
- Schilling, R. and G. Szamel: *Glass transition in systems without static correlations: a microscopic theory*, J. Phys.: Condens. Matter **15**, S967 (2003a).
- *Microscopic theory for the glass transition in a system without static correlations*, Europhys. Lett. **61**, 207 (2003b).
- Seksek, O., J. Biwersi, and A. Verkman: *Translational diffusion of macromolecule-sized solutes in cytoplasm and nucleus*, J. Cell Biol. **138**, 131 (1997).
- Semenov, A. N.: *Dynamics of concentrated solutions of rigid-chain polymers. Part 1.—Brownian motion of persistent macromolecules in isotropic solution*, J. Chem. Soc., Faraday Trans. 2 **82** (1986).
- Sengers, J. V.: *Density expansion of the viscosity of a moderately dense gas*, Phys. Rev. Lett. **15**, 515 (1965).
- Skal, A. S. and B. I. Shklovskii: *Topology of the infinite cluster of the percolation theory and its application to the theory of the hopping conduction*, Sov. Phys. Semi-cond. **8**, 1029 (1975).

- Stauffer, D. and A. Aharony: *Introduction to Percolation Theory* (Taylor & Francis, London, 1994), 2nd ed.
- Stenull, O. and H. Janssen: *Conductivity of continuum percolating systems*, Phys. Rev. E **64**, 56105 (2001).
- Straley, J. P.: *Non-universal threshold behaviour of random resistor networks with anomalous distributions of conductances*, J. Phys. C **15**, 2343 (1982).
- Svitkina, T. M., E. A. Bulanova, O. Y. Chaga, D. M. Vignjevic, S.-i. Kojima, J. M. Vasiliev, and G. G. Borisy: *Mechanism of filopodia initiation by reorganization of a dendritic network*, J. Cell Biol. **160**, 409 (2003).
- Tokuyama, M. and I. Oppenheim: *Statistical-mechanical theory of brownian motion – translational motion in an equilibrium fluid*, Physica A **94**, 501 (1978).
- Tolić-Nørrelykke, I. M., E.-L. Munteanu, G. Thon, L. Oddershede, and K. Berg-Sørensen: *Anomalous diffusion in living yeast cells*, Phys. Rev. Lett. **93**, 078102 (2004).
- Torquato, S.: *Random Heterogeneous Materials* (Springer, Heidelberg, 2002).
- Weijland, A. and J. M. J. van Leeuwen: *Non-analytic density behaviour of the diffusion coefficient of a Lorentz gas II*, Physica (Amsterdam) **38**, 35 (1968).
- Weiss, M., M. Elsner, F. Kartberg, and T. Nilsson: *Anomalous subdiffusion is a measure for cytoplasmic crowding in living cells*, Biophys. J. **87**, 3518 (2004).
- Wong, I. Y., M. L. Gardel, D. R. Reichman, E. R. Weeks, M. T. Valentine, A. R. Bausch, and D. A. Weitz: *Anomalous diffusion probes microstructure dynamics of entangled F-actin networks*, Phys. Rev. Lett. **92**, 178101 (2004).
- Zaccarelli, E., S. V. Buldyrev, E. L. Nave, A. J. Moreno, I. Saika-Voivod, F. Sciortino, and P. Tartaglia: *Model for reversible colloidal gelation*, Phys. Rev. Lett. **94**, 218301 (2005).
- Ziemann, F., J. Radler, and E. Sackmann: *Local measurements of viscoelastic moduli of entangled actin networks using an oscillating magnetic bead micro-rheometer*, Biophys. J. **66**, 2210 (1994).
- Zwanzig, R.: *Memory effects in irreversible thermodynamics*, Phys. Rev. **124**, 983 (1961).
- *Time-correlation functions and transport coefficients in statistical mechanics*, Annu. Rev. Phys. Chem. **16**, 67 (1965).

Acknowledgments

I'm very grateful to Prof. Dr. Erwin Frey for posing the interesting and challenging subject of this thesis and for introducing me to the world of soft matter and biological physics. His continuous interest in my work and clearly pointing out the significance of my results as well as his enthusiasm about possible implications has been motivating all the time.

Without the collaboration with Dr. Thomas Franosch, this work were not what it is. I thank him for uncountably many fruitful discussions and for always asking the right questions—challenging me to try harder and to get more interesting results.

I am happy that my wife Diana makes my life more colorful. I thank her for a lot of sympathy especially during the time of writing up the thesis and for her steady love and encouragement.

From the very beginning, my parents have supported my affinity to sciences and later in particular my physics studies. I'm especially grateful that they always took care that I would receive the best possible education, and I thank them for their love and manifold help.

My colleagues from SF 5 made the daily work more pleasant. In particular, I thank Alexander Skupin, Claus Heußinger, Klaus Kroy, Rüdiger Thul and Thomas Franosch not only for nice and sometimes also useful talks about physics and much other stuff, but also for many pleasant challenges in *scopone scientifico*.

Gratefully, I acknowledge financial support during the last three years from IBM Deutschland and the Hahn-Meitner-Institut Berlin. Computer resources have been provided generously by the Leibniz Rechenzentrum München.

Above all, I thank Jesus Christ. He is the one everything comes from that I am and have, be it my aptitudes and talents, inventiveness and creativity, family and friends, or difficulties and success. In trouble and joy, He has always been faithfully on my side, with mercy and grace.

